

**BIOMACROMOLECULES, MOLECULES AND FUNCTIONAL  
NANOPARTICLES FOR THERAPEUTIC AND DIAGNOSTIC  
APPLICATIONS**

A DISSERTATION SUBMITTED TO  
THE GRADUATE SCHOOL OF ENGINEERING AND SCIENCE  
OF BILKENT UNIVERSITY  
IN PARTIAL FULFILLMENT OF THE REQUIREMENTS  
FOR THE DEGREE OF  
DOCTOR OF PHILOSOPHY  
IN  
MATERIALS SCIENCE AND NANOTECHNOLOGY

By

Ayşe Özdemir

March 2016

BIOMACROMOLECULES, MOLECULES AND FUNCTIONAL  
NANOPARTICLES FOR THERAPEUTIC AND DIAGNOSTIC  
APPLICATIONS

By Ayşe Özdemir  
March 2016

We certify that we have read this thesis and that in our opinion it is fully adequate, in scope and in quality, as a thesis for the degree of Doctor of Philosophy.

---

Ayşe Begüm Tekinay (Advisor)

---

Turgay Tekinay (Co-advisor)

---

Mustafa Özgür Güler

---

Bahri Aydın

---

Aykutlu Dana

---

Hatice Kader Karlı Ođuz

Approved for the Graduate School of Engineering and Science:

---

Levent Onural  
Director of the Graduate School

**ABSTRACT**

**BIOMACROMOLECULES, MOLECULES AND FUNCTIONAL  
NANOPARTICLES FOR THERAPEUTIC AND DIAGNOSTIC  
APPLICATIONS**

Ayşe Özdemir

PhD in Materials Science and Nanotechnology

Advisor: Ayşe Begüm Tekinay

Co-Advisor: Turgay Tekinay

March, 2016

Cancer is one of the most important global health problem. In the last decade, researchers have focused on the development of novel sensitive diagnostic agents and potential therapeutic molecules to further contribute to the success of cancer treatment and increase survival rates of cancer patients. Magnetic resonance imaging (MRI) is a powerful diagnostic tool and used in clinics for cancer imaging. Superparamagnetic iron oxide nanoparticles (SPIONs) are used as a negative contrast agent to increase sensitivity of MRI. SPIONs can be coated with biocompatible natural or synthetic materials to maintain stability and improve their blood distribution profile. SPIONs can also be non-covalently functionalized with peptide amphiphile (PA) molecules through hydrophobic interactions to render them water soluble and biocompatible. In addition, several efforts have been made to improve specificity and sensitivity of SPIONs by attaching cancer targeting agents such as peptides. For cancer therapy, metal based drugs have attracted attention because of their biological and pharmaceutical properties over the past decades. The understanding of interactions between potential agents and biomolecules is important for designing novel anticancer

drugs against tumors to overcome the toxicity of currently used chemotherapeutic drugs and achieve more precision. Herein, I investigated the potential of proline-rich PA coated SPIONs as a negative contrast agent for cancer diagnosis by MRI. To achieve water solubility and cancer targeting, positively charged K and LPPR peptide sequences were presented on the PA micelles. PA functionalization provided a water-dispersible hybrid system. Biocompatibility and efficient uptake of the SPIONs were found to be improved with PA coating. This hybrid system provided enhancement in the MR imaging of tumor tissue in chemically induced breast cancer model. In addition, *in vivo* experiments and histological examinations revealed the biodistribution and bioelimination profile of the nanoparticles. These SPION/PA system can potentially be used as a contrast agent in cancer diagnosis by MRI. In addition, I analyzed the interactions between metal based molecules that can be used as cancer therapeutics and calf thymus DNA or human serum albumin (HSA) by spectroscopic and calorimetric methods which showed the binding modes, affinities and the effects on the structure of these biomacromolecules. Although similar structures demonstrated similar binding characteristics, each molecule has different association with DNA or HSA. The obtained results are promising for the development of metal or half metal based anticancer agents targeting DNA and carried by HSA.

**Keywords:** Magnetic Resonance Imaging, Superparamagnetic Iron Oxide Nanoparticles, Biomacromolecule, Metal ions.

**ÖZET**

**TERAPÖTİK VE DİAGNOSTİK UYGULAMALAR İÇİN**

**BİYOMAKROMOLEKÜLLER, MOLEKÜLLER VE FONKSİYONEL**

**NANOPARÇACIKLAR**

Ayşe Özdemir

Malzeme Bilimi ve Nanoteknoloji, Doktora

Tez Danışmanı: Ayşe Begüm Tekinay

Eş Danışman: Turgay Tekinay

Mart, 2016

Kanser dünya genelinde en önemli sağlık sorunlarından biridir. Geçtiğimiz yüzyıl da araştırmacılar kanser tedavisinin başarısını arttırmaya katkıda bulunacak ve kanser hastalarının yaşama oranını yükseltecek yeni, hassas teşhis ajanları ve potansiyel tedavi edici moleküllerin geliştirilmesi üzerinde yoğunlaşmıştır. Manyetik rezonans görüntüleme etkili bir teşhis aracıdır ve klinikte kanser görüntülemeye kullanılmaktadır. Süperparamanyetik demir oksit nanoparçacıklar (SPION) MRI hassasiyetini arttırmak için negatif zıtlık ajanı olarak kullanılmaktadır. Kararlı halin sürdürülebilmesi ve kan dağılım profillerinin iyileştirilebilmesi için SPION'lar biyouyumlu, doğal veya sentetik malzemelerle kaplanabilir. Yeni bir yaklaşım olarak, SPION'lar peptit amfifil (PA) moleküllerle hidrofobik etkileşimler yoluyla suda çözünebilir ve biyouyumlu hale getirmek için fonksiyonlaştırılabilir. Ayrıca SPION'lara kanseri hedefleyen antibadi ve peptit gibi ajanlar eklenerek özgünlük ve hassasiyeti arttırmak için pek çok çaba sarfedilmektedir. Geçtiğimiz yıllarda metal içerikli ilaçlar gösterdikleri biyolojik ve farmakolojik özelliklerden dolayı antikanser ajanı olarak dikkatleri çekmiştir. Kullanılmakta olan sisplatin gibi kemoterapi

ilaçlarının toksisitesini ortadan kaldırmak ve daha hassas tedavi sağlamak için biyomoleküllerle potansiyel ajanlar arasındaki etkileşimlerin anlaşılması, yeni antikanser ilaçlarının dizaynı için önemlidir. Bu tez çalışmasında, prolince zengin peptit amfifillerle kaplanmış SPIONların MRI ile tümör görüntüleme negatif zıtlık ajanı olarak kullanılabilirliği araştırılmıştır. Suda çözünürlüğü sağlamak ve kanseri hedeflemek için pozitif yüklü K ve LPPR amino asit sekansları peptit amfifiller üzerinde sunulmuştur. PA fonksiyonlaştırması suda çözünebilir hibrit bir sistem sağlamıştır. PA kaplamasının biyoyumluluğu ve hücreye alımı arttırdığı bulunmuştur. Bu hibrit sistem, kimyasal yolla indüklenmiş meme kanseri modelindeki tümörün MR ile görüntüleme zıtlığı arttırmaktadır. Ayrıca *in vivo* deneyler ve histolojik incelemeler nanoparçacıkların biyolojik dağılımlarını ve biyoatılım profillerini ortaya çıkarmıştır. Bu SPION/PA sistemi potansiyel olarak MRI ile kanser teşhisinde negatif zıtlık ajanı olarak kullanılabilir. Ayrıca, kanser tedavisinde kullanılacak metal bazlı moleküller ile sığır timus DNA'sı veya insan serum albumin (HSA) arasındaki etkileşimler, bağlanma modları, ilgiler ve ilgili moleküllerin biyomakromoleküllerin yapısı üzerindeki etkileri spektroskopik ve kalorimetrik metotlarla ortaya çıkarılmıştır. Benzer yapılar benzer bağlanma karakteri gösterse de her molekül DNA veya HSA ile farklı bir ilişkiye sahiptir. Bu sonuçlar DNA'yı hedefleyen ve HSA tarafından taşınan metal yada yarı metal içerikli antikanser ajanlarının geliştirilmesi için umut vaatmektedir.

**Anahtar kelimeler:** Manyetik Rezonans Görüntüleme, Süperparamanyetik Demir Oksit Nanoparçacıklar, Biyomakromolekül, Metal iyonları.

## **Acknowledgement**

I would like to express my gratitude to my advisors, Prof. Ayşe Begüm Tekinay and Prof. Turgay Tekinay for their guidance and support of my research, for their patience, motivation, knowledge and kindness. Their guidance helped me in not only all the time of my Ph.D. but also having a good personality as a scientist.

I would like to thank Prof. Mustafa Özgür Güler for giving me the opportunity to study with his group and for devoting his valuable time to review and comments on this thesis. My Ph.D studies could not be completed without Prof. Güler's contributions.

I would like to thank Prof. Dr. Bahri Aydın, who helped me to develop my ideas, knowledge and understanding as a thesis committee member. I want to thank to the members of my thesis jury, Prof. Aykutlu Dana and Prof. Kader Karlı Oğuz for their valuable comments.

I would like to thank UNAM (National Nanotechnology Research Center) for technical and equipment support. I would like to acknowledge the PhD fellowship from TÜBİTAK (The Scientific and Research Council of Turkey) BİDEB 2211-A. I would also like to thank the National Boron Research Institute of Turkey (Ulusal Bor Araştırma Enstitüsü (BOREN), Ankara, Turkey) (Grant No. 2012.ç0356) and COST (European Cooperation in Science and Technology) action-112S047 funded parts of the research discussed in this dissertation.

I acknowledge Dr. Alper Dilli for the many valuable discussions that helped me understand my research area better and Mr. Erdeniz Yurdakul, a fine technician who

kept me in technical assistance during my study in Chapter 2. In particular, I am grateful to the hospital staff, especially to Mr. İbrahim Ulusoy during *in vivo* studies.

I would like to express my special thanks to Melis Şardan Ekiz for her valuable contributions in the synthesis and characterization of the SPIONs and PAs used in study in Chapter 2. She helped me to improve my view of science especially during the experimental design and academic writing. I am also grateful to Ömer Faruk Sarioğlu and Refiye Tekiner for their fruitful collaboration and contributions to my studies in Chapter 3 and 4.

I thank my fellow NBT and BML lab mates for the stimulating discussions, interchanging ideas, and for all the fun we have had at UNAM. I would also like to thank Gözde, Göksu, Seren, Gökhan, Nuray and Melike for exchanges of knowledge and skills, which helped enrich the experience and improve my knowledge during my graduate program. A very special thanks goes out to Merve for her geniality and supports during the problems I faced with. For moral support, I thank to Büşra, Seyran, Hacer, Adile and Fatma who are my best friends.

I would like to thank Prof. İhsan Dođramacı, the founder of Bilkent University for giving opportunity to study in an international unique environment to conduct high impact research.

I would like to thank to my parents, my sister Gülsüm, my brother Hasan Hüseyin and my husband Salih who always supported and encouraged me with their best wishes.

Finally, this dissertation is dedicated to my son, who has been not only my source of love but also the motivating force throughout my dissertation.

## Contents

ABSTRACT.....	i
ÖZET.....	iii
Acknowledgement.....	v
Contents .....	vii
List of Figures .....	xiii
List of Tables.....	xvi
Abbreviations .....	xvii
<b>Chapter 1</b> .....	1
<b>INTRODUCTION</b> .....	1
1.1 Cancer.....	2
1.1.1 Cancer Diagnosis and Therapy .....	4
1.1.2 Importance of Material - Biomacromolecule Interactions .....	24
<b>Chapter 2</b> .....	26
<b>BIOACTIVE PEPTIDE AMPHIPHILE FUNCTIONALIZED SUPERPARAMAGNETIC IRON OXIDE NANOPARTICLES (SPIONs) FOR IN VIVO TUMOR IMAGIG</b> .....	26
2.1 INTRODUCTION .....	27

2.2 RESULTS and DISCUSSION .....	31
2.2.1 Synthesis and Characterization of the Nanoparticles .....	31
2.2.2 <i>In vitro</i> Cytotoxicity and Uptake Studies .....	35
2.2.3 <i>In vivo</i> Cancer Model.....	42
2.2.4 <i>In vivo</i> Magnetic Resonance Imaging (MRI) Studies.....	44
2.2.5 Histological Examination and Tissue Distribution of SPION/K-PA .....	50
2.3 CONCLUSION .....	56
2.4 EXPERIMENTAL SECTION .....	57
2.4.1 Materials .....	57
2.4.2 Synthesis of superparamagnetic iron oxide particles.....	57
2.4.3 Peptide amphiphile (PA) synthesis.....	58
2.4.4 Surface coating of SPIONs.....	59
2.4.5 Morphological characterization of SPIO nanoparticles.....	59
2.4.6 Particle size and zeta potential analysis.....	59
2.4.7 Iron content determination.....	60
2.4.8 PA content determination .....	61
2.4.9 <i>In vitro</i> studies .....	61
2.4.9.1 Cell viability analyses.....	62
2.4.9.2 SPION accumulation analyses in cells .....	62
2.4.9.3 Microtube formation assay .....	63

2.4.10 Animal breast cancer model .....	63
2.4.11 MRI analyses .....	64
2.4.12 Histological analyses .....	66
2.4.13 Statistical analysis.....	66
<b>Chapter 3</b> .....	<b>67</b>
<b>INTERACTIONS BETWEEN METAL IONS AND BIOMACROMOLECULES</b> .....	<b>67</b>
3.1 INTRODUCTION .....	68
3.2 RESULTS and DISCUSSION .....	71
3.2.1 Binding of DNA with Metal Ions .....	71
3.2.1.1 Characterization of the Binding of Metal Ions to DNA by UV-Visible (UV-Vis) Absorbance Spectroscopy .....	71
3.2.1.2 Competitive Binding of Au(III) and Ga(III) Ions with EtBr-DNA Mixture .....	73
3.2.1.3 Analysis of Conformational Changes .....	74
3.2.1.4 Thermodynamics of DNA Binding .....	76
3.2.1.5 Investigation of Metal Ion Binding by Vibrational Spectroscopy.....	79
3.2.2 HSA Studies .....	83
3.2.2.1 Analysis of Electronic Spectra to HSA .....	83
3.2.2.2 Analyses of Effects of Binding of Metal Ions to Fluorescence Emission of HSA.....	85

3.2.2.3	Calorimetric Investigation of the HSA-Metal Ion Binding .....	87
3.2.2.4	Analysis of Effects of Metal Ions on the FT-IR Spectra of HSA.....	89
3.2.2.5	Antitumor Activities of Au(III) and Ga(III) Ions .....	91
3.3	CONCLUSION .....	92
3.4	EXPERIMENTAL SECTION .....	94
3.4.1	Materials .....	94
3.4.2	UV-Vis absorbance spectroscopy .....	94
3.4.3	EtBr displacement assay .....	95
3.4.4	CD spectroscopy .....	95
3.4.5	ITC .....	96
3.4.6	FT-IR spectroscopy .....	96
3.4.7	Fluorescence spectroscopy .....	97
3.4.8	Cell culture and viability assay .....	97
<b>Chapter 4</b>	.....	<b>98</b>
	<b>INTERACTIONS BETWEEN BIOMACROMOLECULES AND BORIC ACID</b>	
	<b>OR BORON COMPOUNDS</b> .....	<b>98</b>
4.1	INTRODUCTION .....	99
4.2	RESULTS and DISCUSSION .....	102
4.2.1	DNA Binding Characteristics of BA .....	102
4.2.1.1	The Effects of Interaction of BA with DNA to Its Absorbance .....	102

4.2.1.2 Investigation of Conformational Transition of DNA .....	104
4.2.1.3 Morphological Investigation of DNA-BA Interactions.....	106
4.2.1.4 Effects of BA Treatment on FT-IR Spectra of DNA.....	107
4.2.1.5 Analysis of Thermodynamics of BA-DNA Binding .....	110
4.2.2 DNA Binding Characteristics of Boron Compounds .....	112
4.2.2.1 Spectroscopic Confirmation of the Interaction of Borates with DNA	112
4.2.2.2 Competitive DNA Binding Between EtBr and Borates .....	116
4.2.2.3 Investigation of Effects of Borate on DNA Damage.....	118
4.2.2.4 Analysis of Effects of Borates on DNA Conformation .....	120
4.2.2.5 Structural Analysis of DNA-Borate Binding.....	122
4.2.3 HSA Binding Characteristics of Boron Compounds.....	129
4.2.3.1 Binding Studies Using UV-Vis Spectra .....	129
4.2.3.2 Fluorescence Quenching of HSA by Boron Compounds.....	131
4.2.3.3 Analysis of Protein Conformation .....	133
4.2.3.4 Structural Analysis of HSA Binding of Borates.....	135
4.2.3.5 Cytotoxicity of Boron Compounds on HUVECs .....	138
4.3 CONCLUSION .....	139
4.4 EXPERIMENTAL SECTION .....	141
4.4.1 Materials and solutions .....	141
4.4.2 UV-Vis absorbance spectroscopy.....	141

4.4.3 EtBr displacement assay .....	142
4.4.4 TEM.....	142
4.4.5 ITC .....	143
4.4.6 DNA cleavage and mobility experiments.....	143
4.4.7 Fluorescence measurements .....	143
4.4.8 CD spectroscopy.....	144
4.4.9 FT-IR spectroscopy .....	145
4.4.10 Cytotoxicity assay.....	146
<b>Chapter 5</b> .....	147
<b>CONCLUSION and PROSPECTS</b> .....	147
Bibliography.....	152
Appendix .....	168

## List of Figures

Figure 1.1 Medical imaging techniques.....	6
Figure 1.2 Schematic illustration of physicochemical mechanisms to alter MRI contrast.....	8
Figure 1.3 Schematic illustration of relaxations of magnetic particles.....	9
Figure 1.4 Schematic illustration of hysteresis loop of superparamagnetic materials.....	12
Figure 1.5 Active and passive targeting strategies.....	19
Figure 1.6 Cellular uptake and specificity of gold nanoparticles.....	23
Figure 2.1 Images of hydrophobic iron oxide nanoparticles in the absence and presence of magnetic field and chemical structures of PA molecules.....	33
Figure 2.2 DLS analysis to determine the dispersion stability of K-PA coated SPIONs and LPPR coated SPIONs.....	34
Figure 2.3 Dose-dependent cytotoxicity profiles of PA coated SPIONs and free PAs on different cell lines.....	38
Figure 2.4 Viability of HUVECs.....	39
Figure 2.5 Prussian blue assay of HUVECs.....	40
Figure 2.6 Tube formation on Matrigel.....	41
Figure 2.7 Chemically induced breast cancer progression in female Spraque-Dawley rats.....	43
Figure 2.8 <i>In vivo</i> MRI.....	46
Figure 2.9 MR images from healthy rats.....	47
Figure 2.10 <i>In vivo</i> MR images from tumor bearing rats.....	48

Figure 2.11 Quantification of signal intensity changes.....	49
Figure 2.12 H&E staining for analyzing the tissue morphology of the kidney, liver and spleen of healthy rats.....	52
Figure 2.13 H&E staining for analyzing the tissue morphology of the kidney, liver and spleen of tumor bearing rats.....	53
Figure 2.14 Prussian blue staining for investigating iron accumulation in the tumor of rats.....	54
Figure 2.15 Prussian blue staining for analyzing iron accumulation in the liver, kidney and spleen of healthy rats.....	54
Figure 2.16 Prussian blue staining for investigating iron accumulation in the tumor, kidney, liver and spleen of tumor bearing rats.....	55
Figure 2. 17 MRI procedure.....	65
Figure 3.1 UV-Vis absorbance spectra of CT DNA-metal system.....	72
Figure 3.2 CD spectra of CT DNA titrated with metal ions .....	75
Figure 3.3 ITC final thermograms of Au(III)-DNA and Ga(III)-DNA bindings.....	78
Figure 3.4 FT-IR spectra of CT DNA in the presence of Au(III), and Ga(III) ions ..	81
Figure 3.5 Absorption spectra of HSA with various amount of metal ions.....	84
Figure 3.6 Fluorescence spectra of HSA in the presence of metal ions.....	86
Figure 3.7 ITC final thermograms of Au(III)-HSA, and Ga(III)-HSA bindings.....	88
Figure 3.8 Representative spectrum of curve-fitted amide I region of HSA. ....	90
Figure 3.9 Alamar blue cytotoxicity assay.....	91
Figure 4.1 UV-Vis spectra of CT DNA in the presence and absence of BA. ....	103
Figure 4.2 CD spectra of free DNA and BA- DNA mixtures BA .....	105
Figure 4.3 TEM observation of free CT DNA, BA, and CT DNA-BA mixture. ....	106

Figure 4.4 FT-IR spectra of DNA-BA mixtures. ....	108
Figure 4.5 ITC data for the titration of BA into CT DNA .....	111
Figure 4.6 Chemical structures of ule and col.....	113
Figure 4.7 UV-Vis spectra of CT DNA in the presence and absence of boron compounds. ....	114
Figure 4.8 UV-Vis spectra of boron compounds in the presence and absence of different concentrations of CT DNA.....	115
Figure 4.9 Gel electrophoresis .....	119
Figure 4.10 CD spectra of CT DNA in the presence of borates. ....	121
Figure 4.11 FT-IR spectra of CT DNA-ule mixtures.....	125
Figure 4.12 FT-IR spectra of CT DNA-col mixtures.....	126
Figure 4.13 FT-IR difference spectra of CT DNA-ule mixtures and CT DNA-col mixtures.....	127
Figure 4.14 FT-IR second-derivative spectra of CT DNA-borates.....	128
Figure 4.15 UV-Vis spectra of free HSA and different molar ratios of HSA-boron compound complexes.....	130
Figure 4.16 Fluorescence emission spectra of HSA-borate complexes. ....	132
Figure 4.17 CD spectra of HSA-ule and HSA-col interactions .....	134
Figure 4.18 FT-IR spectra and difference spectra of HSA-ule and HSA-col .....	136
Figure 4.19 Variations in HUVEC viability after borate treatment .....	138

## List of Tables

Table 3.1 Relative fluorescence ratios of EtBr-CT DNA mixture after incubation with metal ions .....	73
Table 3.2 Thermodynamic parameters obtained by ITC .....	78
Table 3.3 Peak positions and spectral shifts of the metal ions-DNA complexes.....	82
Table 3.4 Thermodynamic parameters obtained by ITC analysis for the binding of HSA with Au(III) or Ga(III) ions.....	88
Table 3.5 Secondary structure of HSA upon treated with Au(III) or Ga(III) ions.....	90
Table 4.1 The relative fluorescence intensity ratios with respect to varying concentrations of BA.....	103
Table 4.2 FT-IR of the free CT DNA and CT DNA-BA complexes.....	109
Table 4.3 EtBr displacement assay .....	117
Table 4.4 Curve fitting analysis of free HSA and protein incubated with borates ..	137

## Abbreviations

<b>ANOVA</b>	: Analysis of variance
<b>Au</b>	: Gold
<b>BA</b>	: Boric acid
<b>BNCT</b>	: Boron neutron capture therapy
<b>CCD</b>	: Charge-coupled device
<b>CD</b>	: Circular dichroism
<b>Co</b>	: Cobalt
<b>Col</b>	: Colemanite
<b>CT</b>	: Computed tomography
<b>CT DNA</b>	: Calf thymus deoxyribonucleic acid
<b>DLS</b>	: Dynamic light scattering
<b>DMBA</b>	: 7,12-Dimethylbenz(a) anthracene
<b>DMEM</b>	: Dulbecco's modified Eagle's medium
<b>DMF</b>	: Dimethylformamide
<b>DNA</b>	: Deoxyribonucleic acid
<b>EPR</b>	: Enhanced permeability and retention
<b>EtBr</b>	: Ethidium Bromide
<b>FBS</b>	: Fetal bovine serum

<b>FDA</b>	: Food and drug administration
<b>FT-IR</b>	: Fourier transform infrared
<b>Ga</b>	: Gallium
<b>Gd</b>	: Gadolinium
<b>HBTU</b>	: Hexafluorophosphate
<b>H&amp;E</b>	: Hematoxylin-eosin
<b>HPLC</b>	: High-performance liquid chromatography
<b>HSA</b>	: Human serum albumin
<b>HUVEC</b>	: Human umbilical vein endothelial cell
<b>IR</b>	: Infrared
<b>MCF-7</b>	: Human breast adenocarcinoma cell
<b>MDA-MB-453</b>	: Human metastatic breast carcinoma cell
<b>Mn</b>	: Manganese
<b>MRI</b>	: Magnetic resonance imaging
<b>MSN</b>	: Microporous silica nanoparticles
<b>NRP-1</b>	: Neuropilin-1
<b>PA</b>	: Peptide amphiphile
<b>PBS</b>	: Phosphate buffered saline
<b>PET</b>	: Positron emission tomography
<b>Pt</b>	: Platinum

<b>PVA</b>	: Polyvinyl alcohol
<b>QDs</b>	: Quantum dots
<b>RES</b>	: Reticuloendothelial system
<b>RF</b>	: Radiofrequency
<b>ROI</b>	: Region of interest
<b>ROS</b>	: Reactive oxygen species
<b>Ru</b>	: Ruthenium
<b>SEM</b>	: Standard error of the mean
<b>SPECT</b>	: Single-photon emission computed tomography
<b>SPION</b>	: Superparamagnetic iron oxide nanoparticle
<b>TCP</b>	: Tissue culture plate
<b>TEM</b>	: Transmission electron microscopy
<b>TFA</b>	: Trifluoroacetic acid
<b>TIS</b>	: Triisopropylsilane
<b>Trp</b>	: Tryptophan
<b>Ule</b>	: Ulexite
<b>US</b>	: Ultrasound
<b>UV-Vis</b>	: UV visible
<b>VEGF</b>	: Vascular endothelial growth factor
<b>VEGFR</b>	: Vascular endothelial growth factor receptor

# **Chapter 1**

## **INTRODUCTION**

## 1.1 Cancer

Cancer is a complex disease characterized by the uncontrolled tissue growth and abnormal cell spreading. The accumulation of spontaneous or inherited genetic mutations<sup>1</sup> and several molecular alterations are the main reasons of cancer<sup>2</sup>. Other factors that result in cancer are external factors, such as tobacco<sup>3</sup> or excessive sun exposure<sup>4, 5</sup>, infectious organisms such as human papillomavirus<sup>6, 7</sup>, hepatitis B<sup>8</sup> and C virus<sup>9</sup>, human immunodeficiency virus, or *Helicobacter pylori*<sup>10</sup>, unhealthy diet<sup>11</sup>, obesity<sup>12</sup>, physical inactivity<sup>13</sup>, as well as internal factors, such as hormones<sup>14</sup>, and immune conditions<sup>1, 15</sup>. Generally, the presence of one or more of these factors results in a detectable cancer within ten or more years.

In the US, cancer is the second most common disease<sup>16</sup>. It is reported that approximately 14.5 million cancer patients survived until 2014 and it is expected that this value will increase nearly 1.6 million in 2015<sup>17</sup>. On the other hand, there is a significant increase in the incidence of cancer cases in our country. Each year thousands of cancer cases are diagnosed in Turkey and the most commonly diagnosed cancer type is the lung cancer among men, while breast cancer is the most frequent cancer type among women according to the results of the Ministry of Health of Turkey<sup>18</sup>.

Although screening offers an opportunity for the diagnosis of cancer in early stages, it is not enough to provide extensive treatment and better outcomes. The early prognosis and treatment of cancer, before symptoms appear, remain poor with current imaging and therapeutic modalities in oncology clinic. Unfortunately, more than half of cancer patients have metastasized cancer cells that invade other organs of the body when

cancer is detected, which reduce the effectiveness of treatment and increase mortality rate for cancer of the breast, colon, rectum, cervix, and lung<sup>19</sup>.

Some of the cancer biomarkers alter their expressions according to biological conditions. They are genes, microRNAs<sup>20</sup>, proteins, lipids, carbohydrates, and small metabolite molecules<sup>19</sup>. They can be used as early cancer indicators which are often over-expressed in tumor cells rather than healthy cells such as gastrin-releasing peptide receptor for breast, colon, lung, and especially prostate cancer<sup>21</sup>, L-ferritin receptors for breast cancer<sup>22</sup>, KIT protein for gastrointestinal stromal tumors<sup>23</sup>, MMR enzyme loss for Lynch syndrome which is associated with malignant colon<sup>24</sup>, rectum, endometrium, stomach and small bowel cancer<sup>23</sup>, prostate-specific membrane antigen for prostate cancer, and VEGF/VEGFRs for tumor angiogenesis<sup>25</sup>. By using these biomarkers as targets, not only could we predict tumor characteristics such as metastasis, hormone dependence, induction of angiogenesis, but also it could facilitate decision making for diagnosis and treatment of cancer accurately. As an example, Neuropilin-1 (NRP-1) is a transmembrane glycoprotein co-receptor of vascular endothelial growth factor (VEGF) and is highly expressed in cancer cells to promote angiogenesis of tumor tissue. Depending on this molecular mechanism, human monoclonal anti-NRP-1 antibody MNRP1685A was developed for the treatment of advanced solid tumors and further modification was done by combining anticancer drugs such as bevacizumab and paclitaxel to increase efficiency of therapy<sup>26, 27</sup>.

In addition to early diagnosis of cancer, we also need to improve quality of the life of cancer survivors with further advancements in diagnosis and subsequently monitoring tumor progression, metastasis, and then effectiveness of the therapy with high

specificity<sup>21</sup>. Also, in order to develop novel imaging agents and new anticancer agents, the exact mechanism of action of these agents and their effects in biological systems need to be investigated.

### **1.1.1 Cancer Diagnosis and Therapy**

Multidisciplinary approaches have led to biomedical imaging modalities which are not only highly sensitive, but also have good resolution properties. These techniques have assisted us in understanding the biological phenomena and diagnose several diseases over the last few decades. Currently, detection of diseases are based on several chemical or biological clinical tests, histopathological analysis of tissue specimen, as well as imaging techniques. In order to detect tumor at early stage, managing disease course in patients, and decrease mortality rate of cancer patients, diagnostic screening methods and cancer therapy agents should urgently be improved.

Imaging techniques are important for the diagnosis of cancer in early stages. They can be used for presenting accurate location of cancer cells, tumor morphology and cancer metabolism<sup>28</sup>. As imaging modalities, Positron emission tomography (PET), single-photon emission computed tomography (SPECT), computed tomography (CT), ultrasound (US), optical fluorescence imaging, and magnetic resonance imaging (MRI) are widely used. Their potential benefits and drawbacks are illustrated in Figure 1.1.

PET and SPECT are nuclear imaging methods which give information about the functional processes and metabolic activity, based on the used biologically active material. These conventional imaging techniques differ in terms of sensitivity, spatial resolution, used radioactive contrast agents and cost<sup>29</sup>.

CT uses X-ray for the detection of different tissues. Even though CT is non-invasive and has high resolution, radiation exposure during clinical examination may result in dangerous outcomes, such as induction of cancer<sup>30</sup>. Recent developments in nanotechnology lead to new alternative materials that perform better than aromatic iodinated contrast agents, such as gold nanorods, fullerenes and carbon nanotubes which can be functionalized by conjugation with several targeting agents in order to increase retention rate and tissue specific accumulation<sup>31</sup>.

Besides being an inexpensive and flexible imaging modality, US has widespread use for several applications. With the advances in technology, 3D imaging systems have been produced to get higher diagnostic accuracy of pathology<sup>32</sup>. Microbubbles have been used to increase sensitivity of US imaging. For selective assessment and treatment of inflammation<sup>33</sup>, ischemia–reperfusion injury, angiogenesis, and thrombosis, these microbubbles have been modified by a variety of targeting ligands and combined with drugs<sup>34</sup> over the last ten years. Furthermore, contrast-enhanced US method is capable of detecting early tumor angiogenesis by using microbubbles functionalized with echistatin<sup>35</sup>.

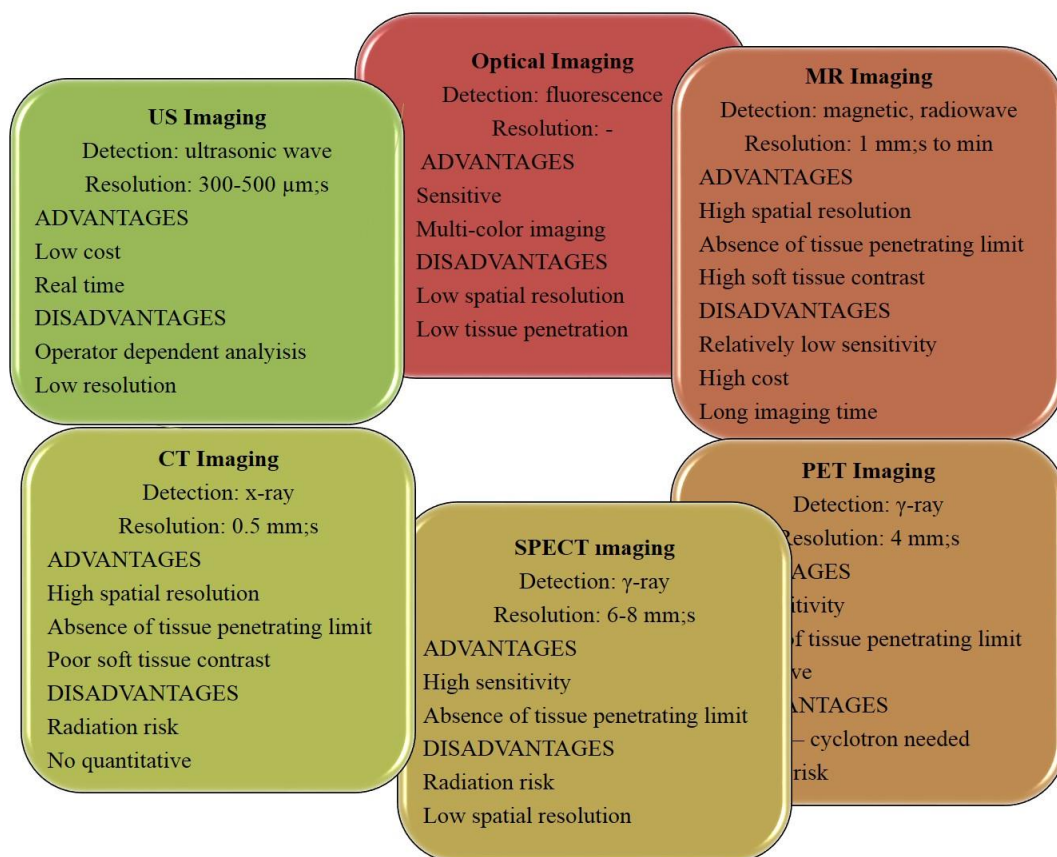


**Figure 1.1** Medical imaging techniques.

Optical or fluorescence imaging is based on photon detection by a charge-coupled device (CCD) camera. It is used for visualization of fluorescently labeled specific cells *in vitro* and *in vivo*. There are advantages and disadvantages of fluorescence imaging technique. It is relatively cost effective, portable and provides real time imaging. On the other hand, autofluorescence and limited light penetration depth may be problematic when you need high spatial sampling of photons propagating through animal tissues<sup>36</sup>. The most commonly used fluorophores are polymethines-organic dyes such as Cy5.5, Cy7<sup>37</sup> and indocyanine green which is FDA approved for clinical use<sup>38</sup>. Activatable fluorescent probes which do not emit light as unbound but give fluorescence by enzymatic activation if bound to its target inside the cell have newly

emerged<sup>38</sup>. It is possible to detect tumor early with highly sensitive fluorochromes that conjugate to overexpressed growth factor receptors on the cancer cells. For example, tumor specific fluorescence imaging was demonstrated in an ovarian cancer patient through the folate conjugated FITC in a pilot study<sup>39</sup>. For the diagnosis of breast cancer, Pham W. *et al.* synthesized Cy7 conjugated with AREPPTRTFAYWG peptide sequence that provides uMUC-1 antigen specific binding of the dye<sup>40</sup>. With the advances in nanotechnology new materials have been evaluated for *in vivo* molecular cancer imaging applications such as dye-containing silica or lipoprotein or calcium phosphate nanoparticles, quantum dots (QDs), inorganic fluorescent semiconductor nanocrystals, upconversion nanoparticles, Au nanoclusters and Ag nanoclusters<sup>28</sup>.

Radiology is accepted as “gold standard” for understanding the effectiveness of treatment and response of body to the applied treatment<sup>23</sup>. Up to now, the most widely used clinical and preclinical radiology imaging technique to detect physiological processes, anatomical details and disease state is MRI. The main reasons for the superiority of MRI are high spatial resolution at submillimeter scale, high contrast between soft tissues, being a noninvasive method and the absence of ionizing radiation during imaging. There are several parameters that affect signal intensity and distinct contrast in MR imaging. Some of them are proton relaxation rates, water proton densities, tumbling rates or time, field strength, acquisition sequence<sup>41</sup>, accessibility of water to the agent, electron spin state, MR frequency and (super)paramagnetism of the contrast agent<sup>42</sup>. These physicochemical mechanisms can be used to produce responsive contrast agents as well<sup>42</sup> (Figure 1.2).

Classically, the principle behind MRI can be explained as alignment of protons of water molecules in the presence of an external magnetic field ( $B_0$ ). Longitudinal magnetization is the alignment of proton nuclear spins in the same direction of  $B_0$  when radiofrequency (RF) pulse is applied.

In contrast, transverse magnetization occurs when the proton nuclear spins are aligned antiparallel with  $B_0$ . During transverse magnetization, longitudinal magnetization is reduced. Under a magnetic field, nuclear spin transition is called “spin flip” and its quantum state is expressed with the following formula:

$$\omega_0 = \gamma B_0$$

where  $\omega_0$  is Larmor frequency,  $\gamma$  is gyromagnetic ratio<sup>43</sup>.

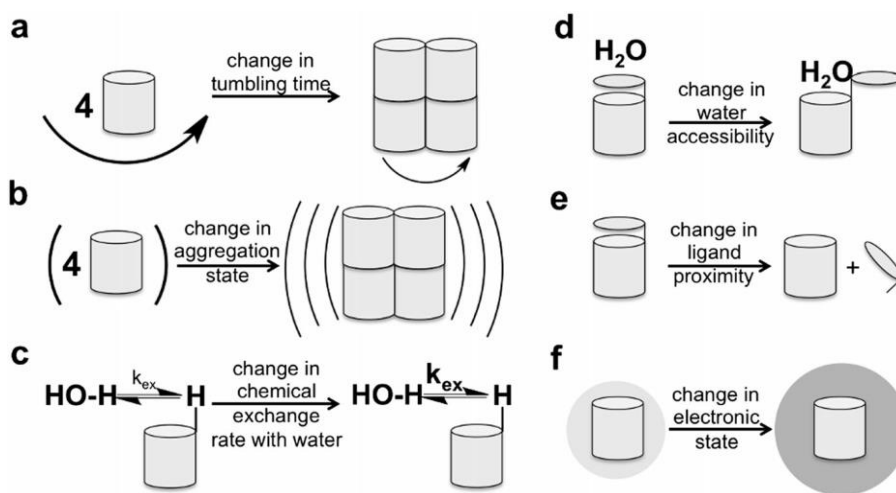


**Figure 1.2** Schematic illustration of physicochemical mechanisms to alter MRI contrast. Reproduced by permission of Wiley<sup>42</sup>.

After removal of the RF pulse, the excited water protons relax to the ground state by emitting the energy gained from the RF pulse. There are two different relaxation processes. Longitudinal (spin-lattice) relaxation which is known as T1, derives from

the longitudinal magnetization recovery. On the other hand, reduction of transverse magnetization resulting from the loss of phase coherence and dephasing between the proton nuclear spins produces transverse (spin-spin) relaxation known as T2 (Figure 1.3). Upon reconstruction of these signals with Fourier transform, gray scale images are obtained. Thus, images are sorted into two groups: T1-weighted images and T2-weighted images. The inverse of relaxations is called as relaxation rate “R1 or R2” ( $s^{-1}$ ). A brighter contrast is obtained if T1 relaxation rate (R1) is faster. Darker contrast is observed in the presence of a faster T2 relaxation rate (R2)<sup>43</sup>.

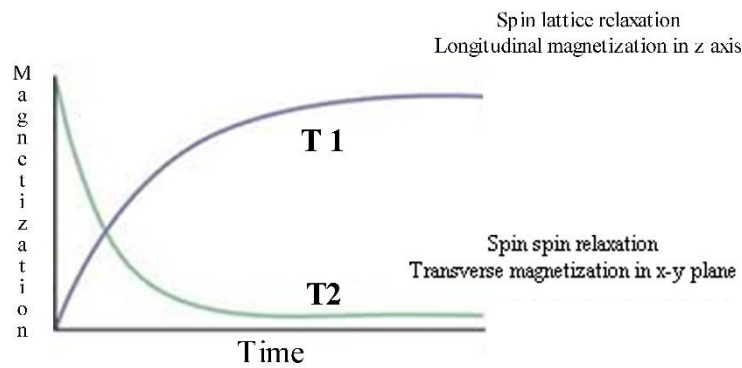


**Figure 1.3** Schematic illustration of relaxations of magnetic particles.

MRI gives more reliable results for clinicians in the diagnosis diseases related to invasion of structures when compare to CT and US <sup>44</sup>. If the contrast between diseased region and the healthy region is uncertain, it is sometimes very hard to detect the region of interest (ROI)<sup>43</sup>. Although low expression levels of some biomarkers and relatively low sensitivity (for example, false-positive rate of 10% for breast cancer, limited detection of small tumors or subtle anatomical changes<sup>43</sup>) of MRI limit its application in diagnosis of some of pathologies, using contrast agents can overcome these

limitations. The basic function of contrast agents is to accelerate magnetic relaxation to create much more contrast in RIO, which gives opportunity for discrimination between the pathological lesions and the healthy tissues. In 2010, approximately 35% of all clinical MRI in the USA was performed with the help of contrast agents<sup>45</sup>. There are two types of contrast agents: positive contrast agents result in brighter images, while negative contrast agents produce a darker image. Although they have strong contrast enhancement effects, their tissue specificity and selectivity need to be improved.

Contrast agents that are designed to enhance MRI signal comprise various materials, such as metals (gold, silver, and cobalt) and metal oxides ( $\text{Fe}_3\text{O}_4$ ,  $\text{TiO}_2$ , and  $\text{SiO}_2$ )<sup>46</sup>. Generally, T1 contrast agents demonstrate paramagnetic properties. The inorganic materials that have been applied clinically are mainly gadolinium ( $\text{Gd}^{3+}$ ) chelates which have unpaired electrons, a large magnetic moment and relaxivity ( $r_1$  and  $r_2$ ) values around  $4\text{--}6 \text{ mM}^{-1}\cdot\text{s}^{-1}$ <sup>47</sup>. Food and drug administration (FDA) and European agencies have approved Gd based contrast agents for clinical use<sup>48</sup>. In 1988, the first approved contrast agent was GdDTPA (gadopentetate dimeglumine, Magnevist®) for imaging of pathologies in liver and gastrointestinal system<sup>49</sup>. For a standard MRI scan, the minimum concentration of positive contrast agent is approximately 10 to 500  $\mu\text{M}$ , depending on the imaging system properties<sup>42</sup>. It is known that free Gd is very toxic. The exchange of Gd with other metal species, called transmetallation, and chelate dissociation due to the protonation of the ligands at acidic environment are the main factors for adverse effects of Gd chelates in the body<sup>50</sup>. The determined lethal dosage for mouse is  $0.2 \text{ mmol kg}^{-1} \text{ Gd}^{3+}$ . It causes well-known toxicity observed as nephrogenic systemic fibrosis, which is a serious syndrome, on human patients with

severe kidney failure. Rui *et al.* investigated toxicity of several T1 contrast agents using a mouse model. They observed that Gd accumulates in the liver, spleen, and especially kidneys<sup>48</sup>. *In vivo* studies also showed deposition of Gd in bone<sup>49</sup>. In a study performed by Kanazawa *et al.* commercially available gadolinium-diethylenetriamine pentaacetic acid (GdDTPA BMA, Omniscan®), was administered intravenously to the patients with bladder cancer. They reported that use of this T1 contrast agent gives opportunity for quantification and discrimination of bladder tumors and the normal bladder wall<sup>51</sup>. Gd based nanoparticles with minimum toxicity and prolonged circulation time have been evaluated after surface modifications by scientists. Li *et al.* reported potassium/gadolinium iron hexacyanoferrate nanoparticles can be used as positive MRI contrast agents and measured a relaxivity of  $12.3 \text{ mM}^{-1} \text{ s}^{-1}$ . Under infrared (IR) radiation, these nanoparticles convert IR energy to thermal energy which gives opportunity for cancer therapy<sup>52</sup>.

Due to their high magnetization properties, MnO containing materials have also been tested as T1 contrast agents. When compared to Gd(III) chelates, MnO contrast agents have more contrast enhancement potential in MRI. However their high toxicity often diminishes their clinical application. Potential severe effects of MnO have been studied by several researchers *in vitro* and *in vivo*<sup>48, 53-55</sup>. Chen *et al.* modified the surface of MnO nanoparticles with N-(trimethoxysilylpropyl) ethylene diamine triacetic acid (TETT) silane which increases water solubility and biocompatibility. In order to achieve glioma specific binding, these nanoparticle were further decorated with folic acid, which showed that these nanoparticles can be used for glioma diagnosis by MRI<sup>56</sup>. In another study, manganese oxide (MnO) nanocrystals with the size of 15-20 nm were incorporated into a pH sensitive polymer. This material generates bright

contrast when taken by low pH compartments in the cell such as lysosome<sup>57</sup>. Huang *et al.* synthesized and characterized a new T1 contrast agent for brain tumor imaging which was coated with HSA that provides long term stability and monodispersity of MnO nanoparticles in biological media. Unlike phospholipid-coated MnO nanoparticles ( $0.21 \text{ s}^{-1}\text{mM}^{-1}$ ), this modification does not cause a significant reduction in the relaxivity of material<sup>58</sup>.

For T2 weighted sequences, superparamagnetic iron oxide nanoparticles (SPION) have been clinically applied. Very small and single domain ferromagnetic particles demonstrate superparamagnetism where the energy barriers are relatively low with respect to thermal energy, and therefore the magnetization occurs with thermal excitations. In other words, superparamagnetic materials can be magnetized as soon as an external magnetic field is applied and their average magnetization is zero without a magnetic field like paramagnetic material but their magnetic susceptibility is larger than paramagnetic materials (Figure 1.4).

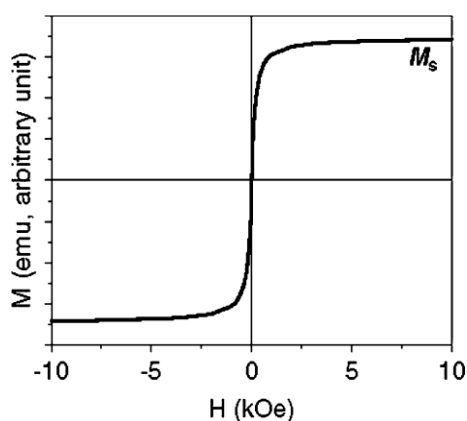


**Figure 1.4** Schematic illustration of hysteresis loop of superparamagnetic materials.

There are two sources for SPIONs: one of them is magnetite ( $\text{Fe}_3\text{O}_4$ ), other is maghemite ( $\gamma\text{-Fe}_2\text{O}_4$ )<sup>59</sup>. They have characteristically monocrystalline structure.

SPIONs with different coating agents and hydrodynamic sizes (ranging from 5 nm to 3500 nm) have been approved<sup>60</sup> as T2 contrast agents by the FDA or are in clinical development<sup>61</sup>. Some of the commercial ones are called Feridex = Endorem, Clariscan, Resovist = Cliavist, Sinerem and Abdoscan®.

In clinical study, researchers investigated MRI contrast enhancement of Resovist®, which is a reticuloendothelial system (RES) specific dextran coated SPION, with 1.5-T MR scanner. For liver lesions larger than 2 cm, these nanoparticles could be used for detection accurately (95.2%)<sup>62</sup>.

Yang *et al.* synthesized PEG coated SPIONs and functionalized with folate as tumor targeting ligand. They reported that these nanoparticles selectively accumulates in cancer cells both *in vitro* and *in vivo*. MRI of a mouse model revealed that the dark contrast generated from folate conjugated PEG coated SPIONs is significantly high at the tumor site rather than healthy tissue<sup>63</sup>. As an alternative strategy, hydrophobic SPIONs with 9.9 nm diameter were encapsulated into polymeric micelles and were functionalized with the attachment of RGD peptide for tumor  $\alpha_v\beta_3$  integrin imaging by MRI<sup>64</sup>.

In the literature, there are several studies about SPIONs prepared with different sizes and compositions by using different strategies and comparison of their contrast effects in MRI<sup>65-67</sup>. Combination of Co and Mn with iron oxide nanoparticles (CoFe<sub>2</sub>O<sub>4</sub> and MnFe<sub>2</sub>O<sub>4</sub>) also leads to more prominent T2 contrast enhancement. However, there are some considerations about the toxicity of these nanoparticles due to the production of free metal ions that may result in dangerous outcomes in nervous system<sup>68</sup>. Though iron oxide nanoparticles are typically considered negative contrast agents, SPIONs

with mean size of 5 nm or less demonstrate T1 MRI contrast effects. Some groups have developed hybrid systems by combining polymers and SPIONs to obtain dual T1/T2 responsive probe for tumor detection<sup>69-71</sup>.

SPIONs can be used for imaging of apoptosis, angiogenesis,  $\beta$ -amyloid accumulation, inflammation and gene expression via MRI<sup>72</sup>. On the other hand, biological applications of SPIONs are not restricted to MRI contrast enhancement. SPIONs can be used for tissue repair, immunoassay, detoxification of biological fluids, hyperthermia, drug delivery<sup>73</sup>, and cell separation purposes as well<sup>74</sup>.

Although SPIONs have several advantages such as biocompatibility and long blood circulation time, we have to take disturbance in iron homeostasis, oxidative stress, and altered cellular responses into consideration in clinical use<sup>73</sup>.

Thanks to the improvements in synthesis methodologies, there are important developments in the preparation of high quality magnetic nanoparticles. Synthesis methods of magnetic nanoparticles can be categorized into four groups: co-precipitation, thermal decomposition, microemulsion, and hydrothermal synthesis techniques. By using these methods, nanoparticles with different compositions and phases can be synthesized such as iron oxides, pure metals, alloys and ferromagnets. During nanoparticle production, the main purpose is to obtain highly stable, monodisperse, uniform, as well as size and shape controlled magnetic nanoparticles<sup>75</sup>.

Co-precipitation is one of the most common method for magnetic materials' synthesis, especially iron oxides. This process occurs under elevated temperatures or room temperature in the presence of base and inert atmosphere<sup>76</sup>. The physicochemical properties of the final products such as composition and size are mostly determined by

the content of the initially used salts, and the chemical properties of precipitation medium<sup>77</sup>. Although this method is very simple and fast, the nanoparticles synthesized with co-precipitation technique are very polydisperse.

The best and most common method for the synthesis of size and shape controlled magnetic nanoparticles is thermal decomposition technique which is performed at high temperatures (ranging from 240 to 320 °C) and needs organic solvents with stabilizing surfactants. Generally, metal acetylacetonates, metal cupferronates and carbonyls are used as precursors. Surfactants used as stabilizing agent include hexadecylamine, oleic acid or fatty acids such as decanoic acid, lauric acid, myristic acid, palmitic acid, oleic acid and stearic acid<sup>78</sup>. By changing the ratio of these two materials and hydrocarbon solvents, size, shape and composition of the product can be modified<sup>75</sup>. Nanoparticles with very narrow size distribution and very small size can be synthesized by this method. However, it is a little bit more complicated and time consuming technique than other methods. Nanoparticles synthesized with thermal decomposition method are generally not water soluble, thus they need a surface capping agent such as poly(ethylene glycol) (PEG) or dextran for biomedical applications. It is also noteworthy that water soluble nanoparticles can be obtained with this method if monocarboxyl-terminated PEG<sup>79</sup> or R, $\omega$ -dicarboxyl-terminated PEG are used as surface capping agent<sup>80</sup>.

Microemulsion method is also used to prepare magnetic nanoparticles at ambient conditions. This method depends on stabilization of two different thermodynamically stable isotropic dispersion of immiscible liquids by an interfacial film of surfactant molecules<sup>81</sup>. The most important disadvantage of microemulsion method is that

generally controlling shape, size and dispersity is very hard. Moreover, it is not an efficient method for magnetic nanoparticle synthesis, because you have to use large amounts of solvents for a little amount of product.

Another method for magnetic nanoparticle synthesis is hydrothermal method. Although this synthesis method is simple, high temperature (above 200 °C) and pressure conditions (higher than 2000 psi) are required for the production of size and morphology controlled materials<sup>80</sup>. Basic mechanism behind the hydrothermal method is the separation and phase transfer at the interfaces of the liquid, solid, and solution phases. However the detail of mechanism of hydrothermal method is unclear. In order to get monodispersed and uniform metal and metal oxide nanoparticles, a mixture of high-boiling-point reducing agent, electrostatic stabilizer and surfactant are required.

Nanoparticles obtained by methods mentioned before are generally unstable under physiological conditions. Therefore, they are stabilized with biocompatible materials which are monomeric stabilizers such as carboxylates or phosphates, inorganic materials such as gold and silica, or polymers such as dextran, PEG, polyvinyl alcohol (PVA), poly(D,L-lactide-co-glycolide (PDL)<sup>61</sup>, alginate, starch or chitosan<sup>80</sup> to prevent agglomeration or precipitation, and to improve colloidal stability in biological media. Up to now, the most powerful and common coating agent has been dextran, which is found on the surface of some FDA approved contrast agents for MRI<sup>82</sup>. *In vitro* and *in vivo* investigations revealed that dextran coating decreases toxicity of nanoparticles and it is biodegradable and improves their blood distribution profile<sup>83</sup>. Furthermore; dextran coated SPIONs give opportunity for attachment of targeting moieties on the surface of agent due to the tunable surface chemistry.

As an alternative to covalent attachment methods for surface coating of nanoparticles, hydrophobic interactions between alkyl chains of peptide amphiphile (PA) and lauric acid or laurylamine or octyl groups on the surface of nanoparticles can be used for the functionalization purposes<sup>84, 85</sup>. PAs are molecules containing a hydrophobic tail (usually double-chain lipids or single chain fatty acids) and a hydrophilic biologically active peptide headgroup (capable of mimicking functions of several biomolecules such as receptors) which are conjugated through a spacer<sup>86</sup>. Above the critical micelle concentration, PAs form soluble micelles. Incorporating a variety of targeting amino acid sequences to the PA micelles allows not only targeting but also imaging of several diseases like cancer<sup>87, 88</sup>.

Recently, significant progress has been made on the development of unique contrast agents with tumor targeting properties. These designs are generally based on conjugation of contrast agent with tumor specific ligands such as DNA, siRNA, aptamers, small molecules, peptides, proteins and antibodies<sup>89</sup> which are capable of binding selectively to cancer biomarkers or receptors for not only tumor targeted imaging but also non-invasive monitoring of molecular processes, and targeted drug delivery<sup>82</sup>. For instance, cyclic(RGDyK)-4-methylcatechol labeled monodispersed Fe<sub>3</sub>O<sub>4</sub> nanoparticles were used as integrin targeted T2 contrast agents and these ultrasmall nanoparticles have 60 mM<sup>-1</sup>s<sup>-1</sup> more relaxivity value than clinically used Feridex® nanoparticles<sup>90</sup>. Radermacher *et al.* designed a new SPION agent coated with PEG and functionalized with TLVSSL peptide sequence, which is called phosphatidylserine-targeted hexapeptide. This new contrast agent was tested in terms of necrotic tissue targeting after cancer treatment in an animal liver tumor model.

When compared to non-targeted nanoparticles, coupling of targeting ligand to the SPION induced a 3-fold higher accumulation in tumor site<sup>91</sup>.

Actually, the effective diagnosis and treatment of solid tumors depend on true understanding of cancer targeting for proper material design<sup>92</sup>. The well-known differences between tumor and healthy tissue are leaky blood vessels (due to the disordered tight junctions<sup>93</sup>) and impaired lymphatic system of the tumor tissue, namely enhanced permeability and retention (EPR) effect which could be used for accumulation of particles and drugs via active or passive targeting strategies (Figure 1.5). Size and shape are the most important factors for nonspecific accumulation of particles. Additionally, increasing blood concentration of a material enhances passive tumor targeting chance by preventing aggregation, precipitation and serum protein binding of nanoparticles. On the other hand, active targeting is achieved by coating of surfaces with tumor specific binding ligands. Chemical and physical properties of nanoparticles affect their uptake and interactions with biological substances as well<sup>92</sup>.

In one study, scientists compared the effect of size, coating and addition of a targeting ligand on the tumor accumulation of iron oxide nanoparticles *in vitro* and *in vivo*<sup>94</sup>. According to their observations, 30 nm nanoparticles accumulate more than particles with 100 nm size. Coating of nanoparticles with PEG did not result in significant differences between *in vitro* and *in vivo* uptake of nanoparticles. Furthermore, *in vivo* imaging of mice tumor tissue has been achieved by a monovalent Fab' fragment of Tmab (FDA approved monoclonal antibody for breast cancer targeting) moiety coupled to iron oxide nanoparticles. Antibody targeted nanoparticles with smaller size have greater tumor concentration than passively targeted nanoparticles because of high

washing out rate of nonspecific particles from neoplastic tissues. Several studies have explored that upon intravenous administration, materials with a molecular weight above the renal threshold (40 kDa) and diameter ranging from 10 to 150-200 nm tend to accumulate preferentially in tumor<sup>93</sup>.

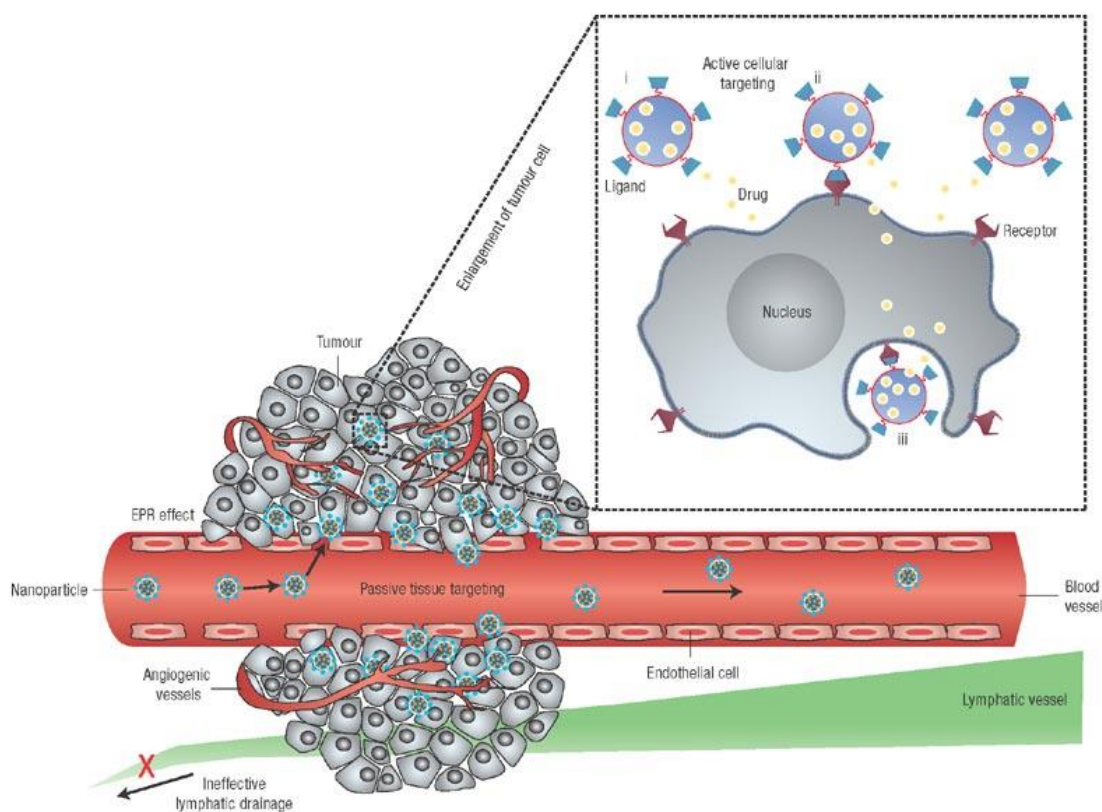


**Figure 1.5** Active and passive targeting strategies. Reprinted from reference [89] with permission<sup>89</sup>.

Currently used cancer management methods are surgery, radiation, chemotherapy, endocrinotherapy, immune therapy, and molecular targeted therapy. However, these

methods have limited advantages due to the poor effectiveness especially for metastatic disease with acquired resistance at late stage.

Nowadays, one important class of potential therapeutics are peptides that have high specificity and low toxicity for the treatment of diseases, which depend on angiogenesis. In the last decade, several promising amino acid sequences have been identified for the inhibition of cancer progression through preventing vessel formation. The advantages of peptides for cancer targeting are their small size which leads to good tissue penetration, functionalization capability which gives opportunity for encapsulation or surface coating of nanoparticles, and being a component of combination therapies<sup>95</sup>.

Actually, inorganic chemistry in medicine can be categorized into two different approaches: one of them utilizes ligands (metal ions in different forms; either free or bound to a biomacromolecule such as protein) as drugs, other uses metals as imaging agents previously discussed in detail<sup>96</sup>.

Herein, inorganic chemotherapeutics used in cancer treatment will be discussed in detail. The main mechanism of conventional cancer drugs is eliminating malignant cells without considering the presence of healthy cells in the environment. Although they usually manage their duty efficiently, their precision is insufficient and they have several adverse side effects such as nephrotoxicity<sup>97</sup>, ototoxicity, and allergy<sup>98</sup>. Research on chemotherapeutics for cancer is important for designing novel anti-cancer drugs against tumors to overcome the toxicity of these drugs and achieve more precision.

Over the past decade, metal based drugs have attracted attention because of their biological and pharmaceutical properties as anticancer agents. Metallopharmaceuticals such as BBR3464, satraplatin and picoplatin contain platinum (Pt), which binds to DNA and interferes with its normal function, halting DNA replication, and thereby leading to cell death. The most commonly used Pt containing potent anticancer drugs are cisplatin, carboplatin, oxaliplatin and KP1537. However acquired resistance after repeated administrations limits their medical use<sup>99</sup>. By mimicking superoxide dismutase (SOD) enzyme, Mn chelates can be used for cancer therapy. NAMI-A and KP1339, which are chemotherapeutic agents, include ruthenium (Ru) compound. Besides having strong complex forming ability with various ligands<sup>100</sup>, greater resistance to hydrolysis provide advantages to Ru compounds as anticancer drugs<sup>96</sup>. Other examples of use of inorganic compounds are Arsenix trioxide, namely Trisenox® for the treatment of acute promyelocytic leukaemia, gallium (KP46) for melanoma<sup>101</sup>, and lanthanum (KP772) for multi-drug resistant cancer<sup>102</sup>.

Several researchers have investigated the use of new metal (iron, copper, cobalt, zinc, cadmium and mercury) compounds for their antineoplastic potential<sup>103-107</sup>. One interesting study demonstrated that successful Gd neutron capture therapy was achieved by incorporation of Gd(III) chelates into calcium phosphate micelles without therapeutic drugs. This finding is important because this system can effectively accumulate in tumor tissue and disrupted cancer cells through  $\gamma$ -rays or electron emission from the Gd nuclides. Furthermore, being an MRI guided cancer targeting system facilitates imaging of tumor lesions and minimizing toxicity on healthy tissue<sup>108</sup>.

He *et al.* reported the anticancer properties of a gold(III) porphyrin complex (Au-1a) loaded microporous silica nanoparticles (MSN) denoted with RGD peptide which binds integrins overexpressed on cancer cells<sup>109</sup>. Cancer cell specific uptake of these nanoparticles by various cell lines and *in vitro* selective induction of apoptosis by gold encapsulated silica nanoparticles in a co-culture model were demonstrated (Figure 1.6). Time dependent and dose dependent accumulation of this silica-gold drug delivery system in cancer cells revealed the importance of targeting ligand for efficient therapy.

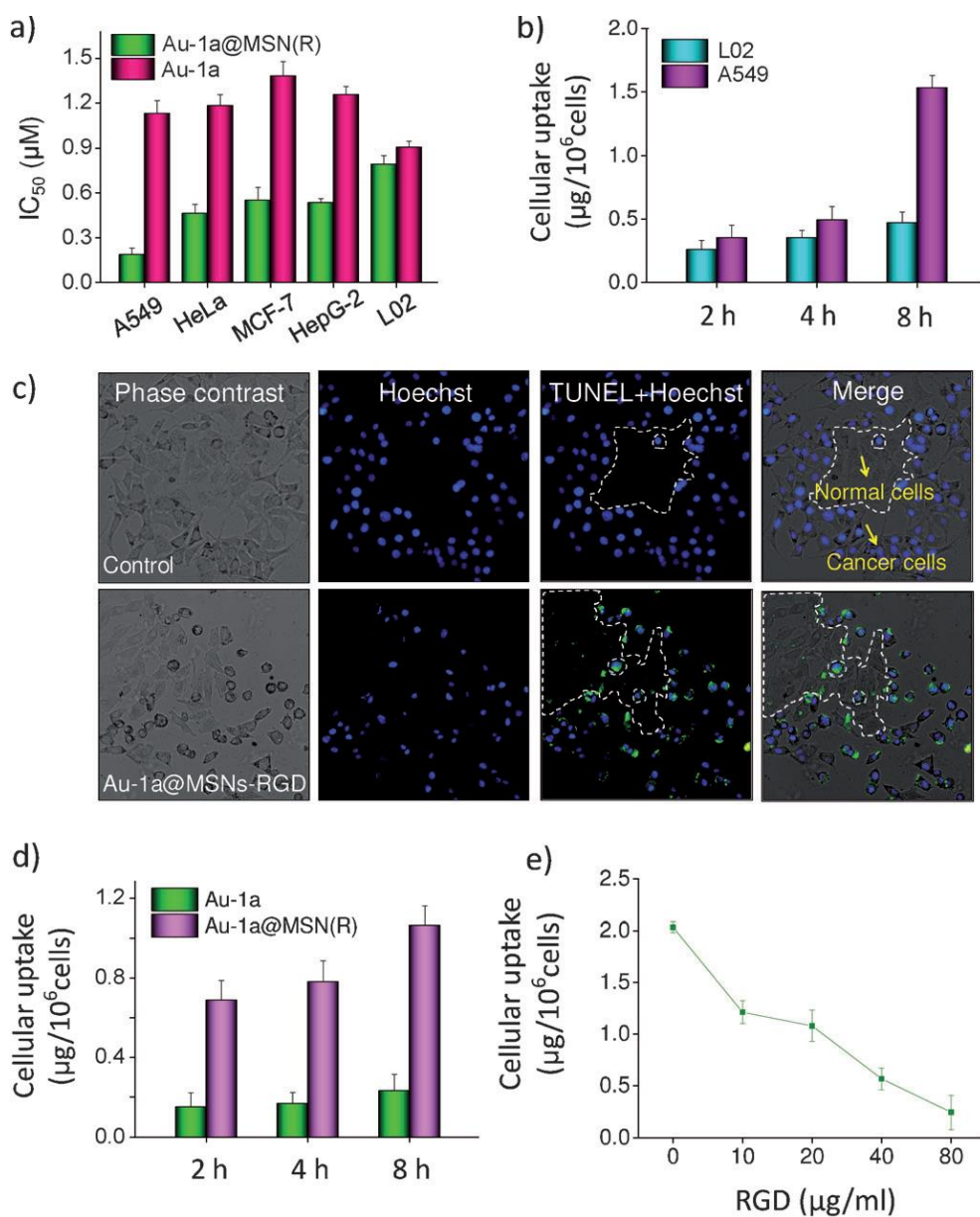


**Figure 1.6** Cellular uptake and specificity of Au-1a@MSN(R). a) Cytotoxicity of gold nanoparticles on different cell lines. b) Quantification of cellular uptake of nanoparticles in L02 normal human liver cells and A549 lung carcinoma cell lines. c) TUNEL-Hoechst 33342 co-staining of A549/L02 co-culture cells after treatment with gold nanoparticles. d) Quantification of time dependent cellular uptake of nanoparticles. e) Dose-dependent effects of RGD peptide on the cellular uptake of Au-1a@MSN(R). Reproduced by permission of Wiley<sup>109</sup>.

### **1.1.2 Importance of Material - Biomacromolecule Interactions**

Conventional cancer treatment is based on chemotherapy and radiotherapy. The discovery and characterization of new drug candidates have received a great deal of attention<sup>110</sup> to improve the quality of life of patients for those undergoing treatments. Up to now, although several different kinds of materials have been developed in order to increase effectiveness of cancer treatment, we still need to improve capabilities of these materials<sup>29</sup>. Significant improvements in both cancer diagnosis and treatment can be achieved through detailed understanding of the interactions between materials and biomolecules which provides important information about the effects of material on the target of interest in terms of thermodynamic and kinetic property changes toward biological molecules such as receptors and deoxyribonucleic acid (DNA), the metabolic fate in blood and pharmacological activity of material.

One of the most important application of inorganic compounds in medicine is cancer chemotherapy. There are extensive studies focusing on use and increasing effectiveness of these metal based antitumor drugs with fewer side effects. The detailed examination of the chemistry of the material, as well as the kinetics and affinity of material's interaction with its potential tumor related molecular targets can yield important insights into material design<sup>99</sup>.

Currently used chemotherapeutic agents generally demonstrate their function through DNA damage by binding to DNA and thereby inhibiting replication and transcription processes. For example; DNA is accepted to be the cellular target of a well-known and commonly used anticancer drug: cisplatin. The intercalation, groove binding and covalent binding are the main binding modes for an association between an agent and

DNA<sup>111</sup>. The extensive understanding of binding modes is important to assess the biological consequences of these DNA adducts. In literature, enormous efforts have been done to determine physical interaction of a compound with DNA by using several spectroscopic, calorimetric and molecular modeling methods<sup>111-114</sup>.

On the other hand, analyses of interaction between inorganic compounds with serum proteins are crucial to understand fate of them in blood stream and their pharmacokinetic behavior. Although efficient transfer of an agent to the target often requires serum protein binding as a drug delivery system, unwanted or random protein-metal ion interactions may result in toxicity. Human serum albumin (HSA) binding contributes significantly to the discovery of novel potential materials because it is capable of transporting various kinds of materials such as drugs<sup>115</sup>, metabolites, endogenous ligands, and metal ions<sup>116, 117</sup>. HSA is a globular protein structurally dominated by  $\alpha$ -helices. It has three homologous domains (I, II and III) and each contain two separate subdomains (A and B)<sup>118</sup>. Although they are very similar in terms of their structures, these domains demonstrate different binding properties. Most HSA-binding drugs bind to the IIA and IIIA domains, while metals utilize other binding sites; such as sites A and B, N-terminal binding sites, the Cys34 binding site and others<sup>119</sup>. In the presence of external small molecules, proteins undergo modifications in their secondary structure, which may affect their stability and binding properties<sup>120</sup>. Thanks to the physical and biophysical characterization techniques, it is possible to determine binding sites of several potential inorganic drug candidates and enhance cytotoxicity of compounds in cancer cells<sup>118, 121</sup>. Thus, HSA based carriers, hybrid systems and metal based drugs could be designed and developed rationally for biomedical applications.

## **Chapter 2**

**BIOACTIVE PEPTIDE AMPHIPHILE FUNCTIONALIZED  
SUPERPARAMAGNETIC IRON OXIDE NANOPARTICLES  
(SPIONs) FOR *IN VIVO* TUMOR IMAGIG**

## 2.1 INTRODUCTION

Breast cancer is the second most commonly diagnosed cancer type among women worldwide. According to the estimation from the National Cancer Institute, about 232,670 new cases were diagnosed in 2014, with 40,000 associated deaths due to the breast cancer in the US<sup>17</sup>. Mortality rate from breast cancer has been increasing each year all over the world. Breast cancer risk is two times higher if a woman has one or more affected first degree relatives diagnosed with breast cancer due to the inherited mutations in cancer susceptibility genes such as BRCA1 and BRCA2<sup>122</sup>. Aging is another factor for the development of breast cancer as well<sup>123</sup>.

Over recent years, enormous studies have focused on different diagnostic and therapeutic approaches to cancer. The most promising strategy has been based on tumor targeting with overexpressed specific receptors. The conjugation of these targeting molecules with contrast agents or drugs improves the selective uptake by tumor cells<sup>124</sup>. Judah Folkman proposed anti-angiogenic therapy in 1971<sup>125</sup>. Although angiogenesis is a physiological process by which new blood vessels are formed, it is also crucial for the tumor growth and metastatic spread of cancer cells by supplying nutrients and oxygen, as well as removing waste products<sup>126</sup>. The role of angiogenesis in supporting solid tumor growth is well documented. Most tumor endothelial cells produce high levels of VEGF, and VEGF receptors (VEGFRs). VEGF expression is up-regulated in response to hypoxia and often increases in regions of necrotic tumor. Neuropilin-1 (NRP-1) is a co-receptor for VEGF and its expression mediates angiogenesis and invasion<sup>127</sup> of several tumor cells, such as breast, prostate, neuroblastomas, astrocytomas, lung, pancreas, bile duct, gastric, colon cancers and melanoma cells<sup>128, 129</sup>. Each breast carcinoma cell has nearly  $1-2 \times 10^5$  NRP-1

molecules on its surface. There is a strong affinity between NRP-1 and VEGF165 but not VEGF121, because the NRP-1 binding site in VEGF165 is encoded by VEGF exon 7, which is absent in VEGF121<sup>127</sup>.

Recently, the short peptide sequence ATWLPPR, was identified by Starzec *et al.* through peptide libraries displayed on bacteriophage<sup>130</sup>. This peptide prevents the binding of VEGF165 to NRP-1 which plays role as an anti-angiogenic and anticancer agent. Positive MRI contrast enhancement of a multifunctional nanoparticle including silica nanoparticles with gadolinium chelate and ATWLPPR peptide as tumor targeting ligand was tested in a rat intracranial U87 glioblastoma model<sup>131</sup>. The intratumoral retention of ATWLPPR-targeted nanoparticles was higher than the non-targeted nanoparticles which demonstrates tumor cell selectivity of this peptide sequence. It has reported that the shortest amino acid sequence interacting with NRP-1 coreceptor is LPPR. In this study, I used LPPR as an antiangiogenic tumor vascularate targeting peptide to hinder the interaction between VEGF and NRP-1 required for angiogenesis of cancer tissue.

Breast exam and mammography are often used to detect breast cancer at an early stage. Although mammography can detect tumor and contribute to treatment of patients, this technique is insufficient if patient is young or has dense breast tissue. MRI is a powerful medical imaging modality for high resolution visualization of the cancer non-invasively. Tissue anatomic structures can be monitored through the detection of magnetization of water protons in the presence of a strong magnetic field. Normal and pathological tissues may have different intrinsic relaxation times depending on their physiological environment, specific contrast can be observed between the site of

interest and the surrounding regions at advanced stages of disease<sup>132</sup>. The sensitivity of MRI can be greatly enhanced by using contrast agents such as SPIONs which increase the signal-to-noise ratio. SPIONs are already used in clinic as contrast agents in MRI (Feridex®, Endorem®, Gastromark®, Sinerem®) for the diagnosis of liver or lymph node pathologies and diseases of the bowel wall or mesentery.

Recent advances in the development of surface modified nanoparticles have increased use of MRI for cancer diagnosis<sup>133</sup>. Several groups have reported that tumor specific MRI T2 imaging agents are biocompatible, biodegradable and have long blood circulation time, which provide high accumulation in the tumor tissue<sup>134, 135</sup>. As contrast agents, iron oxide nanoparticles which are known to be strong enhancers of proton spin–spin relaxation, provide several opportunities in the accurate diagnosis of cancer<sup>135</sup>. The size and coating of nanoparticles strongly influence their contrast enhancement and tumor targeting properties. There are currently several efforts under way to reduce hydrophobic interactions between SPIONs and biological molecules by coating the surface of nanoparticles with different synthetic and natural chemical moieties that also give opportunity for the functionalization of nanoparticles for target specific interaction<sup>74</sup>. Attachment of a biomarker associated with tumor metastasis and/or progression on the surface of nanoparticles is an effective approach towards the early detection of cancer<sup>136</sup> which is called active targeting. Also, nanoparticles can passively accumulate at tumor site due to their small size as discussed in previous chapter. For example, iron oxide nanocubes encapsulated with polyethylene glycol-phospholipid have been shown to increase sensitivity in tumor imaging compared to Feridex<sup>137</sup>. Lee and coworkers have developed branched PEI and PEG coated SPIONs

that are able to bind to negatively charged plasmid DNA due to the positive charge on their surface and are detectable at the tumor site by MRI<sup>138</sup>.

Our group previously reported that lauric acid and laurylamine capped hydrophobic SPIONs can be noncovalently functionalized with peptide amphiphile (PA) molecules through hydrophobic interactions to render them water soluble and biocompatible<sup>84</sup>.

We hypothesized that LPPR coated SPIONs could actively reach the cancerous tissue following systemic administration *in vivo*. On the other hand, K-PA coated SPIONs without a tumor targeting moiety were used as a control. We further hypothesized that the MRI negative contrast enhancement of PA functionalized SPIONs could be utilized to monitor breast tumors noninvasively and to evaluate the effect of SPIONs on the time course of distribution and elimination from tumor and different organs. In this chapter, I demonstrated noncovalent coating of SPIONs with proline-rich PAs, and investigated the efficiency of this superparamagnetic, water-dispersible hybrid system in enhancing the MR imaging of tumor tissue in rats. The potentials of PA functionalized SPIONs as an MRI contrast agent were assessed in Sprague-Dawley rats with mammary gland tumors. In particular, the cellular viability and uptake behavior of the SPION/PA system were investigated using different healthy and cancer cell lines, while the biodistribution and bioelimination of the nanoparticles were investigated by MRI and histological examination in animal tumor model.

## 2.2 RESULTS and DISCUSSION

### 2.2.1 Synthesis and Characterization of the Nanoparticles

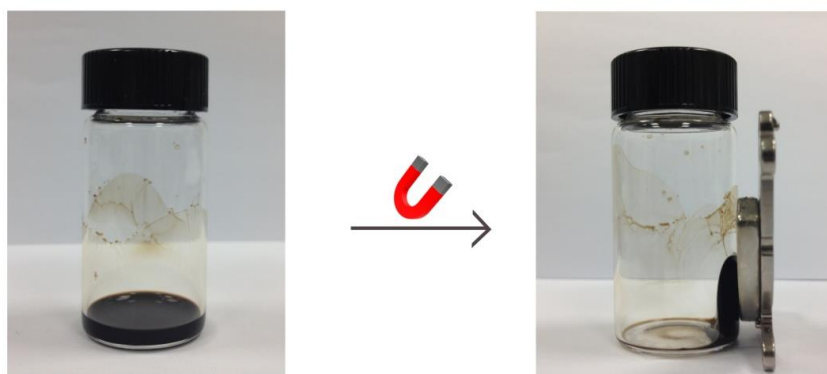
Thermal decomposition is an effective method for the production of iron oxide nanoparticles with minimal variance in shape and size<sup>76</sup>. Although the method results in the formation of water insoluble nanoparticles and requires further modification for the efficient dispersion in the aqueous environment, it provides higher stability and significant control over the size and shape of the nanoparticle compared to co-precipitation, which is another common method for nanoparticle synthesis<sup>80</sup>. Here, iron oxide ( $\text{Fe}_3\text{O}_4$ ) nanocrystals were synthesized through thermal decomposition strategy. These nanoparticles were hydrophobic and dispersed in a non-polar organic solvent, hexane (Figure 2.1a). The iron oxide nanoparticles, which were prepared via thermal decomposition method, had with an average size of 4-16 nm and displayed superparamagnetic characteristics<sup>139</sup> and was verified by vibrating sample magnetometer (VSM) measurements<sup>85</sup> in previous study by Guler group.

A variety of methods are available to increase the water-solubility and enhance the dispersion stability of SPIONs in physiological conditions, which is critical for the *in vivo* applicability of nanoparticles. Principal among these methods are the ligand addition or ligand exchange approaches<sup>140</sup>. In the former method, noncovalent interactions, such as electrostatic interactions, hydrophobic interactions and hydrogen bonding, are the major driving forces for the physical adsorption of molecules to the surface of SPIONs. Amphiphilic macromolecular ligands and liposomes have been used for the preparation of water-dispersible SPIO nanocomposites<sup>135</sup>. In this study, PA molecules were utilized in the production of SPION/PA nanocomposites to

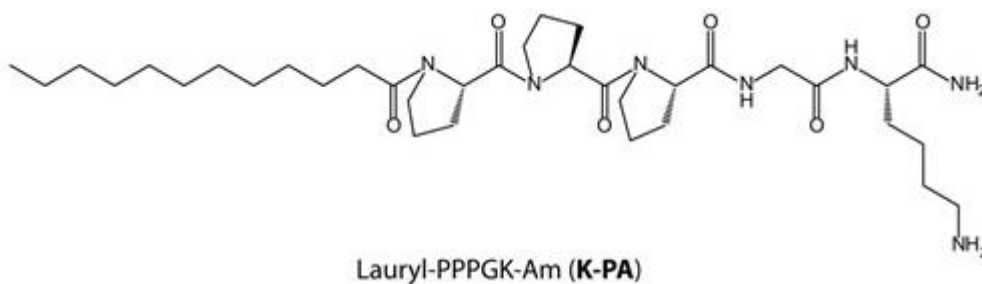
improve the biocompatibility and biodegradability of the functionalized SPIONs. In the PA design, three main segments were used for the development of stable, well-dispersed SPION/PA system. While alkyl tail of PA enhances the hydrophobic interactions between alkylated surface of SPIONs and PA, the proline-rich segment (-PPP) with its hydrogen bond breaking property improves intermolecular cohesive interactions by avoiding nanofiber formation. Finally, charged amino acid residue is used to solubilize the system as well as to prevent its aggregation. The PAs were synthesized by solid phase peptide synthesis strategy (Figure 2.1b,c). SPIONs were successively transferred into the aqueous environment with the non-covalent interaction based coating procedure.

The hydrodynamic size of SPION/PAs was determined in two different media, water and 5% dextrose solution, hydrophobic nanoparticles with a core size of 5.3 nm were found to have hydrodynamic sizes of  $58.0 \text{ nm} \pm 0.7$  and  $58.6 \text{ nm} \pm 0.1$ , which are in the range of optimal values for long circulation times *in vivo*<sup>141</sup> (Figure 2.2). The hydrodynamic sizes did not significantly change over the measured period of time for both solutions, and they maintained their dispersion stabilities even after a week. Nanoparticles dispersed in 5% dextrose solution exhibited smaller changes in their hydrodynamic sizes compared to those dispersed in water, which is suitable for the storage of these nanoparticles prior to their administration. Their zeta potentials were also measured and found to be positively charged due to the lysine residue present in the PA structure. Zeta potential values of SPION/K-PA were  $18.3 \pm 1.4 \text{ mV}$  in water and  $23.7 \pm 1.7 \text{ mV}$  in 5% dextrose solution. SPION-LPPR nanoparticles exhibited zeta potentials of  $24.8 \pm 1.7 \text{ mV}$  and  $33.2 \pm 1.1 \text{ mV}$  in water and 5% dextrose solution, respectively.

A)



B)



C)

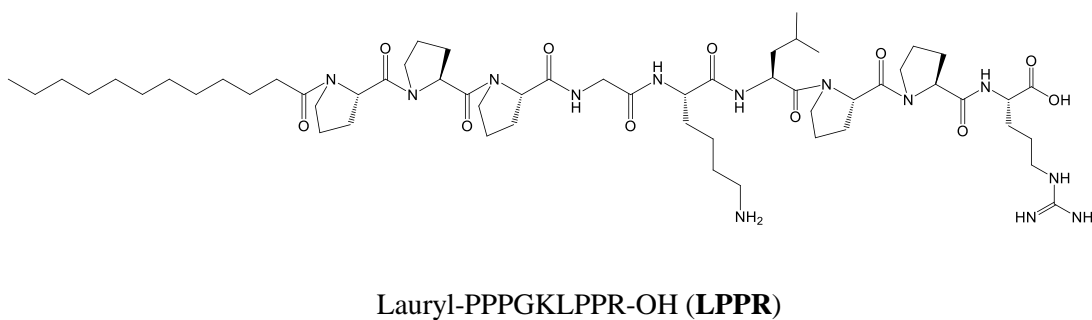


**Figure 2.1** a) Images of hydrophobic iron oxide nanoparticles in the absence and presence of magnetic field when they are dispersed in hexane (10 mg/mL, concentration based on the iron content) b) Chemical structures of PA molecules, K-PA, and c) LPPR.

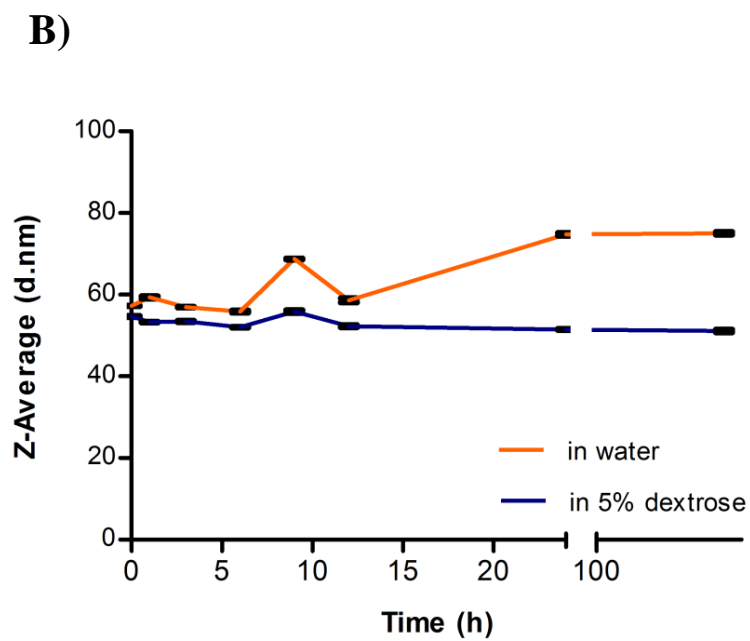
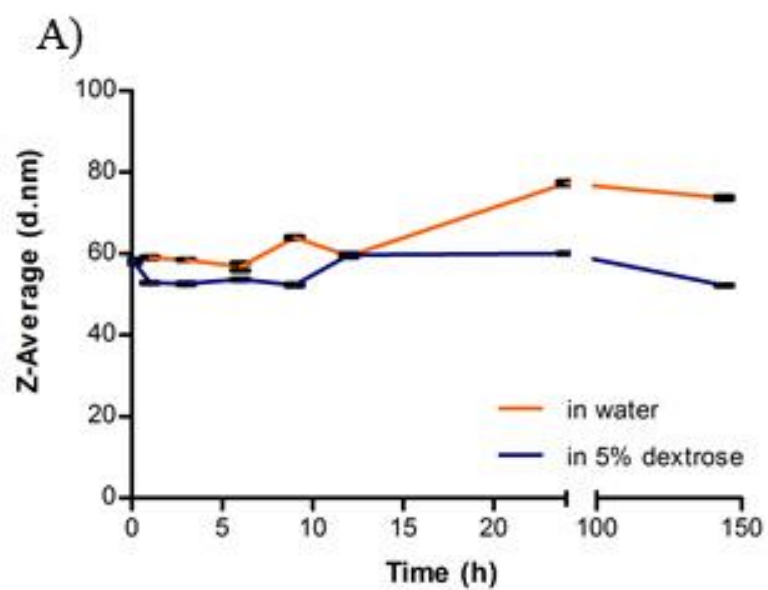


**Figure 2.2** DLS analysis to determine the dispersion stability of K-PA coated SPIONs (A) and LPPR coated SPIONs (B) prepared in two different media as a function of time.

### 2.2.2 *In vitro* Cytotoxicity and Uptake Studies

The biocompatibility of PA coated SPIONs and free PAs was evaluated on vascular endothelial cells and human breast cancer cells by using Alamar blue assay. Iron concentrations were adjusted by measuring iron contents of the solutions using colorimetric Prussian blue assay. PA amounts in corresponding SPION/PA solutions were spectroscopically determined. We compared the toxicity profiles of PA and PA coated SPIONs to understand whether they affect the viability of tumor cells expressing high levels of NRP-1 (MCF-7) and negative for NRP-1 (MDA-MB-453) or non-tumor cells (Figure 2.3). No significant toxicity was observed on HUVECs and MCF-7 cells for PA coated SPION and free LPPR exposure up to 200  $\mu\text{g/mL}$  at 24 h and 48 h. In the literature, dextran or citric acid coated nanoparticles were shown to demonstrate higher cytotoxicity on HUVECs at nanomolar concentrations after 24 h of exposure<sup>142</sup>. When compared to those nanoparticles, these SPIONs are safer for biomedical applications. On the other hand, cytotoxicity assay results also showed that K-PA effects cell viabilities in a dose-dependent manner, especially on tumor cells which may result from the presence of positively-charged side chains on the surfaces of unbound PAs that may increase their interactions with the cell membrane, resulting in membrane damage<sup>143</sup>. Interestingly, PA coated SPIONs showed high cytotoxicity on non-metastatic, semi-adherent MDA-MB-453 cells, even at low concentrations. Bachelder *et al.* reported that in hypoxic environment, metastatic cells increase their survival rate by increasing expression level of VEGF and its receptor, NRP-1. On the contrary, non-metastatic cells do not have NRP-1 and thus, they are more prone to apoptosis<sup>144</sup>. The observed differences in viabilities of two breast cancer cells may be derived from that mechanism.

Prior to *in vivo* studies, the biocompatibility of the nanoparticles was further analyzed using live-dead assay. For *in vitro* studies, selected concentration (75 µg/mL) is equivalent of MR administration dosage which was calculated according to the total circulating blood volume of a rat (64 mL/kg of body weight)<sup>145</sup>. The data in Figure 2.4 indicate that there was no considerable reduction in vascular cell viability after exposure to free PA and PA coated SPION compared to the no-treatment group. More than 90% of the cells were able to survive in the presence of PA coated SPIONs after 24 h incubation, suggesting that these nanoparticles could be employed safely in MRI.

Endothelial cells were stained with Prussian blue to visualize the cellular uptake of nanoparticles. Clustered blue particles were present on the surfaces and interiors of HUVECs exposed to SPION-K or SPION-LPPR (Figure 2.5). Nanoparticles were retained in cells within 6 h. The binding efficiency of PA coated SPIONs reached approximately 90% for HUVECs. Under the same conditions, no blue dots were observed in non-treated control cells. The strong binding interaction exhibited by PA coated SPIONs may result from the electrostatic interactions between negatively charged phospholipid membrane of the cells and the positively charged nanoparticles. In addition, it is known that positively charged nanoparticles have higher uptake rates than negatively charged particles<sup>146</sup>.

In order to test specific targeting capability of LPPR coated SPIONs and thus inhibitory effect of angiogenesis, Matrigel tube formation assay was used *in vitro* (Figure 2.6). Capillary-like structure formation was demonstrated in the presence and absence of PA coated SPIONs. At 6 h after seeding, HUVECs interconnected via cellular extensions in control and SPION-K treated groups, whereas tubes were

disrupted as soon as SPION-LPPR treatment was applied. A similar pattern was observed at 24 h. The effect of SPIONs on tube formation was clearly indicated with quantification. It can be seen that there is a significant difference between SPION-LPPR treated cells and non-treated control group. According to tube formation assay, LPPR coated SPIONs can selectively bind to the components of angiogenesis and prevent tube formation.

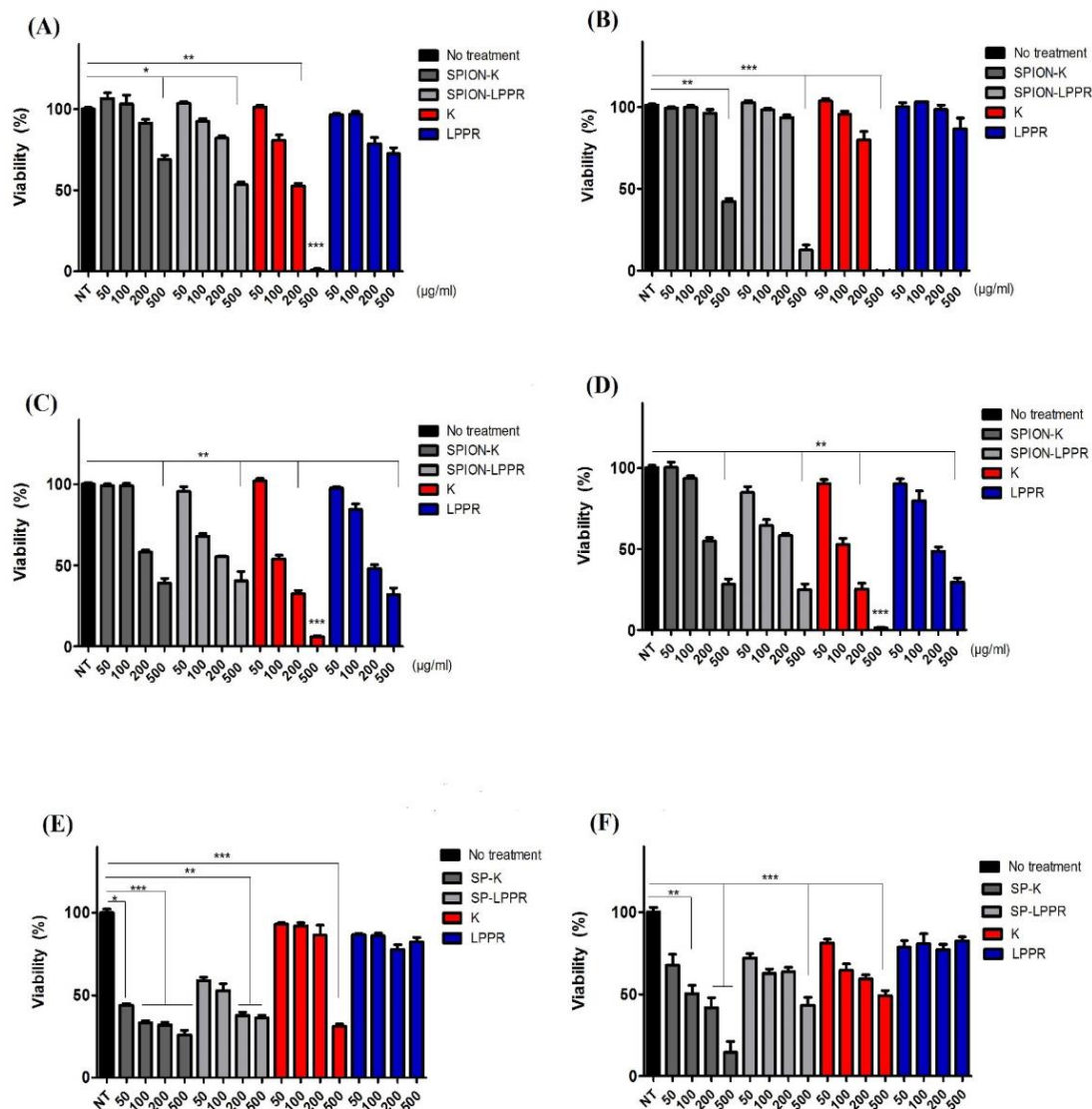


**Figure 2.3** Dose-dependent cytotoxicity profiles of PA coated SPIONs and free PAs on different cell lines. Cell viability of HUVEC (a, b), MCF-7 cells (c, d) and MDA-MB-453 cells (e, f) treated with free PAs (50-500  $\mu\text{g/mL}$  which is equivalent content of iron assembled with PA) and PA coated SPIONs (50-500  $\mu\text{g/mL}$ ) at 24 h (left column) or 48 h (right column). Values were compared to those of the untreated controls and are presented as percentages. Data represent means  $\pm$  standard error of mean (SEM) of a minimum of 3 independent experiments performed in quadruplicates

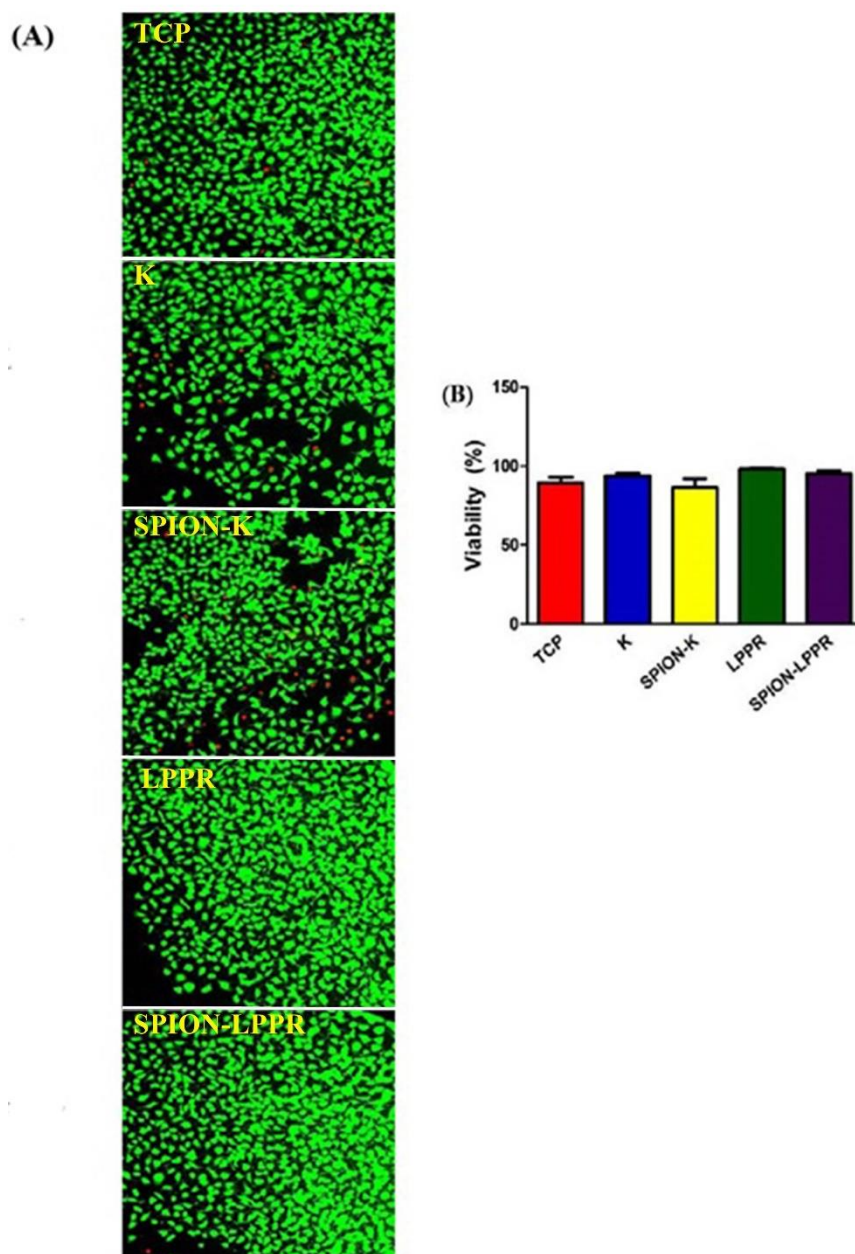


**Figure 2.4** Viability of HUVECs. (A) Cells were tested for cell death after treatment with free K-PA or LPPR-PA (855  $\mu\text{g}/\text{mL}$ ) and PA coated SPIONs (75  $\mu\text{g}/\text{mL}$ ) for 24 h by live-dead assay. Live cells were stained with Calcein-Am (green) and dead cells were stained with ethidium homodimer-1 (red), magnification: 10X. (B) Quantification of viability of experimental groups. TCP: tissue culture plate.

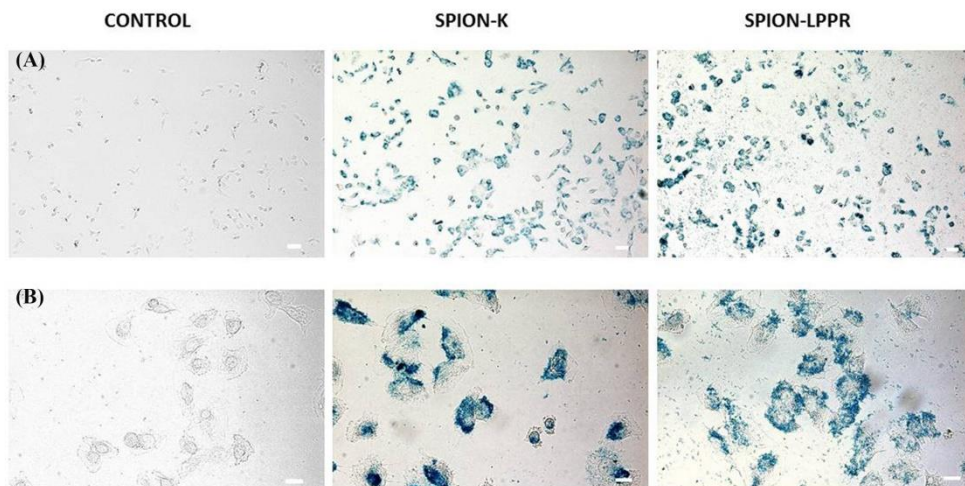


**Figure 2.5** Prussian blue assay of HUVECs. (A) Light microscopy of HUVECs following 6 h of incubation with and w/o SPION-K or SPION-LPPR. (B) Lower panel is higher magnification of samples (40X). Experiments were performed two independent times in triplicate. Scale bars are 50  $\mu\text{m}$  and 20  $\mu\text{m}$  for upper and lower panels, respectively.

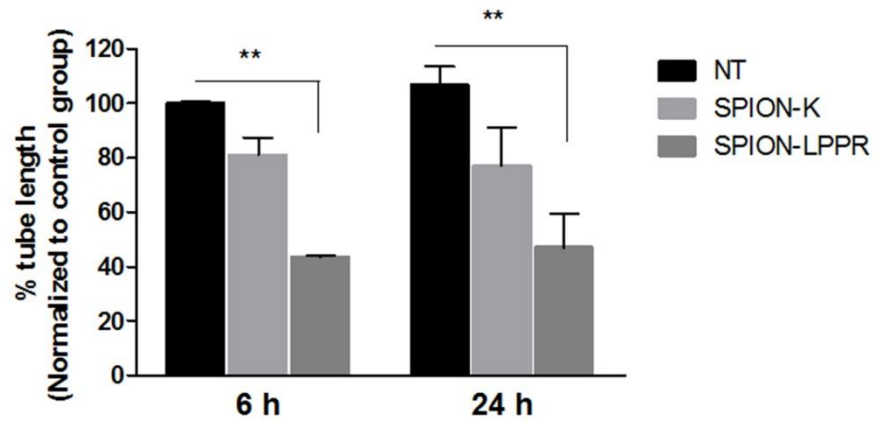
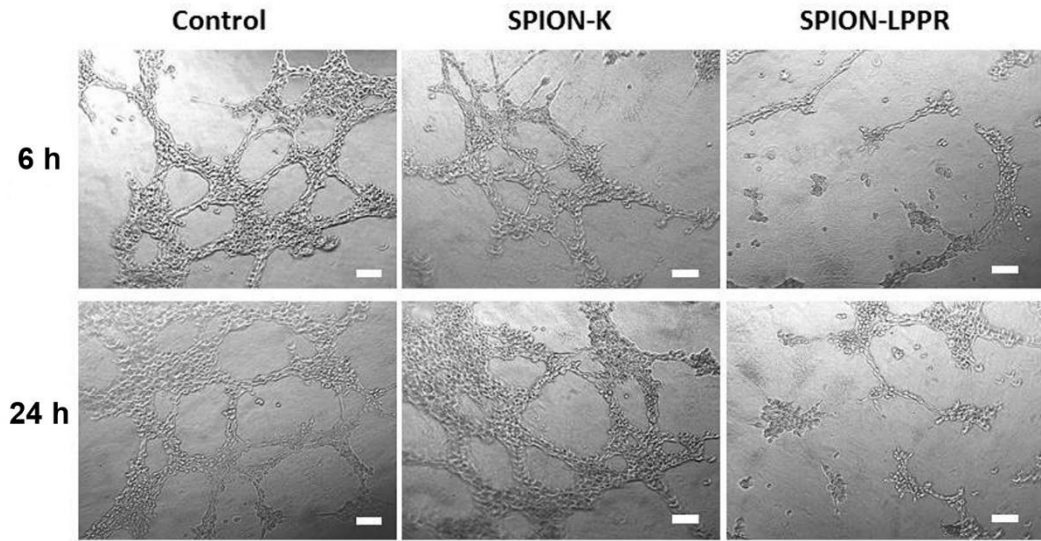


**Figure 2.6** Tube formation on Matrigel. LPPR coated SPIONs exhibit rapid anti-angiogenic effect. Network formation was examined after seeding HUVECs in Matrigel-coated plates during 6 h and 24 h period. Scale bar: 100  $\mu$ M. The error bars represent SEM, (n = 3), ( $p \leq 0.001$ ).

### **2.2.3 *In vivo* Cancer Model**

7,12-Dimethylbenz(a) anthracene (DMBA) is a well known carcinogen which leads to the release of lipid peroxides and formation of free radicals to induce tumorigenesis<sup>147</sup>. In order to optimize DMBA concentration for cancer model, we firstly performed preliminary experiments. The animals were distributed into three groups depending on their weight each containing 2 animals. Rats were exposed to 3 different concentrations of DMBA (20, 50, 80 mg/kg body weight). Palpable mammary tumors were observed in DMBA treated animals after 12 weeks (Figure 2.7b). Tumors in 20 mg/kg body weight of DMBA group were very small for MRI experiments. On the other hand, 80 mg/kg body weight of DMBA injection results in lots of tumors with different size and shape. Therefore, 50 mg/kg DMBA was selected for further study to produce animal breast tumor. Animals can survive for several weeks with solid breast tumor. These solid tumors have hypoxic and necrotic core and highly vascularized rim (Figure 2.7c) which demonstrates the high growth rate and aggressiveness of the cancer<sup>148</sup>.

One of the limitations of this chemically induced breast cancer model is that the treated rats eat their tumors when tumor volume reaches 100 mm<sup>3</sup> or more. Therefore, we waited the regrowth of breast tumor prior to MRI imaging of some groups, and the larger tumors shown in Figure 2.15 consequently represent late-stage tumors that exhibited rapid growth during the 15 days observation period.

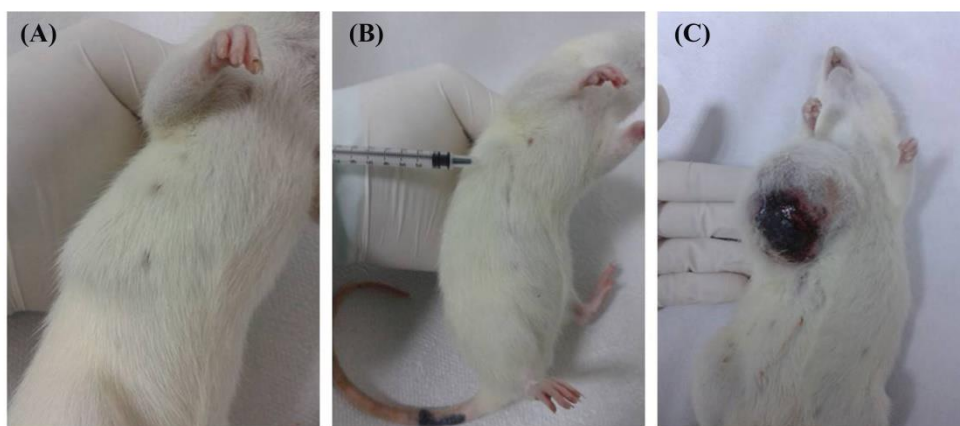


**Figure 2.7** Chemically induced breast cancer progression in female Sprague-Dawley rats. Photograph of a rat before injection (A), palpable tumor formation at injection site (B), and last stages of cancer characterized with necrotic tissue (C).

#### **2.2.4 *In vivo* Magnetic Resonance Imaging (MRI) Studies**

We evaluated the capacity of the PA coated SPIONs to serve as a negative contrast agent in T2-weighted MRI *in vivo*. Relative signal intensity (SI) of nanoparticles in tumors, healthy breast tissue and RES organs were determined as a function of time for up to 15 days after contrast agent injection through the tail vein, using a clinical 1.5 T MRI system with a T2-weighted m-GRASE sequence. The binding specificity of SPIONs to the mammary tumors was determined in a chemically induced rat model of breast cancer. Unfortunately, specific targeting of anti-angiogenic peptide (LPPR) coated SPIONs to highly vascularized breast tumor was not characterized. Although toxicity results derived from *in vitro* data demonstrated the biocompatibility of LPPR coated SPIONs, it did not fully reflect the *in vivo* outcomes<sup>149</sup>. The tail vein injection of LPPR coated SPIONs showed toxicity *in vivo* at highest and lowest concentrations even in different solvents. For this reason, we continued our study with SPION/K-PA. MRI results showed that the nanoparticles preferentially accumulated in tumor tissue rather than RES organs. Compared to the T2-weighted images prior to the administration of SPION/K-PA and non-injected control groups, significant negative enhancement of the MRI signal for SPION/K-PA in the tumor tissue was observed from 1 h to 4 h (Figure 2.8, 2.9 and 2.10). In order to quantify signal contrast enhancement, signal intensity changes resulting from nanoparticle uptake into tumor and other organs were calculated in the RIO of the T2-weighted m-GRASE images as a function of time (Figure 2.11). Importantly, signal intensities of mammary tumors decreased by approximately 45% and 65% at 1 h and 4 h after SPION/K-PA injection, respectively. These results confirmed that SPION/K-PA could serve as an effective negative contrast agent for the diagnosis of cancer by MRI. Additionally, there was no

statistically considerable difference between the organs of healthy and tumor-bearing animals in terms of the signal drop in breast and RES organs following the administration of nanoparticles. Relative SIs were observed to be reduced in the liver, kidney and spleen of both healthy and tumor-bearing animals immediately following nanoparticle administration, which may be a consequence of the fast blood flow rate in these organs<sup>150</sup>. Nevertheless, the signal intensity of magnetic nanoparticles in RES organs started to increase to the same levels as the pre-injection groups at 1 h (Figure 2.11). Compared to the T2 values measured using pre-contrast images, the particles did not produce a T2 shortening after 15 days in any organ. This indicated that nanoparticles were removed from the organs within two weeks.

Though SPION/PA does not possess any targeting ligands on its surface, it can efficiently accumulate in tumors because of the leaky vascular structure of tumor tissue (EPR effect). Using this phenomenon, SPIONs have been previously utilized for *in vivo* cancer imaging via MRI in the absence of a biologically active targeting ligand<sup>151</sup>. However, there is a distinct lack of information regarding the elimination routes and times of retention associated with SPIONs in different organs.

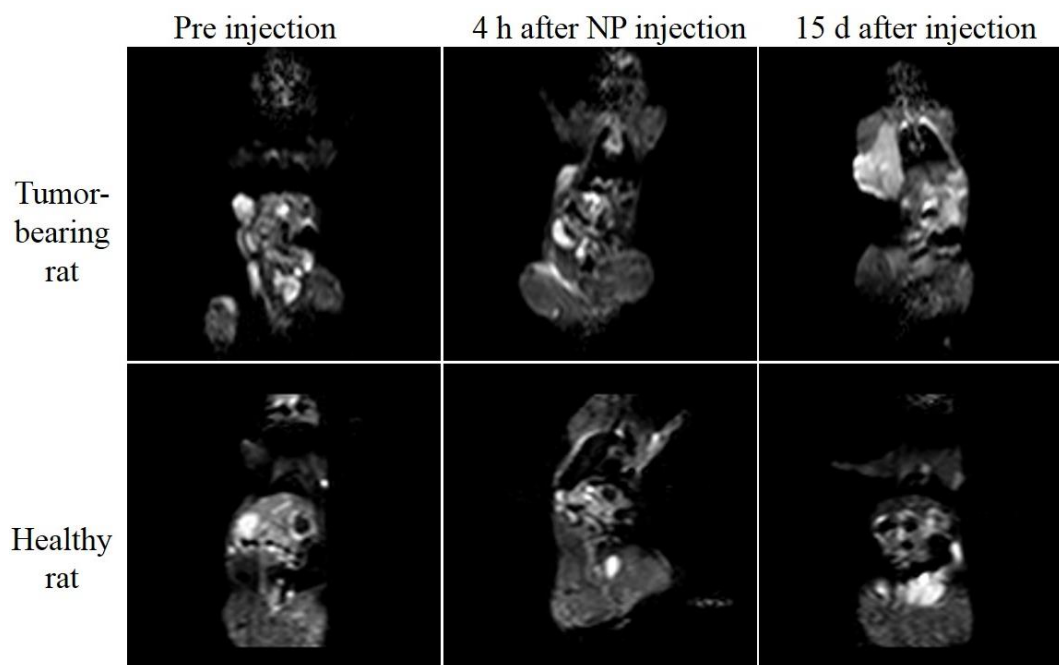


**Figure 2.8** *In vivo* MRI. Signal intensity changes in T2 relaxations at pre injection, 4 h and 15 d post administration of SPION/K-PA (5 mg/kg) in breast, liver, spleen, kidney and breast tumor of rats. A clear gradual signal intensity drop in the breast tumor was observed after SPION/K-PA administration.

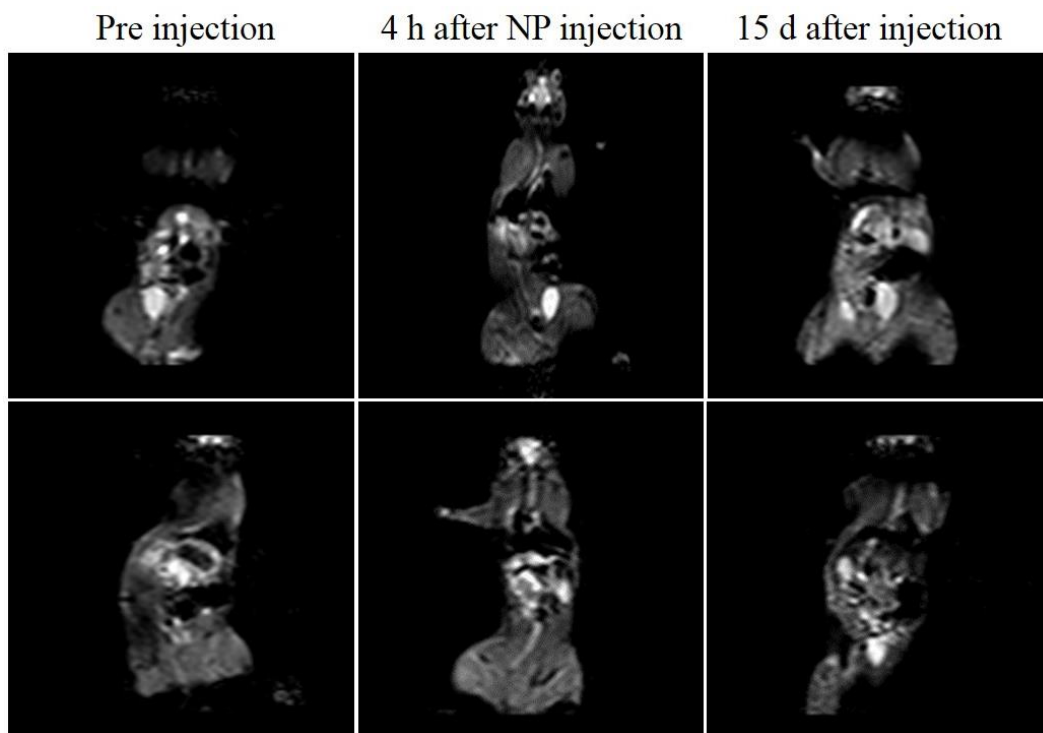


**Figure 2.9** MR images from healthy rats.

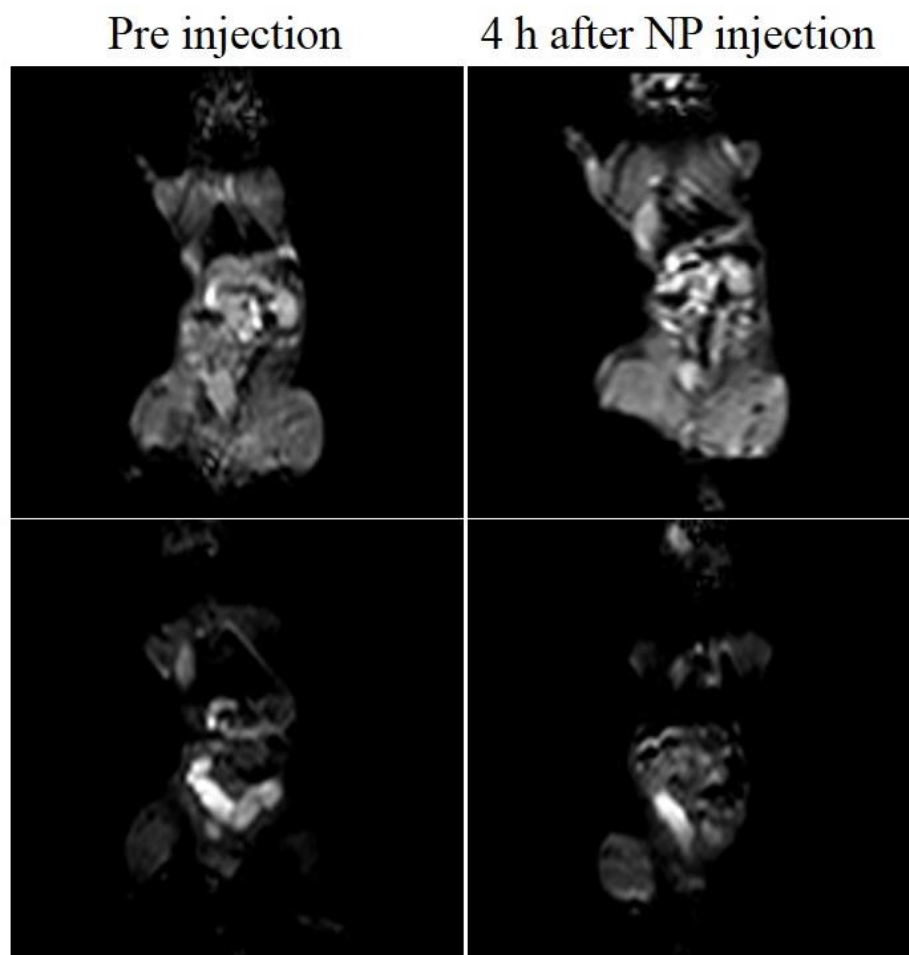


**Figure 2.10** *In vivo* MR images from tumor bearing rats.

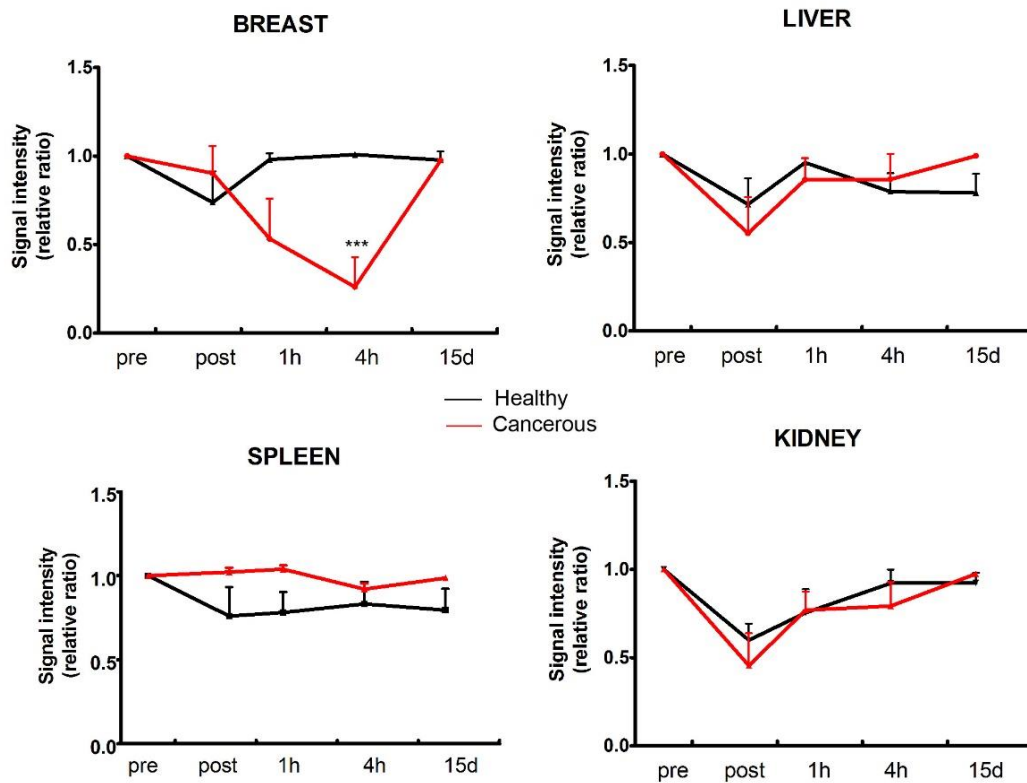


**Figure 2.11** Quantification of signal intensity changes in T2 relaxations at pre-, immediately after injection, 1 h, 4 h and 15 d post administration of SPION-K (5 mg/kg) in breast, liver, spleen and kidney tissues of rats.

### **2.2.5 Histological Examination and Tissue Distribution of SPION/K-PA**

We examined the short and long-term distribution of SPION/K-PA within the tissue sections of rats after nanoparticle injection. RES organs are the main site of accumulation for nanoparticles. Nanoparticle aggregation at these locales may cause inflammation, release of toxic byproducts by biodegradation or uncontrolled and unpredictable patterns of localization. In addition, prolonged nanoparticle exposure may result in hematopoietic, bone marrow and/or renal toxicity<sup>152</sup>. In particular, the infiltration of monocytes and lymphocytes through the portal space or centrolobular veins is the most important indicator of the inflammatory process in liver<sup>153</sup>. There were no obvious pathological changes or any lesions in the liver and the number of lymphocyte did not alter in the spleen of both healthy and tumor-bearing rats after nanoparticle injection (Figure 2.12 and 2.13). Additionally, shortened tube cavity, atrophy of the renal tubular and glomerular epithelial cells, and transparent tubes were lacking in the kidney of experimental groups as well. We therefore demonstrated that exposure to SPION/K-PA does not result in inflammation or systemic toxicity not only in short term but also at two weeks post-injection.

To further verify the accumulation and distribution of SPION/K-PA in tumors and harvested organs, Prussian blue staining was carried out as shown in Figure 2.14, 2.15 and 2.16. In the tumors of rats administered with SPION/K-PA, we could detect a large number of blue dots, which indicates the elevated uptake of nanoparticles. Prussian blue staining of liver, spleen and kidney tissues in the SPION/K-PA group revealed no significant uptake of nanoparticles in both healthy and cancerous rats after 4 h. These results are in accordance with those obtained by MRI.

When designing an effective nanomaterial for diagnostic applications, one of the most important issues is to increase the material's residence time in the organ of interest and thereby allow imaging to be performed for as long as possible prior to its clearance. However, the material should also be broken down and removed from the body after imaging to prevent its cumulative accumulation<sup>154</sup>. Taken together, our results demonstrated that SPION/K-PA is biocompatible and biodegradable and may be incorporated within the iron stores of body, while localizing into the tumor site and allowing enhanced MRI imaging following injection<sup>155</sup>.

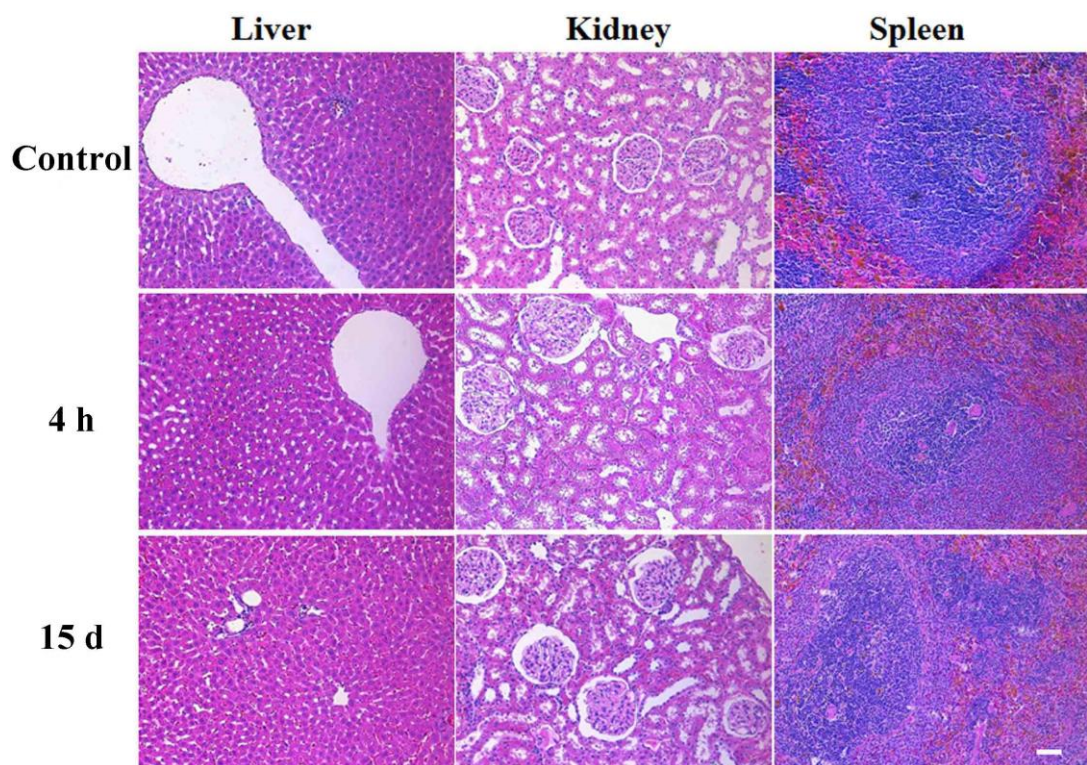


**Figure 2.12** H&E staining for analyzing the tissue morphology of the kidney, liver and spleen of healthy rats (control) or 4 h and 15 days following the injection of SPION/K-PA (5 mg/kg) (original magnification x200 and scale bar:50  $\mu$ m).

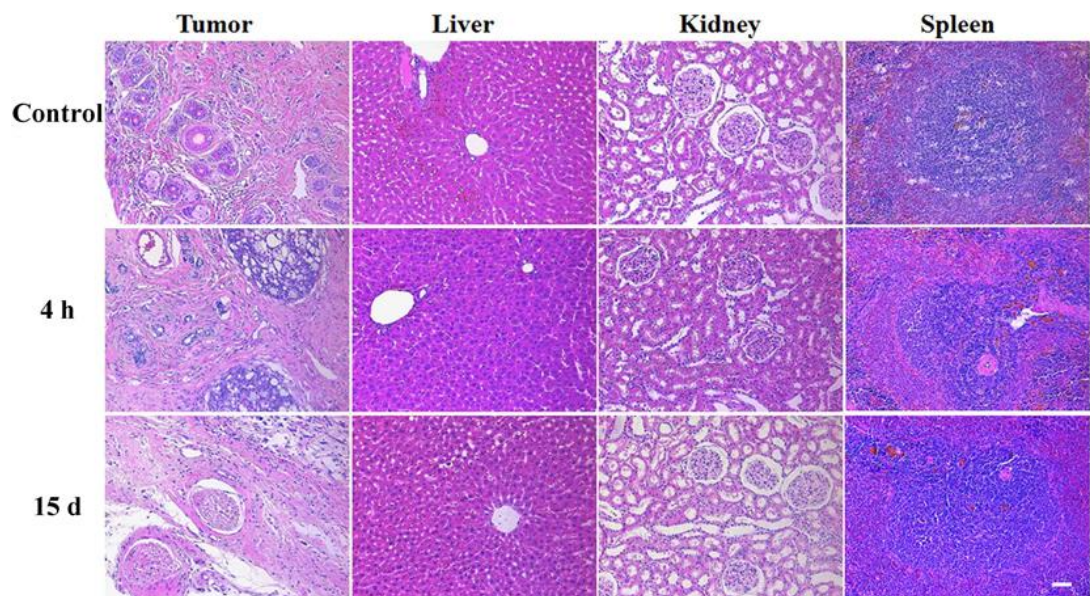


**Figure 2.13** H&E staining for analyzing the tissue morphology of the kidney, liver and spleen of tumor bearing rats (control) or 4 h and 15 days following the injection of SPION/K-PA (5 mg/kg). Photographs were taken at x200 magnification. Scale bar: 50  $\mu$ m.

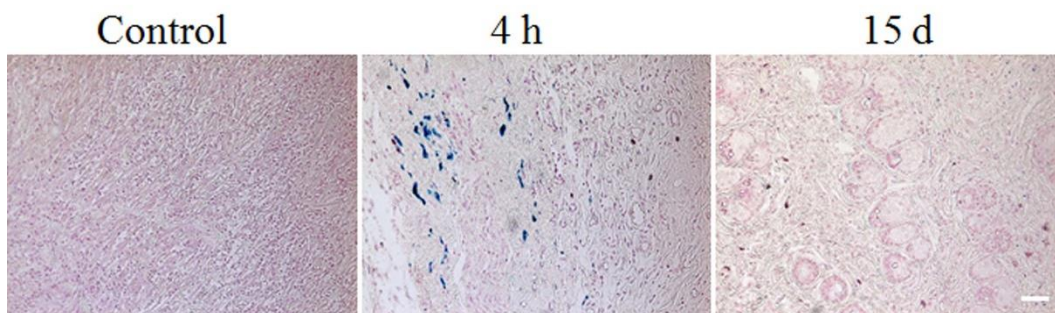


**Figure 2.14** Prussian blue staining for investigating iron accumulation in the tumor of rats (control) or 4 h and 15 days following the injection of SPION/K-PA (5 mg/kg) (original magnification, x200, scale bar: 50  $\mu$ m).

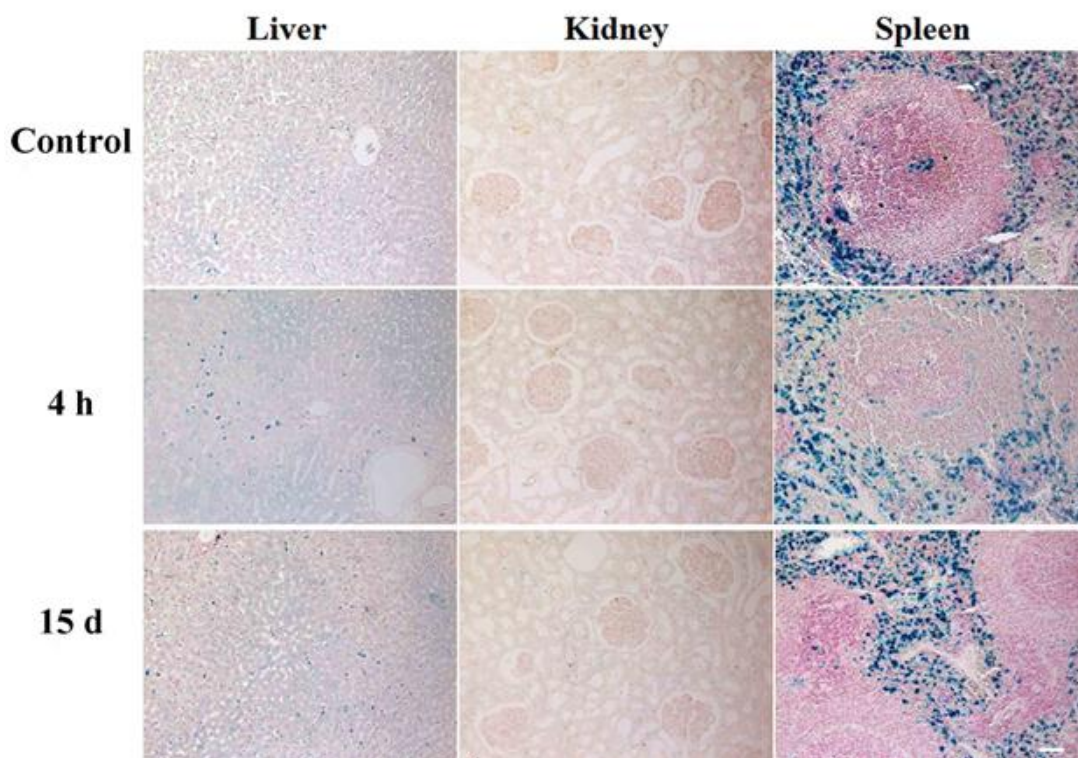


**Figure 2.15** Representative photomicrographs of the liver, kidney and spleen of healthy rats (control) or 4 h and 15 days following the injection of SPION/K-PA (5 mg/kg) stained with Prussian blue staining for analyzing iron accumulation. Positive staining appears in blue dots. (Original magnification  $\times$ 200. Scale bar: 50  $\mu$ m).

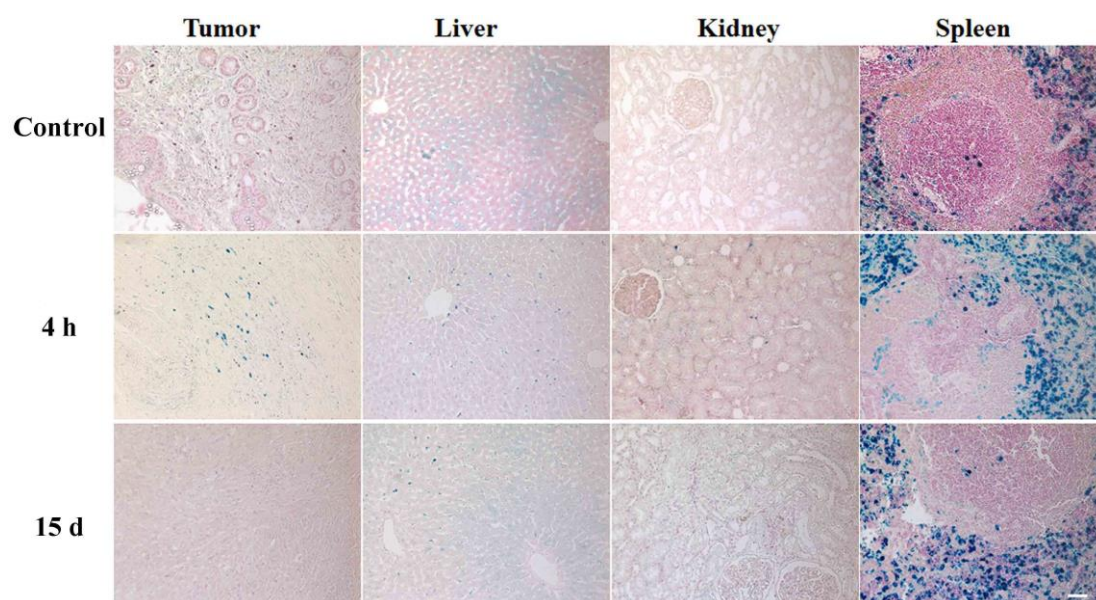


**Figure 2.16** Prussian blue staining for investigating iron accumulation in the tumor, kidney, liver and spleen of tumor bearing rats (control) or 4 h and 15 days following the injection of SPION/K-PA (5 mg/kg) (original magnification x200, scale bar is 50  $\mu$ m).

### 2.3 CONCLUSION

In summary, these results showed that proline-rich PA molecules are suitable for transferring hydrophobic iron oxide nanoparticles into aqueous environments through noncovalent interactions. The MRI signal of breast tumor tissue significantly enhanced after the administration of SPION/K-PA, suggesting that the nanocomposite system is promising as a MRI negative contrast agent. Studies regarding the *in vivo* fate of SPION/K-PA suggest that the co-assembled system is biocompatible and biodegradable, as confirmed by the long-term consistency of the MRI signal and the material's lack of accumulation in RES organs in histological analyses. Due to the ease of functionalization of nanoparticles, the practical utility of PA functionalized SPIONs can be further extended by appending bioactive epitopes into the PA construct to selectively target a specific type of receptor or cell.

## 2.4 EXPERIMENTAL SECTION

### 2.4.1 Materials

1-Dodecylamine (98%) and iron(III) 2,4-pentanedionate (97%) ( $\text{Fe}(\text{acac})_3$ ) were purchased from Alfa Aesar. 1,2-Hexadecanediol was purchased from Sigma-Aldrich. Lauric acid and trifluoroacetic acid (TFA) were purchased from Merck. Chemicals required for peptide synthesis, such as 9-fluorenylmethoxycarbonyl (Fmoc), tert-butylloxycarbonyl (Boc) protected amino acids, [4- $[\alpha$ -(2',4'-dimethoxyphenyl)Fmoc-aminomethyl]phenoxy]acetamidonorleucyl-MBHA resin (Rink amide MBHA resin) and 2-(1H-Benzotriazol-1-yl)-1,1,3,3-tetramethyluronium hexafluorophosphate (HBTU) were purchased from NovaBiochem. All reagents and solvents were used as received. Water used during the experiments was deionized by a Millipore Milli-Q purifier system and had a resistance of 18 M $\Omega$ .cm.

### 2.4.2 Synthesis of superparamagnetic iron oxide particles

Superparamagnetic nanoparticles were synthesized by Melis Şardan Ekiz according to a previously described procedure with minor modifications<sup>76</sup>. Briefly, 6 mmol (1.112 g) lauric acid, 6 mmol (1.2 g) laurylamine and 10 mmol (2.584 g) 1,2-hexadecanediol were mixed in 20 mL of dibenzylether and heated. When the reaction medium reached 200 °C, 2 mmol (0.706 g)  $\text{Fe}(\text{acac})_3$  was added and the sample was stirred for 1-1.5 h at 200 °C under inert atmosphere. A condenser was added to the setup for reflux and the system was moved to a hot jacket heater to increase the temperature to 300 °C. Following 1 h of stirring at this temperature, the mixture was allowed to cool to room temperature and 50 mL ethanol was added under air. The mixture was centrifuged at 8000 rpm for 15 min, the supernatant was removed and 2-3 ml of hexane was added

to the pellet. After 1 min of sonication, 20-30 mL of ethanol was added to the mixture. Lastly, the sample was centrifuged again and the brownish supernatant was discarded. Ethanol addition, centrifugation and decantation steps were repeated until the supernatant was observed to exhibit a clean color. The colorless supernatant was then discarded and 6-7 mL of hexane was added to the pellet. SPIONs were obtained by sonication for 5 min followed by centrifugation for 10 min at 6000 rpm, and stored at 4 °C until use.

### **2.4.3 Peptide amphiphile (PA) synthesis**

Peptide synthesis was performed by using solid phase peptide synthesis by Melis Şardan Ekiz. MBHA Rink Amide resin was used as the solid support for the synthesis of the Lauryl-PPPGK-Am and Lauryl-PPPGKLPPR-OH PAs, and used at a loading of 0.59 mmol/g. Amino acid couplings were carried out in piperidine/dimethylformamide (DMF) in the presence of 2 equivalents of Fmoc protected amino acid, 1.95 equivalents of HBTU and 3 equivalents of N,N-diisopropylethylamine (DIEA) for 2 h. Base-labile Fmoc protecting groups were removed by treatment with 20% DMF solution for 20 min. Acid-labile groups were cleaved and the peptide was removed from the resin using a cleavage cocktail solution (trifluoroacetic acid (TFA) : triisopropylsilane (TIS) : H<sub>2</sub>O in the ratio of 95:2.5:2.5), which was added to the beads and left to react for 2 h at room temperature. Excess TFA was then removed by rotary evaporation, the remaining viscous peptide solution was treated with ice-cold diethyl ether, and the resulting white pellet was freeze-dried. The chemical composition of the PAs was elucidated by reverse phase high-performance liquid chromatography (HPLC) using an Agilent 6530 accurate-Mass Q-

TOF LC/MS equipped with an Agilent 1200 HPLC. A Phenomenex Luna 3 $\mu$  C8 100A (50 x 3.00 mm) column and a water (0.1% formic acid)/acetonitrile (0.1% formic acid) gradient were used as stationary phase and mobile phase, respectively. The PAs were purified on an Agilent 1200 HPLC having Agilent Zorbax 300SB-C8 (21.2 x 150 mm) column with a water (0.1% TFA)/acetonitrile (0.1% TFA) gradient.

#### **2.4.4 Surface coating of SPIONs**

50 mg of PAs were dissolved in deionized water (20 mL), heated up to 55-65 °C and ultrasonicated. 7 mg of SPIONs in hexane (2 mL) was then added to the peptide solution during the sonication process. PA molecules and SPIONs were mixed at a weight ratio of 7:1 and a volume ratio of 10:1, respectively. After an hour of repeated sonication and vortexing steps at indicated temperature range, the solution was purified by centrifugation at 6500 rpm for 5 min, using ultrafiltration tubes with 50 kDa cut-off membranes (Millipore Amicon Ultra-Regenerated Cellulose). This step was repeated at least 2 times.

#### **2.4.5 Morphological characterization of SPIO nanoparticles**

TEM was performed using a FEI Tecnai G2 F30. 10  $\mu$ L of 50-fold diluted, SPION samples were placed on a carbon film (300 mesh) coated copper grid and incubated for 5 min. The excess solution was then removed by pipetting, and the grids were dried under fume hood at room temperature for over 2 h. Nanoparticle diameters were determined by using Image J software from at least 100 nanoparticles.

#### **2.4.6 Particle size and zeta potential analysis**

Hydrodynamic sizes and zeta potentials of the particles were measured by DLS. A Malvern Nanosizer/Zetasizer nano-ZS ZEN 3600 (Malvern Instruments, USA)

instrument with a detector angle of  $173^\circ$  was used for DLS analysis. Hydrophobic particles and hydrophilic particles were diluted with hexane and water, respectively, and measurements were performed in quartz cuvettes. In addition, dip cell electrodes were used in Zeta measurements. All measurements were done in triplicate and standard deviations were calculated from the mean of data. For experiments conducted in 5% dextrose solution at  $25^\circ\text{C}$ . Refractive index, viscosity and dielectric constant values were assumed to be 1.34, 1.03 Pa.s and 77.37, respectively. The concentration of iron oxide nanoparticles was set to  $250\ \mu\text{g}/\text{mL}$  for all experiments, and the refractive index of magnetite particles was taken as 2.42.

#### **2.4.7 Iron content determination**

Iron concentration was determined through colorimetric Prussian blue assay prior to PA coating and *in vitro* and bioimaging experiments. In the Prussian Blue assay, a calibration curve was plotted by preparing serially diluted iron solutions (1000 ppm, VWR-BDH Prolabo) in 6 N HCl. All samples including standards and unknowns were digested at  $65^\circ\text{C}$  for an hour for the conversion of iron from nanoparticle form to ionic form.  $160\ \mu\text{L}$  HCl and  $40\ \mu\text{L}$  of 5%  $\text{K}_4\text{Fe}[\text{CN}]_6$  was then added to  $160\ \mu\text{L}$  of samples. Three independent repeats of each sample were prepared for measurement, and HCl and 5%  $\text{K}_4\text{Fe}[\text{CN}]_6$  in water was used as blank solution. Samples were allowed to stain for 20-25 min, and solution color was observed to change from yellow to blue in high-concentration samples following the reaction. UV absorbance was measured at 690 nm by using Spectramax M5 (Molecular Devices).

#### **2.4.8 PA content determination**

PA-coated SPIONs were purified from excess PA molecules by ultrafiltration using Millipore Microcon Centrifugal Filter Units at a cut-off point of 50 K MW. SPIONs were filtered 2 to 3 times at 6500 rpm for 5 min. The eluted parts were collected at each step and PA concentrations were measured by NanoDrop 2000 (Thermo Scientific). Results were compared with the results obtained from samples prepared with known amounts of PAs. Peptide quantification method offered by Thermo Scientific was utilized to measure the absorbance at analysis wavelength of 205 nm with an extinction coefficient of 31 mg/mL at 1 cm path length<sup>156</sup>. PA solutions were prepared at different concentrations in the range of 0.5 mg/mL to 0 mg/mL by serial dilution.

#### **2.4.9 *In vitro* studies**

Viability profiles of human vascular endothelial cells (HUVEC) estrogen receptor (ER) positive human breast adenocarcinoma (MCF-7) cells and triple negative human breast carcinoma cells (MDA-MB-453) were characterized in the presence of PAs and SPIONs. HUVECs and MDA-MB-453 were kindly donated by Yeditepe University, and Bilkent University, respectively. MCF-7 cells were obtained from the American Type Culture Collection (ATCC, Manassas, VA, USA).

Cells were cultured in Dulbecco's Modified Eagle's Medium (DMEM) (Sigma Chemicals, St. Louis, USA) supplemented with 10% fetal bovine serum (FBS) (Gibco, Carlsbad, CA, USA) and 1% penicillin/streptomycin. Culturing was performed in standard humidified incubators with constant 5% CO<sub>2</sub> at 37 °C. Cells were harvested with trypsin-EDTA after reaching 80% confluency.

#### **2.4.9.1 Cell viability analyses**

Alamar blue assay was used to evaluate the biocompatibility of free PA and PA coated SPIONs on cells. Harvested cells were seeded into 96-well plates (Costars, Corning Inc., NY, USA) with their respective standard culture media at densities of  $1 \times 10^4$  cells/well HUVEC or MCF-7, and  $3 \times 10^4$  cells/well MDA-MB-453. Sterilized and sonicated free PA and SPIONs were diluted 1:4 in culture medium prior to use. The final concentration ranges for the PA and nanoparticles were 0-2.125  $\mu\text{M}$  (equivalent content of iron assembled with PA is indicated in the figure) and 0-500  $\mu\text{g/mL}$ , respectively. After 21 or 45 h of incubation, 100  $\mu\text{L}$  of Alamar blue solution (10% in serum free culture medium) was added to each well after discarding old medium. Following 3 h of incubation, fluorescence readings of the wells were recorded by an M5 Microplate Reader (Molecular Devices, USA) with excitation at 530 nm and emission at 590 nm. Biocompatibility of the samples on vascular cells was also evaluated by live-dead assay (Invitrogen) according to the manufacturer's instructions. HUVECs were seeded into 96-well plates with their standard culture medium at a density of  $5 \times 10^3$  cell/well and treated with SPION/PA (75  $\mu\text{g/mL}$ , according to Fe concentration) and PA (214  $\mu\text{g/mL}$ , 317  $\mu\text{M}$ ) for 24 h (n=3). HUVECs were then washed with sterile phosphate buffered saline (PBS) and stained with 1  $\mu\text{M}$  calcein-AM and 2  $\mu\text{M}$  ethidium homodimer-1. Five images were taken under fluorescence microscopy and quantified using Image J for each sample.

#### **2.4.9.2 SPION accumulation analyses in cells**

SPION accumulation was visualized by staining the cells with Prussian blue, which imparts a blue-purple color in the presence of iron. HUVECs were used for Prussian

blue staining. Cells were seeded at a density of  $1 \times 10^4$  cells/well into 96-well plates, incubated until 80% confluency and subsequently treated with SPION/PA (75  $\mu\text{g}/\text{mL}$ ). After 6 h of incubation, medium was discarded and unbound particles were removed by washing with PBS (10x) three times. The cells were then fixed with 4% paraformaldehyde (100  $\mu\text{L}$ ) for approximately 15 min. A mixture of 6 N HCl: 20%  $\text{K}_4\text{Fe}[\text{CN}]_6$ , 1:1 (v:v) was prepared immediately prior to use, and 100  $\mu\text{L}$  of solution was added to each well. Cells were then incubated for 60 min, washed with PBS and examined under optical microscope at various magnifications.

#### **2.4.9.3 Microtubule formation assay**

The microtubule formation assay was performed on 96-well plates coated with 40  $\mu\text{L}$ /well of Matrigel (BD Biosciences, Bedford, MA, USA). Matrigel was incubated at 37 °C for 30 min to allow polymerization. HUVECs were seeded at  $4 \times 10^4$  cells/well. SPIONs (75  $\mu\text{g}/\text{mL}$ ) were added to cell suspension after seeding. After taking bright field images of cells at 6 h and 24 h, tubule formation was quantified by measuring the tube length of the capillary tubes in at least three images using NIH ImageJ software.

#### **2.4.10 Animal breast cancer model**

All protocols involving animals were approved by the Institutional Animal Care and Use Committee of Diskapi Yildirim Beyazit Training and Research Hospital. A total of 36 Sprague-Dawley rats (12-14 week old, weighing about 200-250 g) were supplied from ADACELL Laboratories (Ankara, Turkey) and used for MRI experiments and histological studies. Animals were randomly divided into two groups (healthy and tumor-bearing). Animals were maintained at constant temperature and a relative humidity of 50–60% under 12 h light/dark cycles, and had access to food and water ad

libitum. Initially, preliminary experiments was performed on 6 rats to optimize DMBA to create cancer model. Mammary carcinomas were induced through subcutaneous injections into the second right mammary pads of adult 2 female rats using single doses of 20, 50 and 80 mg/kg body weight of DMBA dissolved in sesame oil. Rats were palpated weekly to check for tumor formation. Spontaneous mammary tumor formation was observed 3 months after chemical injection in each group. The volume of each tumor was measured by digital caliper and calculated using the following formula: Tumor volume ( $\text{mm}^3$ ) =  $(D \times d^2)/2$  (D: big diameter, d: small diameter of tumor)<sup>157</sup>. MRI measurements were performed when tumor volumes reached 100  $\text{mm}^3$ .

#### **2.4.11 MRI analyses**

In order to evaluate the efficiency of SPION/K-PA as a negative contrast agent for MRI, healthy and tumor-bearing rats were randomly divided into 3 groups (n= 4-6) and imaged with or w/o SPION/K-PA administration. A without-injection group was used as control. In other groups, rats were slowly injected with SPION/K-PA (5 mg Fe/kg body weight in 5% dextrose solution) through the tail vein and sacrificed after 4 h or 15 days. During imaging, Spraque-Dawley rats were anesthetized by intraperitoneal injection of ketamycin (80 mg/kg) and xylazine (20 mg/kg). MRI was performed using a 1.5 T clinical whole body MR scanner (Philips MR system) within a sense C3 small surface coil (Figure 2.17). Images of rats were obtained immediately prior to SPION treatment, during nanoparticle injection, and at 1 h, 4 h and 15 days after injection, with the following sequences and parameters: m-GRASE (gradient and spin-echo weighted imaging): act.TR (ms) 2126, active TE (ms) n\* 18, field of view

(cm) 160 x 200, min slice gap (mm) 0, thickness 2.2 mm, ACQ matrix Mxp (mm) 84 x 72. T2-weighted spin echo coronal: TR (ms) 3000, TE (ms) 80, field of view (cm) 160 x 200, slice gap (mm) 0, thickness 2.2 mm, ACQ matrix Mxp (mm) 388 x 270. T2-weighted fat sat: TR (ms) 3000, TE (ms) 80, field of view (cm) 160 x 200, slice gap (mm) 0, thickness 2.2 mm, ACQ matrix Mxp (mm) 388 x 270. All MRI data were transferred to and analyzed on a diagnostic workstation equipped with a dedicated software for MRI examination (Philips extended MR workspace 2.6.3.4 2009). Images were evaluated by two radiologists with a minimum of 10 years of experience in the field of body MRI. In order to compare SPION-mediated darkening, all images were collected at the same image depth. Signal intensities (SI) of the regions of interest (ROI) were collected from circles of equivalent sizes (~ 5 mm diameter) drawn on the liver, spleen, kidney, breast or tumor tissue. The same procedure was applied to the no-injection group as control. Signal intensity differences were analyzed from all slice images of all tested organs and the breast tumor. Relative signal enhancement was calculated using SI values acquired before (SI pre) and after (SI post) the injection of SPIONs, per the following formula:  $1 + [(SI \text{ post} - SI \text{ pre})/SI \text{ pre}]$ .



**Figure 2. 17** MRI procedure.

#### **2.4.12 Histological analyses**

Histological analysis was performed on tissues obtained from the harvested organs, and their general appearances, clearance profiles and tissue distributions were evaluated to further analyze the *in vivo* biosafety and efficiency of SPION/K-PA. Animals were euthanized after the completion of MR imaging. Mammary tumor, liver, spleen, and kidneys were dissected and fixed overnight in 10% formalin, embedded in paraffin, sectioned with a Leica microtome (5  $\mu$ m thickness), and stained with hematoxylin and eosin (H&E) as described elsewhere<sup>158</sup>. Iron deposits were identified using standard Prussian blue staining protocol. Histological sections were observed under optical microscopy.

#### **2.4.13 Statistical analysis**

All data were presented as  $\pm$  SEM for all *in vitro* and *in vivo* results. Plotting was performed using the GraphPad Prism 5 software (La Jolla, CA). Viability results were evaluated using one-way analysis of variance (ANOVA) with Tukey's test for group-wise comparisons. MRI results were compared by two-way ANOVA test. p values less than 0.05 were considered as statistically significant. Statistical analyses of tube length were performed using two-way ANOVA with Bonferonni multiple comparison test.

## **Chapter 3**

### **INTERACTIONS BETWEEN METAL IONS AND BIOMACROMOLECULES**

Part of this thesis is published in the following article<sup>159, 160</sup>; Reprinted from

“Comparison of Au(III) and Ga(III) Ions’ Binding to Calf Thymus DNA: Spectroscopic Characterization and Thermal Analysis”; Sarioglu O.F., Gursacli R., Ozdemir A., Tekinay T., Biol Trace Elem Res., 2014, pp:445-52 and “Comparative serum albumin interactions and antitumor effects of Au(III) and Ga(III) ions”; Sarioglu O.F., Ozdemir A., Karaboduk K., Tekinay T., J Trace Elem Med Biol. 2015, pp:111-5; with permission from Springer and Elsevier, respectively.

### 3.1 INTRODUCTION

The development of metal-based anticancer drugs mainly started after the observation of accumulation of cisplatin and its analogues around the tumor site clinically. Platinum (Pt) based drugs for oncology therapy have attracted an increasing interest in the last 30 years<sup>161</sup>. On the other hand, heavily restricted activity and a number of toxic effects of these drugs have triggered an increased research about non-Pt metal-based agents<sup>162, 163</sup>. As an alternative to Pt, a large family of gallium, gold, ruthenium, germanium, cobalt, copper and zinc containing complexes have been developed<sup>164</sup>. The second metal species that have been approved for cancer therapy is the gallium (Ga), which can preferentially accumulate into mitochondria and impair mitochondrial functions of tumor cells through p53-dependent mechanism<sup>165</sup>. Furthermore, gallium nitrate salt has been used for the treatment of hypercalcemia, Hodgkin's lymphoma and bladder cancer<sup>166-168</sup>. Due to having similar chemical properties with Fe(III), especially with respect to ionic radius, electron affinity, electronegativity, coordination geometry and Lewis bases affinity<sup>163, 167</sup>, Ga can participate in iron related cellular processes or interact with proteins responsible for iron metabolism<sup>168</sup>. Actually, one of the anticancer mechanism of action of this metal is based on disrupting iron dependent proliferation and other iron containing processes in cancer cells<sup>169</sup>. One mechanism is through binding to the enzyme ribonucleotide reductase and inhibiting its catalytic activity. Ribonucleotide reductase is necessary for DNA replication and DNA repair, and it blocks apoptosis by catalyzing the reduction of ribonucleotides to deoxyribonucleotides. In this way, it can prevent the activation of the proapoptotic factors Bax and caspase-3<sup>161, 163, 170</sup>. Also gallium complexes can exhibit antitumor

activity in the presence of phenolate rings<sup>171</sup>, amine and pyridine groups by inhibiting the activity of proteasome<sup>172</sup>.

The most important advantage of Gallium nitrate is the lack of cross-resistance with conventional chemotherapeutic drugs and the absence of myelosuppressive function. Also this metal salt can be used when the blood count is low<sup>169</sup> and other drugs have failed.

Au(III) compounds are isoelectronic and isostructural with Pt(II) complexes, with which they share a square-planar tetracoordinated geometry. Therefore, gold (Au) can act in a similar way to that of the Pt(II) complexes. Recently, several biologically stable and non-toxic Au(III) complexes have been synthesized and evaluated in terms of *in vitro* and *in vivo* anti-cancer activities on various mice/ rat models against neuroblastoma<sup>173</sup>, melanoma, hepatocellular carcinoma<sup>174</sup>, colon cancer<sup>175</sup>, nasopharyngeal carcinoma (NPC)<sup>176</sup> and NPC-associated metastasis. It was reported that, Au(III) complexes can inhibit the activities of thiol-containing enzymes such as thioredoxin reductase<sup>177</sup>, through ligand exchange reactions to form Au–S(Se) bonds<sup>178</sup> or inhibit telomerase and STAT3 activity<sup>179</sup>. In addition, these complexes are capable of producing reactive oxygen species (ROS)<sup>180</sup> which results in cellular damage.

Due to the importance of DNA on regulation of biological processes and cell division, several DNA targeting metal binders have been developed as effective chemotherapeutic agents<sup>181, 182</sup>. These agents interact with DNA through several modes; coordination to bases, groove binding, intercalative and insertion binding, and dual-mode coordination and intercalation. Thus they interfere with the replication

process and inhibit the proliferation of cancer cells<sup>164</sup>. Therefore, understanding the specific binding sites on DNA and binding modes of complexes is important for elucidating the nature of metal-induced structural changes (e.g. bending, loss of base pairing, base extrusion, and intercalation), as well as the kinetics and mechanism of their formation<sup>183</sup> which could help the development of new metal based reagents and the characterization of these anticancer drugs<sup>182</sup>. HSA is composed of a single polypeptide chain of 585 amino acids that is divided into three homologous domains (I-III): I (1-195), II (196-383) and III (384-585); and each domain consists of two subdomains (A and B)<sup>184</sup>. HSA is the most abundant protein in blood and the biological carrier of various biological, synthetic materials and drugs. F. Kratz reviewed the different drug delivery systems that uses serum albumin as a drug carrier<sup>185</sup>. Binding of a drug to serum albumin affects pharmacokinetics, stability and half-life of this drug<sup>186</sup>. Due to its major role in blood, small molecules-HSA interactions has been an essential field of research in biochemistry, life sciences, clinical medicine and toxicology for the last decades<sup>184</sup>.

In this chapter, we describe and compare the effects of Au(III) and Ga(III) bindings on CT DNA, HSA and differential cytotoxicity of these two metal ions on breast cancer cells via several analytical methods. These results will be crucial for future studies involving the antineoplastic properties of these metals.

## **3.2 RESULTS and DISCUSSION**

### **3.2.1 Binding of DNA with Metal Ions**

#### **3.2.1.1 Characterization of the Binding of Metal Ions to DNA by UV-Visible (UV-Vis) Absorbance Spectroscopy**

UV-Vis absorbance measurement is a common method to investigate the structural changes of DNA and HSA. In order to explore structural alterations of CT DNA with the addition of metal ions, the UV-Vis absorption spectra were observed.

As seen in Figure 3.1, free CT DNA showed absorbance band at 258 nm, and displayed altered intensities in the presence of metal ions. It can be seen that the addition of Au(III) ions resulted in a gradual and concentration-dependent increase (hyperchromism) in the absorbance spectrum, while Ga(III) ions triggered a slight and again concentration-dependent decrease (hypochromism). The observed changes in the absorption of DNA in the presence of Au ions may be due to the intermolecular interactions between DNA and metal ions.

It is reported that hyperchromism and hypochromism are the absorption spectra features of DNA due to the double helical structure. Although hypochromism is related to charge-transfer interactions and gives insight into conformational changes of DNA, hyperchromism is the indicator of DNA melting and denaturation<sup>112</sup>. According to the UV-Vis absorbance data, DNA denaturation may result from the interaction between Au ions and DNA. On the other hand, Ga may not disrupt DNA structure. This analysis suggested that Au(III) and Ga(III) ions bind to DNA by different binding modes and affinities. In addition, Au(III) ions show stronger binding characteristics than Ga(III), since Au bears a higher impact on the spectral intensity of DNA.

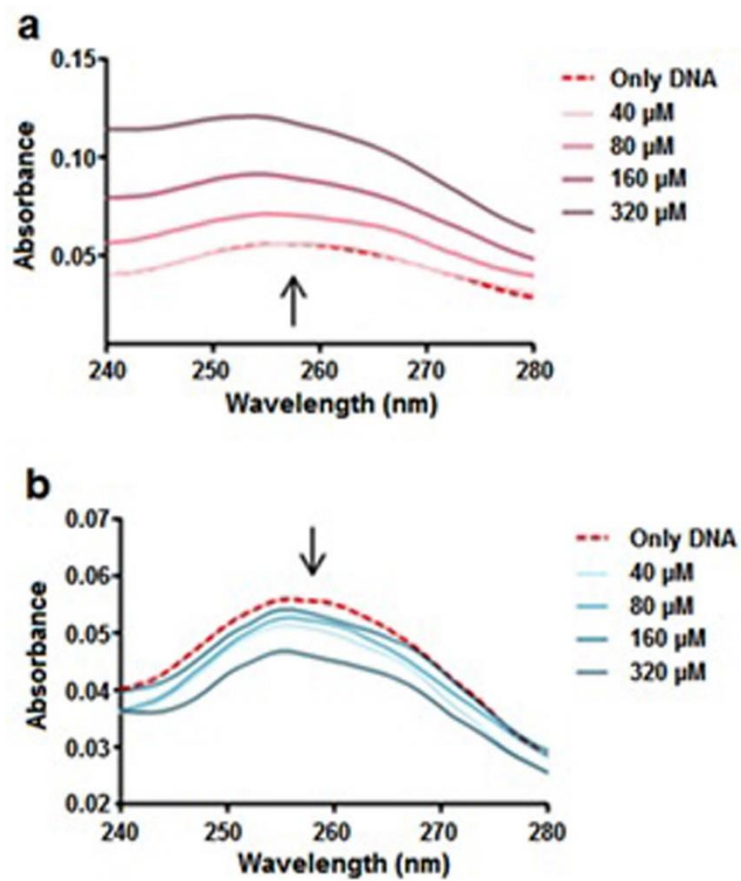


**Figure 3.1** UV-Vis absorbance spectra of CT DNA-metal system within 240–280 nm. Concentrations of 0, 40, 80, 160, and 320  $\times 10^{-6}$  M were used for **a)** Au(III) and **b)** Ga(III) ions. pH = 7.4.

### 3.2.1.2 Competitive Binding of Au(III) and Ga(III) Ions with EtBr-DNA Mixture

Competitive ethidium bromide (EtBr) displacement experiments were performed to test whether metal ions are capable of intercalative binding to DNA, and whether the intercalative binding strengths change with increasing metal ion concentrations. Displacement was monitored by a decrease in EtBr–DNA fluorescence in the presence of metal ions (Table 3.1). The fluorescence emission spectra of intercalated EtBr with increasing concentration of metal ions, especially at higher concentrations, represented a significant reduction of the emission intensities of EtBr-DNA mixture and quenching of its fluorescence. Though this result may suggest both metal ions are capable of intercalating between CT DNA strands, it is known that groove binders can also cause a reduction in the emission intensity of EtBr-DNA mixtures, so Au(III) and Ga(III) ions may have groove binding properties<sup>187</sup>.

**Table 3.1** Relative fluorescence ratios of EtBr-CT DNA mixture after incubation with varying molar ratios of Au(III) and Ga(III) ions.<sup>a</sup>

[metal ion]/[ctDNA]	Relative Fluorescence (F) (%)	
	Au(III)	Ga(III)
0.25	95 ± 1.54	98.03 ± 0.99
0.5	93.31 ± 1.77	90.89 ± 5.03
1	71.74 ± 6.51	74.54 ± 5.31
2	49.81 ± 1.85	42.56 ± 6.72

<sup>a</sup> DNA concentrations were constant for all samples (200 μM), while metal ion concentrations were varying (50-100-200-400 μM).

### 3.2.1.3 Analysis of Conformational Changes

Circular dichroism (CD) is a method based on the interactions of chiral molecules with circularly polarized electromagnetic rays. The differences between the absorption of right and left handed circularly polarized light by chiral molecules produce CD signal. Generally, ellipticity, which describes the quantity of CD signal, is expressed in degrees<sup>188</sup>. In the past decades, this technique has been commonly used to study nucleic acid structures and to monitor conformational polymorphism of DNA (B-form, A-form and Z-form) upon addition a molecule.

As a mean for further exploring the binding of the metal ions to DNA, CD spectra were recorded when varying concentrations of Au(III) and Ga(III) ions were added to CT DNA. The B-conformation of DNA is characterized by two positive peaks at 220 and 275 nm and a negative peak at 245 nm<sup>189</sup>. The peak around 245 nm corresponds to the helicity of DNA, and the peak around 275 nm corresponds to the stacking of DNA bases<sup>190</sup>. It is known that an intensity increase at 275 nm can be attributed to B to A conformational transition<sup>191</sup>. Our CD spectra revealed that metal-DNA bindings do not significantly alter the DNA structure. Interaction between DNA and Au(III) ions causes reduction in the intensities of CD values at 245 nm and no consistent change at 275 nm was observed, which may indicate that the right-handed helicity of B-DNA is modified (Figure 3.2a). There is no peak shift and no increase in the spectra of Au samples at 275 nm. These results indicated that DNA structure does not change after Au ion binding. After the addition of Ga, we observed minor changes at 245 and 275 nm in the CD spectra (Figure 3.2b). Apparently, Ga(III) ions are not as influential as Au(III) ions on CT DNA. Furthermore, as with Au(III) samples, Ga(III)-DNA

interactions may take place without conformational transitions in DNA structure. Although intercalators are known to enhance the intensities of both positive and negative bands, groove binders demonstrate less or no perturbation on the helicity and base stacking bands<sup>192</sup>. Therefore, the lack of distinct signatures for conformational transitions in our CD results suggested that both Au(III)-DNA and Ga(III)-DNA interactions might occur without conformational changes in DNA. In contrast, EB displacement assay results suggested that Au(III) and Ga(III) ions display intercalative binding properties. The lack of large perturbations and intensity enhancements in CD bands of metal-DNA complexes indicate that groove binding might be more responsible for metal-DNA interactions.

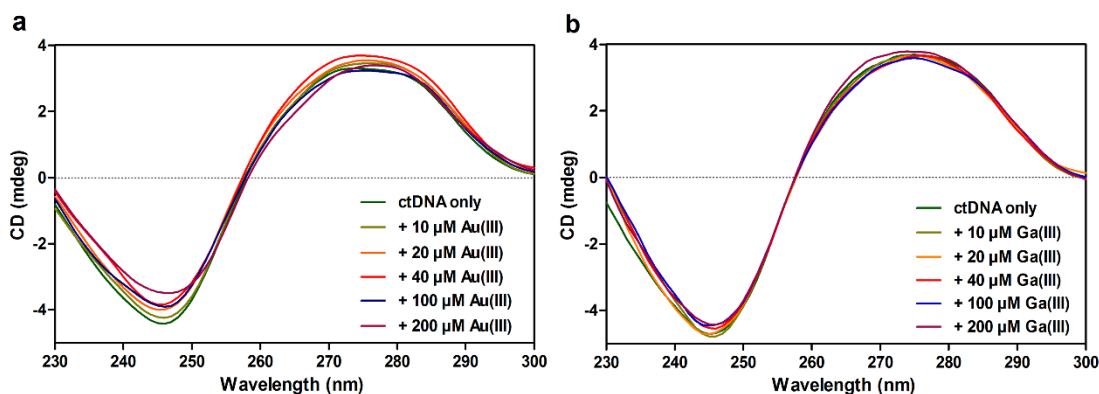


**Figure 3.2** CD spectra of CT DNA titrated with varying molarities of **a)** Au(III) and **b)** Ga(III) ions within 230–300 nm region.

#### 3.2.1.4 Thermodynamics of DNA Binding

Isothermal titration calorimetry (ITC) is a well-known and experimentally simple technique that measures the released or absorbed heat during the reaction. ITC directly measures enthalpy changes associated with interactions. Experiments can yield binding isotherms allowing quantification of equilibrium binding constants, and almost all thermodynamic profile that can be obtained as well<sup>113</sup>. The most important advantages of using this technique are to characterize the thermodynamics of biomacromolecule binding interactions and the sensitivity of system because of the improvements in data analysis software and ITC instrumentation. ITC gives opportunity to measure heat effects as small as 0.1  $\mu\text{cal}$  (0.4  $\mu\text{J}$ ), heat rates up to 0.1  $\mu\text{cal}/\text{sec}$ , binding constants as large as  $10^8$ – $10^9 \text{ M}^{-1}$  and reaction rates in the range of  $10$ – $12 \text{ mol}/\text{sec}$ <sup>193</sup>. Therefore, it is useful for studying biomacromolecule – metal interactions.

Figure 3.3 shows the ITC results of the both Au(III)-DNA and Ga(III)-DNA reactions. Reactions are exothermic and Au(III)-DNA interaction is much more favorable than Ga(III)-DNA interaction at ambient conditions. Actually, the reactions were conducted under constant pressure and temperature conditions. Au(III)-DNA and Ga(III)-DNA reactions displayed negative  $\Delta G$  values (Table 3.2), and occur spontaneously through forward direction at ambient conditions. Au(III)-DNA binding seems to have a higher spontaneity over Ga(III)-DNA binding, though the homogeneity of both reactions avoids the accurate prediction of reaction spontaneities. The metal–DNA binding constants were in the range of  $10^5$ – $10^6 \text{ M}^{-1}$ . The values on Table 3.2 demonstrated that Au(III) ions bind to DNA with a much higher affinity than Ga(III) ions. According to

$\Delta H$  and  $\Delta S$  values, there are considerable differences between Au(III)-DNA and Ga(III)-DNA bindings, such that Au(III)-DNA binding is enthalpically more favorable but entropically less favorable than Ga(III)-DNA binding. In addition, these values were negative in both cases, and since the  $\Delta G$  values were negative, the reactions are enthalpy driven. Overall data indicated that non-covalent interactions (e.g. electrostatic, van der Waals) are dominant between Au(III)-DNA and Ga(III)-DNA bindings<sup>194</sup>.

As a summary, binding reactions of Au(III)-DNA and Ga(III)-DNA are likely to be spontaneous at ambient conditions, Au(III)-DNA binding was observed to be much more favorable and much stronger than Ga(III)-DNA binding. This data provide another support for the interaction between these metal ions and the DNA double helix. Measurement of the strength of association of metal ions with DNA via ITC has important implications in chemical modifications and drug design strategies for biomedical usage of these metals.

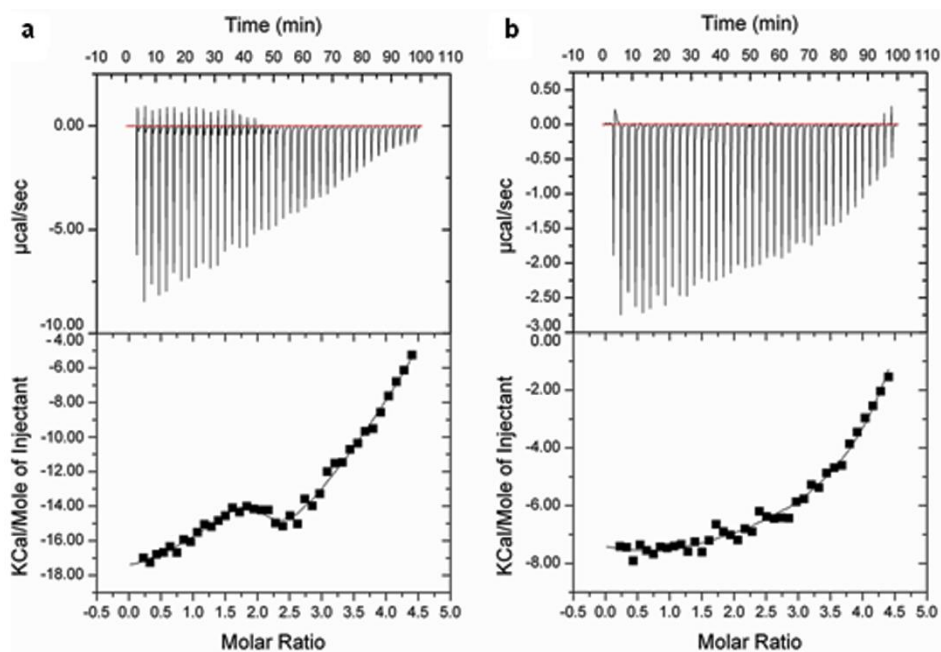


**Figure 3.3** ITC final thermograms of **a)** Au(III)-DNA and **b)** Ga(III)-DNA bindings.

**Table 3.2** Thermodynamic parameters obtained by ITC analysis for the binding of CT DNA with Au(III) or Ga(III) ions.

Thermodynamic parameters	Au(III)	Ga(III)
<b>K<sub>a</sub> (binding affinity)</b> M <sup>-1</sup>	1.43 x 10 <sup>6</sup> ± 3 x 10 <sup>5</sup>	1.17 x 10 <sup>5</sup> ± 1 x 10 <sup>4</sup>
<b>ΔH (enthalpy change)</b> cal/mol	-1.745 x 10 <sup>4</sup> ± 242	-7735 ± 1 x 10 <sup>3</sup>
<b>ΔS (entropy change)</b> cal/mol/deg	-30.3	-2.74
<b>ΔG (Gibbs free energy change)</b> kJ/mol	-35.12	-28.92

### 3.2.1.5 Investigation of Metal Ion Binding by Vibrational Spectroscopy

Fourier transform infrared (FT-IR) spectroscopy is a physic-chemical method based on measurement of vibration of a molecule excited by IR radiation at a specific wavelength range (commonly mid-IR region: 400-4000  $\text{cm}^{-1}$ ). Simply, the principle of FT-IR spectroscopy can be explained as; When IR radiation is passed through a molecule, specific wavelengths are absorbed resulting in the chemical bonds in the sample to vibrate (contracting, stretching, or bending). Functional groups of a molecule always absorb radiation in the same wavenumber range, thus band position gives an idea about the chemical structure in the molecule or changes in the structure<sup>195</sup>. Due to the being convenient, rapid, and non-destructive, requiring less sample preparation requirements, and working under a wide variety of conditions<sup>196</sup>, FT-IR is a powerful technique to examine DNA and protein structure.

FT-IR spectroscopy was performed to determine changes in the double helical structure of DNA after the addition of Au(III) and Ga(III) ions within 600–1800  $\text{cm}^{-1}$  region. The marker bands were chosen for different chemical groups; 1715  $\text{cm}^{-1}$  for guanine, 1663  $\text{cm}^{-1}$  for thymine, 1602  $\text{cm}^{-1}$  for adenine, 1496  $\text{cm}^{-1}$  for cytosine, 1227  $\text{cm}^{-1}$  for asymmetric phosphate, 1080  $\text{cm}^{-1}$  for symmetric phosphate, 1060  $\text{cm}^{-1}$  for sugar phosphate, 1038  $\text{cm}^{-1}$  for carbohydrate, 967  $\text{cm}^{-1}$  for backbone marker, 891  $\text{cm}^{-1}$  for deoxyribose and 818  $\text{cm}^{-1}$  for B-conformation marker<sup>190, 197-199</sup>. Typically, the marker bands at 1710–1717  $\text{cm}^{-1}$  (guanine), 1222–1227  $\text{cm}^{-1}$  (asymmetric  $\text{PO}_2$  stretching), and 825  $\text{cm}^{-1}$  (B-conformation marker) are observed in the spectrum of free DNA with B conformation<sup>197</sup>. As seen from Figure 3.4, minor spectral shifts were observed for these B-conformation markers after binding of metal ions. Table 3.3

shows that there are minor spectral shifts for nucleotide base markers (guanine, thymine, adenine and cytosine), which may indicate that the metal-DNA bindings occur via non-intercalative interactions. The absence of major shifts in phosphate associated bands and the marker bands revealed that CT DNA may remain in B-family structure after Au(III) or Ga(III) ions' binding<sup>198</sup>. Also the observed small shifts in the band of sugar conformation may results from indirect effect of the metal ion binding to DNA<sup>200</sup>.

As a summary, minor shifts were observed in nucleotide base peaks and no apparent alterations occurred on the conformation of CT DNA following both Au(III) or Ga(III) ions binding. The absence of a significant alterations in the position of bases and the conformation of DNA suggested that these ions may not directly capable of influencing DNA synthesis, replication or transcription processes<sup>200</sup>. In addition, metal ions may bind to DNA mainly through groove binding and non-covalent interactions instead of intercalation.

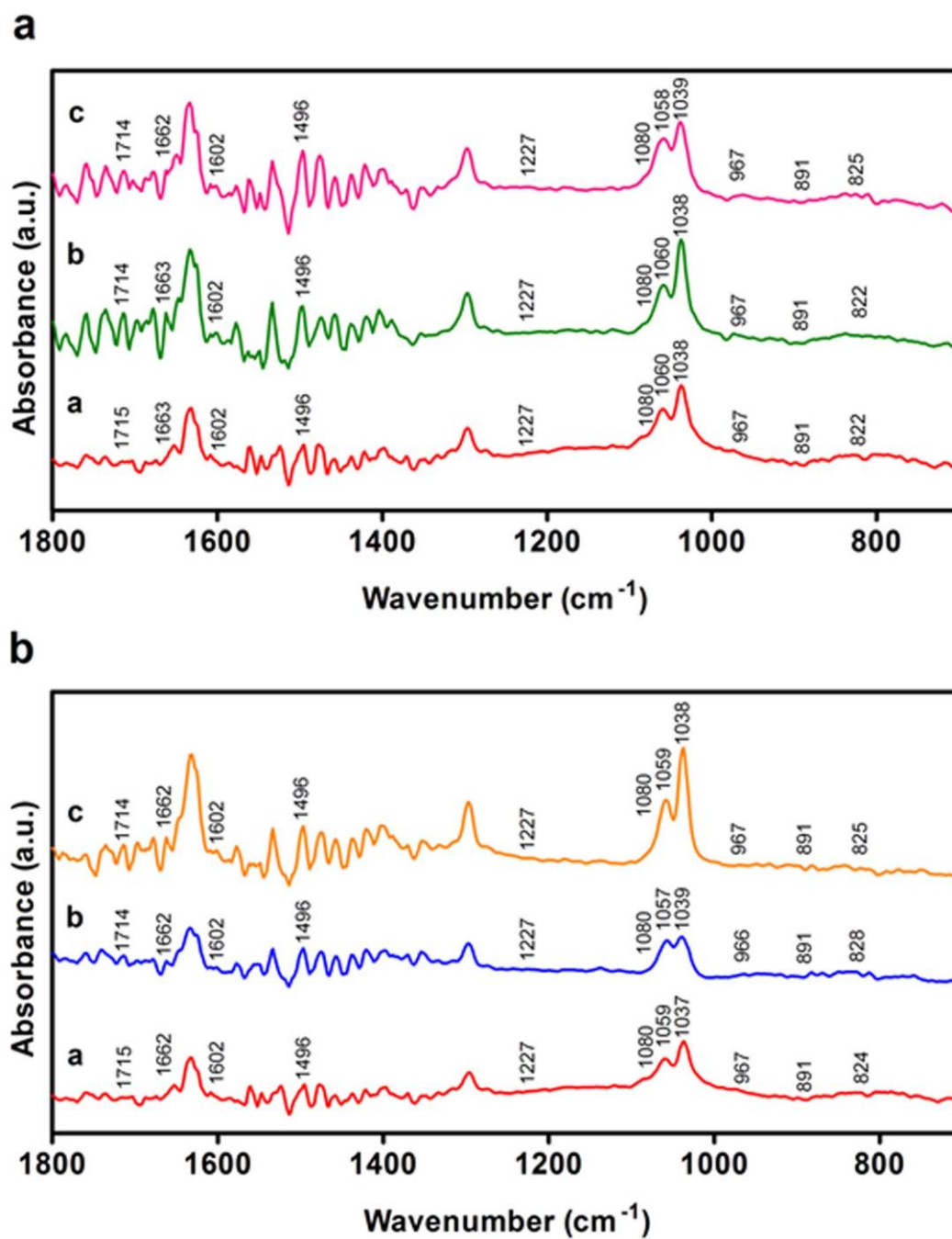


**Figure 3.4** FT-IR spectra of CT DNA in the range of  $600^{-1}, 800^{-1}$   $\text{cm}^{-1}$  when treated with varying molarities of **a**) Au(III), and **b**) Ga(III) ions (a: 0, b: 100, c: 200  $\mu\text{M}$  of metal ions).

**Table 3.3** Peak positions and spectral shifts of the Au(III)-DNA and Ga(III)-DNA complexes at different molar ratios.

DNA bands	Free ctDNA	DNA – 100 $\mu$ M Au(III)	DNA – 200 $\mu$ M Au(III)
Guanine	1715	-1	-1
Thymine	1663	0	-1
Adenine	1602	0	0
Cytosine	1496	0	0
Phosphate asymmetric	1227	0	0
Phosphate symmetric	1080	0	0
Sugar phosphate			
Carbohydrate	1060	0	-2
	1038	0	+1
Backbone marker	967	0	0
Deoxyribose	891	0	0
B- conformation marker	822	0	+3

DNA bands	Free ctDNA	DNA – 100 $\mu$ M Ga(III)	DNA – 200 $\mu$ M Ga(III)
Guanine	1715	-1	-1
Thymine	1662	0	0
Adenine	1602	0	0
Cytosine	1496	0	0
Phosphate asymmetric	1227	0	0
Phosphate symmetric	1080	0	0
Sugar phosphate			
Carbohydrate	1059	-2	0
	1037	+2	+1
Backbone marker	967	-1	0
Deoxyribose	891	0	0
B- conformation marker	824	+4	+1

### 3.2.2 HSA Studies

#### 3.2.2.1 Analysis of Electronic Spectra to HSA

UV-Vis absorption measurement is a simple method to explore structural changes of serum albumin and examine serum albumin-metal ion interactions. In order to examine structural alterations of HSA in the presence of metal ions, UV-Vis spectra were recorded within 260-300 nm. Typically, HSA shows absorption peak at about 280 nm due to the aromatic residues (tryptophan, tyrosine, phenylalanine) in the protein<sup>201</sup> (Figure 3.5). With the addition of Au(III) ions, we observed a gradual increase in the total intensity of absorbance at 280 nm, whereas Ga(III) ions did not show a significant difference on the HSA spectra. This result may indicate stronger binding characteristics and higher binding affinity for Au(III) ions, since Au(III) ions have a higher impact on the spectra of HSA in a concentration dependent manner. The gradual enhancement in UV intensity by the addition of Au(III) ions may cause the exposure of a large hydrophobic pocket (i.e., IIA subdomain of HSA), which contains a tryptophan (Trp-214), to the surrounding aqueous environment<sup>162, 202</sup>. The absence of any blue (towards shorter wavelengths) or red (towards longer wavelengths) shift provides information about stable polarity of the protein environment upon metal ion binding<sup>203</sup>. UV-Vis absorbance results revealed that the structure of HSA seems to be more changed upon interaction with gold, rather than Ga.

It is known that HSA has reactive thiol (-SH) group (Cys34) in its structure and these groups have important function during antioxidant activity of the protein<sup>204</sup>. The high binding affinity of Au(III) ions to thiol group of the serum protein may increase the stability of HSA- Au(III) complex<sup>178</sup>.

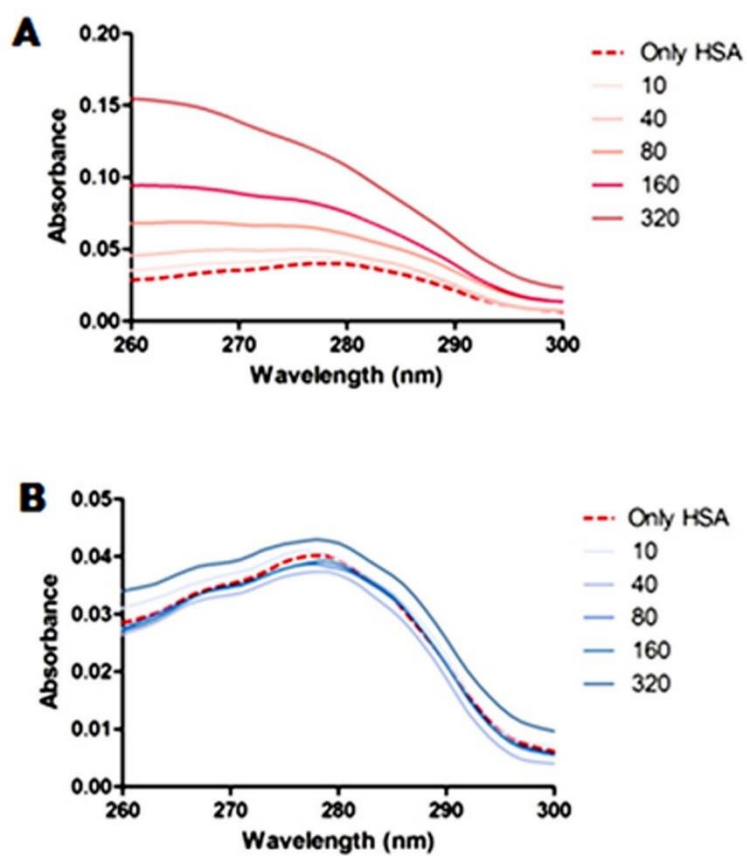


**Figure 3.5** Absorption spectra of HSA with various amount of metal ions. **A)** Au(III)-HSA and **B)** Ga(III)-HSA, and the concentrations of Au(III) chloride hydrate and Ga(III) nitrate hydrate salts used are; 0, 10, 40, 80, 160, 320  $\mu\text{M}$ .

### 3.2.2.2 Analyses of Effects of Binding of Metal Ions to Fluorescence Emission of HSA

When a substance absorbs UV light or electromagnetic radiation, it raises to an excited electronic state. Fluorescence is the emitted light during transition from an excited state to a lower energy state. Fluorophores are the main compounds responsible for re-emitting light. Proteins containing several aromatic groups, or plane or cyclic structure with several  $\pi$  bonds exhibit fluorescence in the ultraviolet region. The known fluorophores in proteins are phenylalanine, tyrosine and tryptophan amino acids. Although three of these amino acids are capable of giving fluorescence, tryptophan (Trp) is the essential contributor of the process<sup>205</sup>. The fluorescence of HSA is mostly triggered by the Trp, because phenylalanine has a very low quantum yield and the fluorescence that comes from tyrosine is drastically quenched by the presence of an amino group, a carboxyl group or a Trp near to the tyrosine<sup>206</sup>.

The effect of metal ions on the fluorescence of HSA was evaluated by fluorescence quenching experiments. The characteristic fluorescence emission peak of HSA was observed at 345 nm (Figure 3.6). The addition of Au ion led to a much more decrease in the fluorescence intensity of HSA along with a spectral shift towards shorter wavelengths than the Ga ions at the same concentration range. According to fluorometric measurements, the electrostatic interaction is the predominant intermolecular force for binding of metal ions to serum protein<sup>207</sup>. The blue-shift in some of the emission spectra can be attributed to the electron density shift from the benzene ring to the pyrrole ring upon excitation<sup>208</sup>. These data revealed that metal ions interact with serum albumin and quench its fluorescence. Furthermore, Au(III) is

inferred to be better than Ga(III) in quenching the fluorescence, which may result from a stronger interaction between Au(III) and HSA.

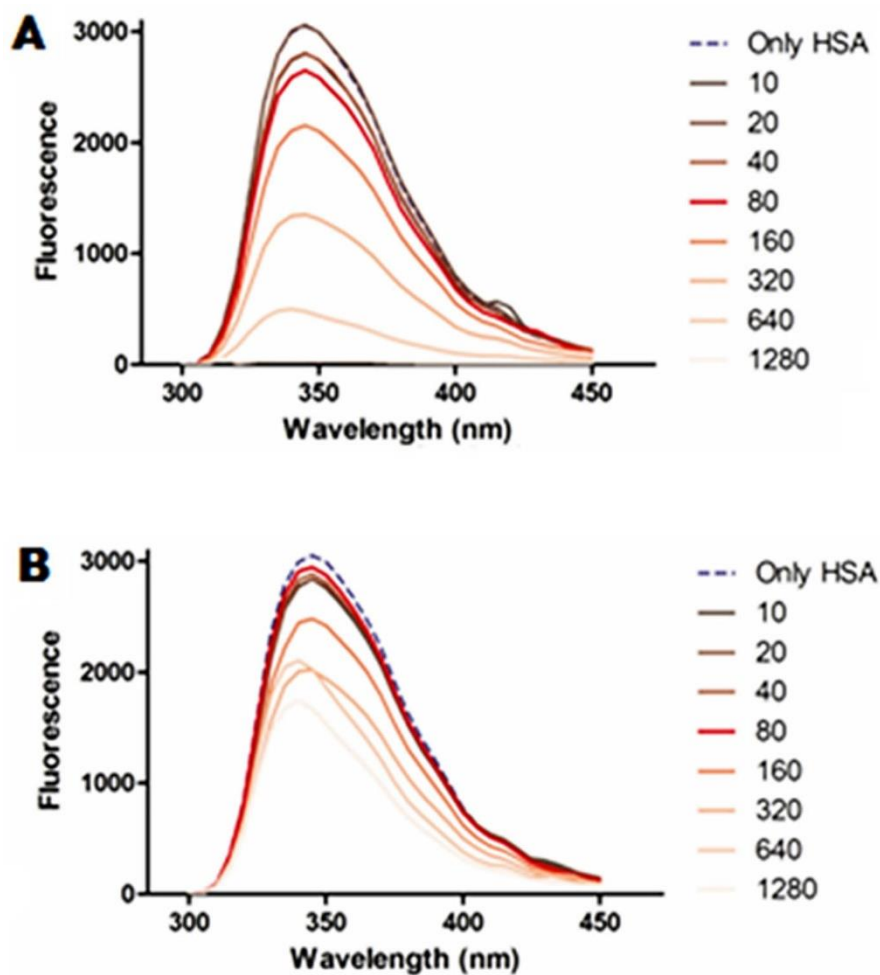


**Figure 3.6** Fluorescence spectra of HSA in the presence of **A)** Au(III), and **B)** Ga(III) ions. Metal ion concentrations = 0, 10, 40, 80, 160, 320, 640, 1280  $\mu\text{M}$ .

### 3.2.2.3 Calorimetric Investigation of the HSA-Metal Ion Binding

Isothermal titration calorimetry (ITC) is the only technique capable of measuring the magnitude of the binding affinity and thermodynamic parameters directly in one run<sup>209</sup>. ITC was used for the analysis of binding thermodynamics. Titration experiments were performed where metal ions were titrated into the HSA solution, not only thermodynamic parameters but also binding constants and the stoichiometry of the complexes were obtained at a constant temperature and under constant pressure by ITC.

The interaction enthalpy change of the binding between metal ions and HSA showed that serum albumin provided a stronger interaction to Au ions than to Ga ions (Figure 3.7). The thermodynamics of associations were demonstrated in Table 3.4 by the stoichiometry of the interaction ( $n$ ), the association constant ( $K_a$ ), the free energy ( $\Delta G$ ), enthalpy ( $\Delta H$ ), and entropy ( $\Delta S$ ).  $\Delta H$ ,  $\Delta S$  and  $\Delta G$  values were all negative in both reactions, the reactions are enthalpy driven and it reveals that non-covalent interactions (e.g. electrostatic, van der Waals) are dominant between Au(III)-HSA and Ga(III)-HSA bindings<sup>194</sup>. Au(III) has a much higher affinity to serum albumin than Ga(III)-HSA. In terms of enthalpy and entropy values of these reactions, Au(III)-HSA binding is enthalpically more favorable but entropically less favorable than Ga(III)-HSA binding.  $\Delta G$  values of Au(III)-HSA and Ga(III)-HSA bindings were negative, hence these reactions are exergonic and are likely to occur spontaneously through forward direction at ambient conditions. Although the homogeneity of both reactions evades the accurate prediction of reaction spontaneities, Au(III)-HSA binding seems to have a higher spontaneity over Ga(III)-HSA binding. Also, UV-Vis spectroscopy and fluorescence spectroscopy results are consistent with the thermal analysis results.

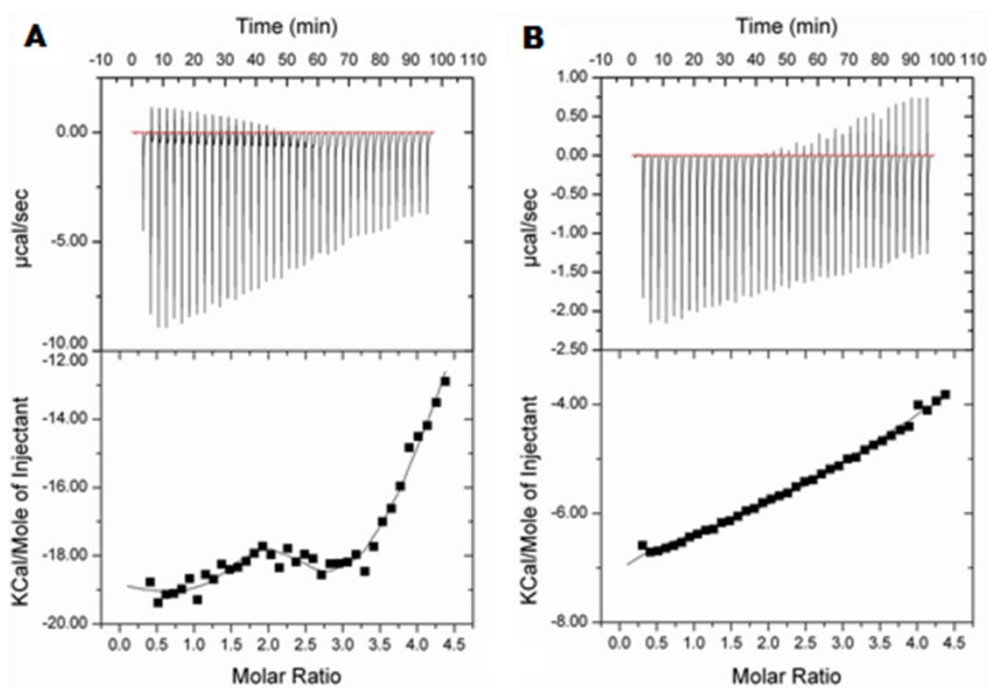


**Figure 3.7** ITC final thermograms of **A)** Au(III)-HSA, and **B)** Ga(III)-HSA bindings.

**Table 3.4** Thermodynamic parameters obtained by ITC analysis for the binding of HSA with Au(III) or Ga(III) ions.

Thermodynamic parameters	Au(III)	Ga(III)
<b>K<sub>a</sub> (binding affinity)</b> M <sup>-1</sup>	$3.87 \times 10^5 \pm 4.9 \times 10^4$	$9.68 \times 10^3 \pm 5 \times 10^2$
<b>ΔH (enthalpy change)</b> cal/mol	$-1.911 \times 10^4 \pm 255$	$-1.061 \times 10^4 \pm 231$
<b>ΔS (entropy change)</b> cal/mol/deg	-38.5	-17.3
<b>ΔG (Gibbs free energy change)</b> kJ/mol	-31.88	-22.74

#### 3.2.2.4 Analysis of Effects of Metal Ions on the FT-IR Spectra of HSA

FT-IR spectroscopy was employed for the analysis of secondary structure alterations upon Au(III) or Ga(III) binding to HSA by combining the curve-fitting results of amide I bands. Due to the different vibrations of peptide moiety, proteins exhibit characteristic amide bands and the most information about the change of protein secondary structure come from the Amide I band of proteins ranging from 1600 to 1700  $\text{cm}^{-1}$ . Fourier self-deconvolution, second derivative analysis and curve fitting procedure have been employed as described elsewhere<sup>207, 210</sup>.

Curve fitting analysis of the amide I region was performed to estimate approximate ratios of the three main subgroups of protein secondary structures with respect to the total protein content, which are adopted at the regions of: 1630  $\text{cm}^{-1}$  for  $\beta$ -sheet, 1655  $\text{cm}^{-1}$  and 1661  $\text{cm}^{-1}$  for  $\alpha$ -helix, and 1678  $\text{cm}^{-1}$  for  $\beta$ -turns. The percentage differences of these groups with respect to varying concentrations of metal ions were determined. A representative spectrum of the amide I region following the application of curve fitting analysis was demonstrated in Figure 3.8.

According to curve-fit data, the  $\alpha$ -helix content had a decrease of  $\approx 5$  and 2% after HSA interacted with Au(III), and Ga(III), respectively (Table 3.5). Although  $\beta$ -sheet structure content of the HSA increased from 25% up to 27% when HAS was titrated with Au ions, there was no considerable difference in the presence of Ga ions even at high concentration.  $\beta$ -turn content also increased 3 and 1% after the addition of Au(III), and Ga(III), respectively. FT-IR data demonstrated that the alterations in the secondary structure of serum albumin in Ga(III) samples were in  $\alpha$ -helices and  $\beta$ -turns, this was  $\alpha$ -helices,  $\beta$ -sheets and  $\beta$ -turns for Au(III) samples.

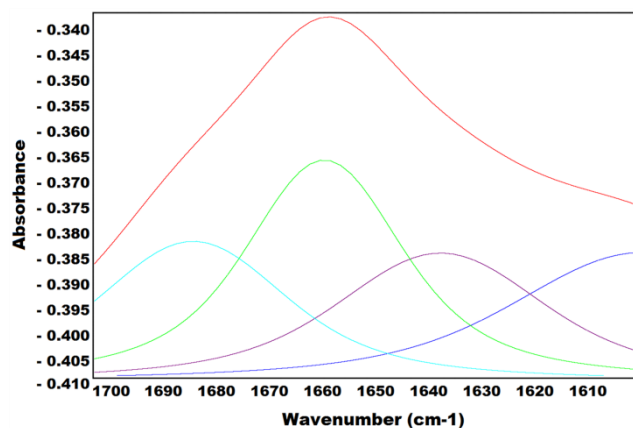


**Figure 3.8** Representative spectrum of curve-fitted amide I region of HSA.

**Table 3.5** Secondary structure of HSA upon treated with Au(III) or Ga(III) at different concentrations. The percentage of different structures were calculated as the ratio of the corresponding peak areas to the total area of all amide I peaks. The area-percentage values are the averages of duplicate samples (means  $\pm$  SEM).

	$\beta$ -sheets	$\alpha$ -helices	$\beta$ -turns
<b>HSA only</b>	1595 $\text{cm}^{-1}$ 24.98% $\pm$ 0.73	1633-1657 $\text{cm}^{-1}$ 54.96% $\pm$ 0.9	1682 $\text{cm}^{-1}$ 20.05% $\pm$ 1.63
<b>100 <math>\mu\text{M}</math> Au</b>	1599 $\text{cm}^{-1}$ 27.61% $\pm$ 0.62	1635-1659 $\text{cm}^{-1}$ 50.57% $\pm$ 0.47	1685 $\text{cm}^{-1}$ 21.81% $\pm$ 0.15
<b>200 <math>\mu\text{M}</math> Au</b>	1598 $\text{cm}^{-1}$ 27.22% $\pm$ 0.58	1633-1658 $\text{cm}^{-1}$ 49.62% $\pm$ 3.53	1683 $\text{cm}^{-1}$ 23.15% $\pm$ 0.58
<b>100 <math>\mu\text{M}</math> Ga</b>	1601 $\text{cm}^{-1}$ 24.51% $\pm$ 0.19	1634-1658 $\text{cm}^{-1}$ 54.19% $\pm$ 1.58	1684 $\text{cm}^{-1}$ 21.29% $\pm$ 0.05
<b>200 <math>\mu\text{M}</math> Ga</b>	1601 $\text{cm}^{-1}$ 24.67% $\pm$ 0.31	1635-1658 $\text{cm}^{-1}$ 53.81% $\pm$ 0.44	1683 $\text{cm}^{-1}$ 21.47% $\pm$ 0.3

### 3.2.2.5 Antitumor Activities of Au(III) and Ga(III) Ions

The antitumor activity of the metal ions was evaluated by Alamar blue assay to assess their effects on cellular proliferation in human breast cancer cell line (MCF-7) *in vitro*. Percentages of cell viability relative to non-treated control of MCF-7 cells after 24 h-exposure to Au(III) and Ga(III) ions at a concentration of 0, 50, 100, 250, 500 and 1000  $\mu\text{M}$  are shown in Figure 3.9. There is a dose dependent effect of Au ions on MCF-7 cells' viability. We observed a significant decrease in cell viability up to 10% at high concentration. On the other hand, Ga(III) ions did not exhibit significant anti-proliferative activity against these cells. At tested concentration range, the maximum impact reached 10% decrease of cell viability when exposed to Ga ions. These results revealed that the Au ions are more cytotoxic than Ga ions to breast cancer cells. Therefore, Au can be considered as a potential anti-cancer agent.

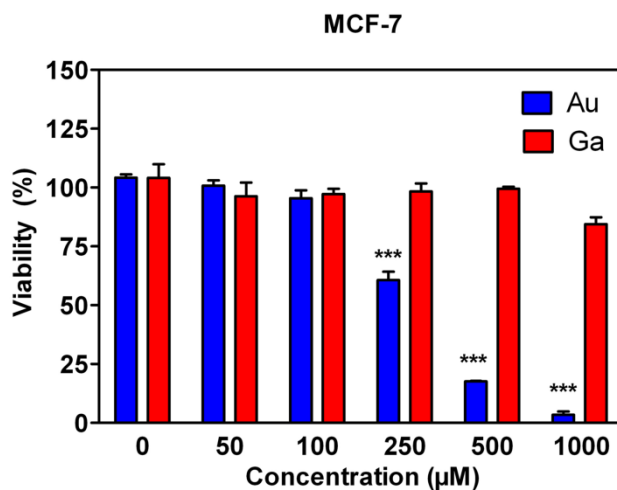


**Figure 3.9** Alamar blue cytotoxicity assay. Histogram for MCF-7 cells treated with varying concentrations of Au(III) and Ga(III) ions for 24 h. \*\*\*  $p < 0.001$ .

### 3.3 CONCLUSION

By using several spectroscopic and calorimetric techniques, we investigated binding characteristics and affinities of Au(III) and Ga(III) ions to model DNA and serum albumin.

Obtained results clearly indicated that both Au(III) and Ga(III) ions are capable of interacting with CT DNA and HSA. However Au(III) ions interact with CT DNA and HSA more favorably and with a higher affinity than Ga(III) ions. Although the interaction between metal ions and DNA does not disrupt conformation of CT DNA, high concentrations of both metal ions led to considerable changes in the secondary structure of HSA, especially in the  $\alpha$ -helix. Metal ions may interact with grooves of CT DNA and the non-covalent interactions play a major role for metal ion and DNA association. Furthermore, thermal analysis of metal-DNA interactions revealed that both reactions were exothermic at ambient conditions. The quenching in the intrinsic fluorescence of the Trp residue in HSA upon the addition of metal ions to serum albumin solution gives information on specific binding of metal ions to this site. Moreover, the dose dependent antitumor activity of the metal ions was examined by using human breast cancer cell line, MCF-7.

There are several studies about the anticancer activity of different gold complexes. They demonstrate their neoplastic function through the interaction with specific enzymes (selenolol thiol-containing thioredoxin reductase (TrxR), glutathione reductase, and peroxidase) or activation of apoptotic pathways or dysfunction of mitochondria<sup>211</sup>. Based on the interaction between Au(III), Ga(III) ions and DNA or

HSA, new strategies should be employed to increase stability of metal containing complexes and novel carriers should be designed.

Auranofin is an antirheumatic gold complex with anticancer activity. Although it demonstrates high anti-tumor properties *in vitro*, it reacts and covalently binds to the Cys-34 of serum albumin which cause toxicity *in vivo*. On the other hand, thiol proteins on cell membrane could preferentially increase uptake of serum bound Au ions. This process may reduce the observed toxicity of metal ions<sup>212</sup>.

On the other hand, the absence of anti-tumor activity of Ga(III) ions against breast cancer cells *in vitro* does not mean that it cannot be considered as anti-cancer compound. Actually, the anti-cancer activity of gallium nitrate was tested in humans with different cancers such as breast, prostate, lung, ovarian, cervical, bladder, renal, melanoma, sarcoma, chronic lymphocytic leukemia, Hodgkin's lymphoma and non-Hodgkin's lymphoma. The observations revealed that it can be used against bladder cancer and non-Hodgkin's lymphoma<sup>213, 214</sup> and combination of this compound with other drugs results in very good outcomes in the cancer treatment<sup>169</sup>.

## **3.4 EXPERIMENTAL SECTION**

### **3.4.1 Materials**

CT DNA with an initial concentration of 10 mg/mL was purchased from Invitrogen™ (USA). Au(III) chloride hydrate and Ga(III) nitrate hydrate (Sigma) were used as received. Au(III) chloride hydrate, Ga(III) nitrate hydrate, and CT DNA stock solutions were prepared in a 10 mM Tris (tris(hydroxymethyl)aminomethane)-HCl buffer (pH 7.4) throughout the experiments. Experimental solutions were made by diluting stock solutions into the buffer solutions to obtain desired final concentrations. HSA (fatty acid free, 99%) in lyophilized powder form was purchased from Sigma Aldrich (USA) and used without further purification. Solutions were freshly prepared prior to experiments.

### **3.4.2 UV-Vis absorbance spectroscopy**

Uv-Vis spectra were recorded at ambient temperature on a NanoDrop 2000 spectrophotometer (Thermo Scientific, USA). The wavelength range was 220–420 nm. Spectra were recorded at 300  $\mu$ M DNA concentration and in the presence of Au(III) chloride hydrate or Ga(III) nitrate hydrate (concentrations range from 10 to 320  $\mu$ M).

Protein binding experiments were performed by keeping the concentration of the HSA (10  $\mu$ M) constant while varying the concentration of Au(III) chloride hydrate or Ga(III) nitrate hydrate. UV-vis spectra were read after 2 h incubation of HSA and Au(III) chloride hydrate or Ga(III) nitrate hydrate solutions.

### 3.4.3 EtBr displacement assay

CT DNA and EtBr was incubated with a final ratio of 10:1 (DNA/EB) in 10 mM Tris-HCl buffer (pH 7.4), to obtain a DNA/EtBr complex solution at 25 °C for 30 min in a dark room. Varying concentrations of Au(III) chloride hydrate and Ga(III) nitrate hydrate solutions were mixed with DNA/EtBr complex for half an hour. In all samples, DNA concentration was constant (200 μM). The fluorescence measurements of the samples were obtained by a SpectraMax M5 Microplate Reader at  $\lambda_{\text{ex}}$  of 530 and  $\lambda_{\text{em}}$  of 590 nm. The fluorescence intensities of the samples were evaluated by using the equation below<sup>215</sup>:

$$F (\%) = (I - I_0) / (I_{100} - I_0) \times 100$$

where F and I are the relative fluorescence and emission intensities for EtBr-DNA mixtures at 590 nm following the addition of metal ion solutions and  $I_0$  and  $I_{100}$  donate the emission intensities of free EtBr and EtBr-CT DNA mixtures.

### 3.4.4 CD spectroscopy

CD spectra of CT DNA (200 μM), and Au(III) chloride hydrate or Ga(III) nitrate hydrate stock solutions were recorded with 1 cm path length quartz cuvette using a Jasco J-815 spectropolarimeter (Jasco, UK). All CD spectra were an average of three scans recorded at a scan speed of 100 nm min<sup>-1</sup>. Spectrum of buffer was recorded and subtracted from the spectra of DNA/metal ion mixtures. Measurements were done with in the 210-300 nm in the nitrogen atmosphere at 25 °C.

### 3.4.5 ITC

Calorimetric analysis was performed in an ITC<sub>200</sub> microcalorimeter (Microcal®) at 25 °C and at 300 rpm stirring speed to prevent foaming on the biological solution. Samples were degassed prior to titration. The sample cell was loaded with CT DNA or HSA (200 μM) and Au(III) chloride hydrate or Ga(III) nitrate hydrate solutions (4 mM) were injected into the reaction cell. The data of metal ion titration into buffer solution were subtracted after data acquisition to analyze biomacromolecule/metal ion binding parameters. Data were analyzed using MicroCal Origin 7.0 software. The data were analyzed using a one-site model by the Origin 7.0 software package supplied by MicroCal.  $\Delta G$  (Gibbs free energy) calculations were made by the following formula<sup>216</sup>:

$$\Delta G = - RT \ln K_a = \Delta H - T\Delta S \quad (2)$$

where  $T$  is the absolute temperature in Kelvin (298 K) and  $R = 8.3151 \text{ J mol}^{-1} \text{ K}^{-1}$ .

### 3.4.6 FT-IR spectroscopy

Infrared spectra were recorded on a Nicolet 6700 FT-Raman Spectrometer (Thermo-Scientific, US). Interferograms were accumulated over the spectral range of 4000–600  $\text{cm}^{-1}$  with a nominal resolution of 4  $\text{cm}^{-1}$  and 164 scans for better signal to noise ratio. Eleven point data smoothing was done by Sawatzky–Golay functionality. All the spectral measurements were performed at room temperature and ambient humidity of 45% RH. In the absence and presence of different concentrations of Au(III) chloride hydrate or Ga(III) nitrate hydrate – CT DNA (200 μM) mixtures were prepared. Final metal ion concentrations (100 and 200 μM) were used with a final HSA concentration of 250 μM. Spectra were collected after 2 h incubation of samples at room temperature with metal ion solutions and measured in duplicate. After 2 h incubation, 20 μL of

final solutions were dropped and dried on the 96-well plate supplied by instrument, and samples were dried at room temperature. The protein secondary structure was determined from the shape of the amide I band at 1600-1700  $\text{cm}^{-1}$ . The data analysis software OMNIC<sup>TM</sup> was used for FT-IR measurements, identification of peak locations, and basic modifications such as baseline and background corrections. Background corrections for H<sub>2</sub>O and CO<sub>2</sub> were carried out for each analysis. Duplicate samples were utilized in each analysis, and experiments were repeated independently for at least two times.

#### **3.4.7 Fluorescence spectroscopy**

The fluorescence measurements were performed using SpectraMax M5 Microplate Reader (Molecular Devices, USA) using a quartz cuvette with 1 cm path length. Excitation wavelength was 290 nm and emission wavelength range was 300-450 nm. Titration experiments were carried out by adding increasing concentrations (10-1,280  $\mu\text{M}$ ) of Au(III) chloride hydrate and Ga(III) nitrate hydrate solutions to HSA solution (10  $\mu\text{M}$ ).

#### **3.4.8 Cell culture and viability assay**

MCF-7 cells were maintained in 10% FBS and 1% penicillin/streptomycin (Gibco) containing DMEM (Gibco) at 37 °C under 5% CO<sub>2</sub>, and passaged twice weekly depending on the confluency of cells. The cell viability was estimated by using Alamar blue Assay. The same procedure was applied as explained in Section 2.4.9.1. Cells were seeded in 96 well-plate at a density of  $1 \times 10^4$  cells/well in 100  $\mu\text{L}$  culture medium, and then treated with different concentrations of metal salt solutions (0-1,000  $\mu\text{M}$ ) prepared in DMEM. Incubation was performed at 37 °C and 5% CO<sub>2</sub> for 24 h.

## **Chapter 4**

### **INTERACTIONS BETWEEN BIOMACROMOLECULES AND BORIC ACID OR BORON COMPOUNDS**

Part of this thesis is published in the following article<sup>199, 217</sup>; Reprinted from

“Non-intercalative, Deoxyribose Binding of Boric Acid to Calf Thymus DNA”;  
Ozdemir A., Gursacli R., Tekinay T., Biol Trace Elem Res. 2014, pp:268:74, with  
permission from Springer and “Spectroscopic evaluation of DNA-borate interactions”;  
Ozdemir A., Sarioglu O.F., Tekinay T., Biol Trace Elem Res., 2015, pp:1-8, with  
permission from Springer.

A partial content of this work is under preparation for a publication with the following  
authors: Ozdemir A., Sarioglu O.F., Tekinay T.

## 4.1 INTRODUCTION

Boron is an essential element, and required for many plant functions, including cell wall cross linking, lignin and nucleic acid biosynthesis<sup>218</sup>, sugar metabolism as well as seed production<sup>219</sup>. In humans, boron compounds play important roles in membrane signaling, reactive oxygen species removal, bone function, calcium and magnesium metabolism and hormone (*e.g.* insulin, estrogen and testosterone) regulation<sup>220</sup>. Boron atoms are capable of forming covalent bonds with several structures, such as porphyrins for photodynamic therapy<sup>221</sup>, in the same way as carbon atoms in organic compounds. The main forms of inorganic boron is boric acid  $B(OH)_3$ . Borates, the naturally occurring forms of boron, are generally found as salts in soil, aqueous environment or food and have widespread use as food preservatives, antiseptics and flame retardants, as well as in cement production and glass industry. Other sources of boron include borate mining, wood burning, sewage disposal and weathering processes. It is known that boron compounds have low toxicity, but they are considered to be toxic to the environment at very high concentrations<sup>222, 223</sup>.

In recent years, considerable academic interest has been devoted to the development of nanoscaled boron containing therapeutic and delivery agents<sup>224-226</sup>. Two boron compounds (bortezomib and tavaborole) are being used for the treatment of multiple myeloma and onychomycosis of the toenail in the market and boron based drug design will take on an increasingly important role for further development in medicinal chemistry<sup>221</sup>. Various types of boron containing agents have been investigated for biomedical applications due to the low chemical reactivity and a high resistance to enzymatic degradation of boron<sup>227</sup>. The most important clinical application of boron is based on the element's capacity to absorb neutrons, which has been used to kill

tumor cells in boron neutron capture therapy (BNCT), a non-invasive technique for the treatment of various cancers<sup>228, 229</sup>, especially brain tumors<sup>227, 230</sup> since 1950s<sup>231</sup>. Up to now, several strategies have been employed to selectively deliver boron atoms or boron derivative drugs into tumor cells<sup>232</sup> by the use of various agents, such as liposomes<sup>233, 234</sup> and nanoparticles<sup>232</sup>. Several studies have investigated the anticancer activity, growth inhibition and induction of apoptosis at higher doses<sup>235</sup> of boric acid (BA). Effectiveness of BA for hindering growth and proliferation of prostate cancer cells and breast tumor cells have already been evaluated<sup>236-237, 238</sup>. There are also several studies in the literature about the clinical potential of some borates (e.g. calcium fructoborate) and their effects on the viability of different cancer cell lines<sup>239</sup>. It has been reported that boron compounds are capable of preventing DNA damage<sup>240</sup> induced by titanium dioxide and paclitaxel. Besides the therapeutic potential of BA and its derivatives, the underlying mechanism of boron compounds on normal and pathologic tissues has not yet been established fully<sup>241-244</sup>. Therefore, the relationships between boron and biomolecules still need to be investigated in order to thoroughly understand the precise metabolic effects of BA and borates on key biomacromolecules, such as nucleic acids and to evaluate the potential of the boron containing compounds in biomedical applications.

This study investigated BA as one of the boron compound of interest, since the hydroxyl groups of BA can associate with water molecules of biological ligands. Furthermore BA can form covalent and ester bonds with biomolecules<sup>245</sup>. Two common borates which are widely utilized in industry; ulexite (ule) and colemanite (col) have been also analyzed under physiological conditions in terms of binding interactions.

It is known that most of the chemotherapeutic drugs interact with DNA of cancer cells by intercalation, inter- or intrastrand cross-linking, or binding to the N3 atom of DNA purines, thus stop proliferation and damage tumor cells. As a consequence, a deeper understanding of the basic mechanism between DNA–Boron compound interactions may allow the design of novel boron derivatives for cancer inhibition. Therefore, we used CT DNA as a model biomacromolecule in our experiments. Inorganic boron compounds can also have lethal effect if they are located within or near the cancer cell nucleus<sup>246</sup>.

HSA is the most abundant protein in the blood plasma. In addition to its direct biological functions, such as the maintenance of osmotic pressure, modulation of fluid distribution and prevention of the photodegradation of folic acid, it facilitates the biodistribution of many endogenous and exogenous compounds, including hormones, fatty acids, metals and drugs<sup>119</sup>. The potential interactions between metals and HSA have been a topic of substantial research, and their understanding is of substantial importance for the determination of the mechanism of action for metal-containing drugs<sup>247</sup>.

In this chapter, HSA and DNA binding characteristics of BA and boron compounds were investigated using several spectroscopic, calorimetric, and microscopic methods. Chemical alterations in the secondary structure of these biomacromolecules, the binding modes and binding constants have been investigated using several tools. We also addressed whether ule and col are toxic to endothelial cells.

## **4.2 RESULTS and DISCUSSION**

### **4.2.1 DNA Binding Characteristics of BA**

#### **4.2.1.1 The Effects of Interaction of BA with DNA to Its Absorbance**

The absorption maxima of free DNA is observed at 260 nm as a sigmoidal curve which results from  $\pi$ - $\pi^*$  transitions in the aromatic purine (adenine, guanine) and pyrimidine (uracil, cytosine, thymine) rings of the nucleic acids<sup>248</sup>. Changes in the UV absorption band characteristic of DNA (peak intensity or peak position) upon addition of a ligand show alterations in the DNA secondary structure<sup>228</sup>. Especially, the disruption of the hydrogen bonds between base pairs may occur when a molecule binds to DNA<sup>249, 250</sup>.

In order to understand association between BA and CT DNA, absorption spectral titration experiments were performed. Our results demonstrate that there is a molecular association between BA and CT DNA as seen in Figure 4.1. Though the absorbance change at 260 nm is negligible at lower concentrations of BA, it is increased significantly at higher concentration which may result from DNA denaturation. It is known that decrease in the intensity of maximum peak of DNA, called hyperchromism, without any shift, is related to the non-intercalative binding of a small molecule<sup>251, 252</sup>. In addition, EtBr displacement assay was used to prove non-intercalative binding between BA and CT DNA. EtBr displacement assay results suggested that BA binding to CT DNA is not intercalation because of stable fluorescence intensity of EtBr bound DNA following addition of BA (Table 4.1).

**Table 4.1** The relative fluorescence intensity ratios with respect to varying concentrations of BA.

<b>[ DNA ] / [ Boron ]</b> <b>molar ratio</b>	<b>Relative Fluorence Intensity (%)</b> <b>[ DNA ] / [ BA ]</b>
<b>1 : 0</b>	$100 \pm 4.1$
<b>1 : 1</b>	$98 \pm 3.5$
<b>1 : 5</b>	$97 \pm 1.2$
<b>1 : 20</b>	$95 \pm 2.3$

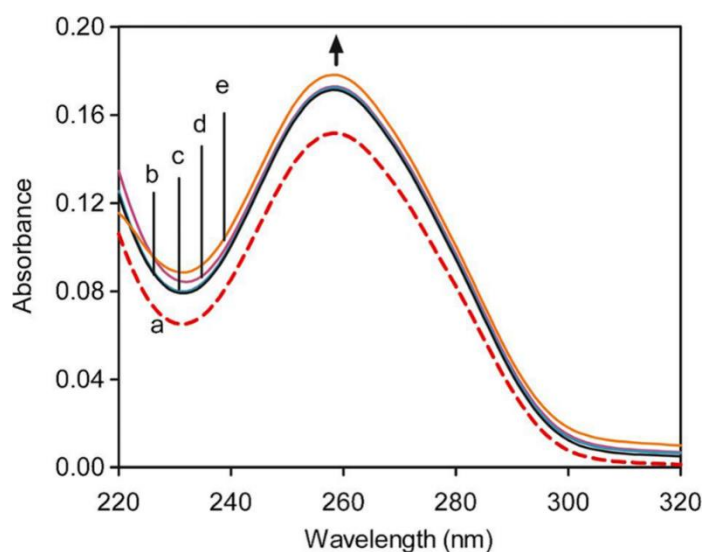


**Figure 4.1** UV–Vis spectra of CT DNA in 0.01 M TE buffer (pH 8.0) in the presence and absence of BA. Total volume was constant. Arrow shows absorbance change upon increasing concentrations of BA. **a)** Free CT DNA (0.01 mM) and DNA–BA complexes with varying DNA/BA ratios **b)** [1:1], **c)** [1:5], **d)** [1:10], and **e)** [1:50].

#### 4.2.1.2 Investigation of Conformational Transition of DNA

Isomerizations among distinct conformational states of DNA can be clearly observed on CD spectra. Unmodified double helical DNA, right-handed B-DNA, has two distinctive CD bands: a positive band at 277 nm and a negative band around 247 nm due to the base stacking of DNA nucleotides<sup>191</sup>. Bands of free CT DNA demonstrate a classical Gaussian shape, which is characteristic of the B-DNA conformation (Figure 4.2a)<sup>253</sup>. Changes in the position of 277 nm band is the indicator of conformational transition from B to A DNA<sup>254</sup>. The intensity of both positive and negative peaks decreased gradually without a significant shifts after BA-DNA complex formation. CD results revealed that the binding of BA to CT DNA may not cause conformational change in DNA structure. Figure 4.2b and 4.2c show quantification of alterations in the band intensities of CD spectra upon the addition of BA. It is known that reduction in the amplitude of the positive CD band around 280 nm is indicative of DNA denaturation<sup>255</sup>. Maybe, the observed decrease in that band in our results is due to degradation of nucleotides which is consistent with our UV–Vis spectroscopy data.

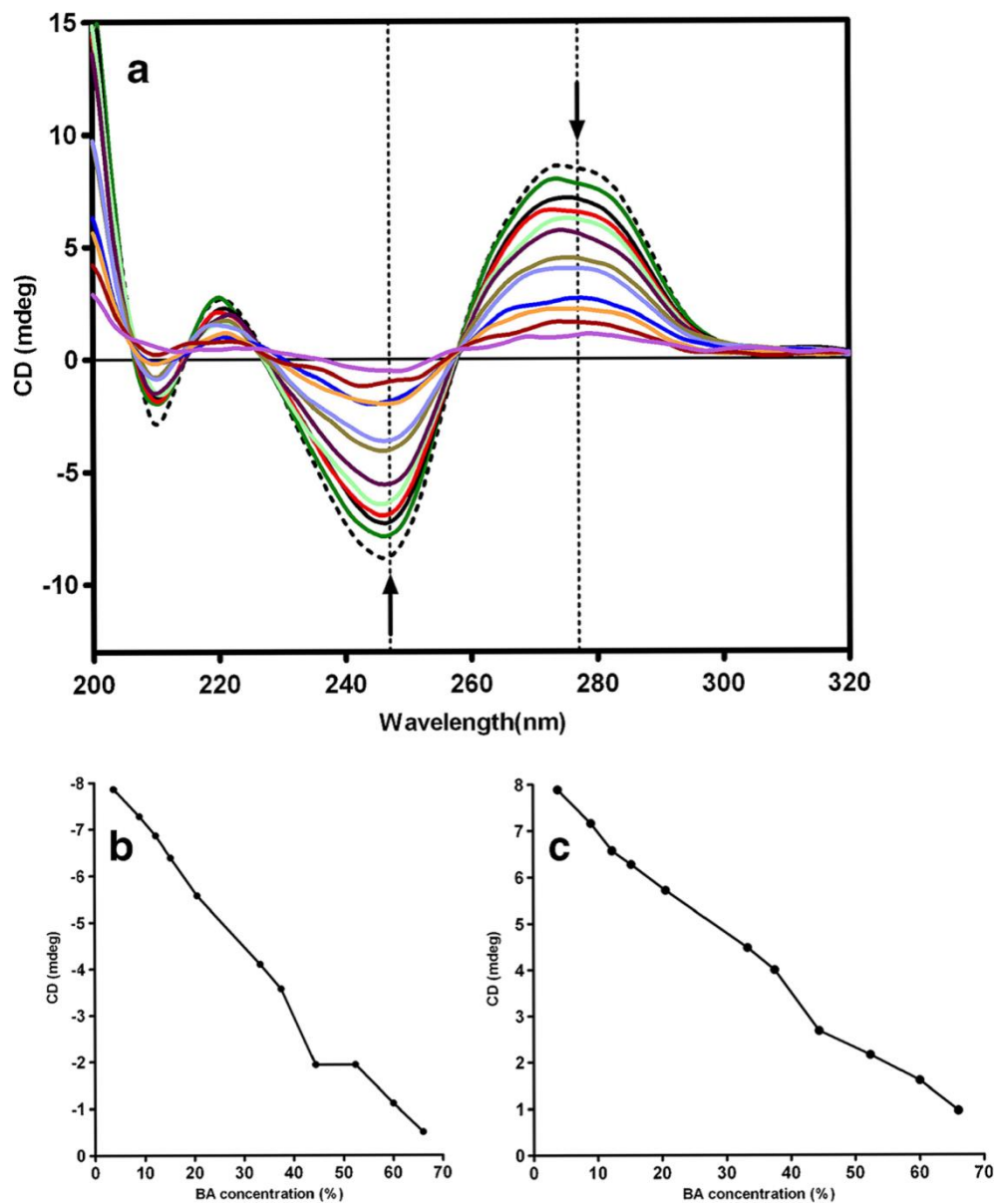


**Figure 4.2** (a) CD spectra of free DNA and BA- DNA mixtures in 0.01 M Tris-HCl buffer (pH 7.5). Arrows show the direction of changes in CD spectrum with increasing BA concentration. (b) Alterations in the amplitude of CD bands at 247 nm and (c) at 277 nm following BA addition.

#### 4.2.1.3 Morphological Investigation of DNA-BA Interactions

TEM is an important analytical tool in the field of material science and molecular biology for structure characterization. TEM is based on irradiation of a sample with electron beam which generally has 60-160 keV energy emitted from an electron gun under the vacuum. Depending on the electron diffraction contrast and distribution of electron density of sample, an image can be obtained on the fluorescent screen. Here, we analyzed the general morphology of BA–DNA complexes by TEM. Structures of free CT DNA and free BA are shown in Figure 4.3a, b. The observed irregular structures of free DNA may result from sheared DNA stock (Figure 4.3a). Free BA clusters form large aggregates as seen in Figure 4.3b. When DNA was incubated with BA, aggregates were clearly observed (Figure 4.3c). Interestingly, BA molecules were homogeneously dispersed and had regular shapes with diameters in the range of 10–15 nm. BA molecules probably bound to the exposed surfaces of double stranded DNA clusters.

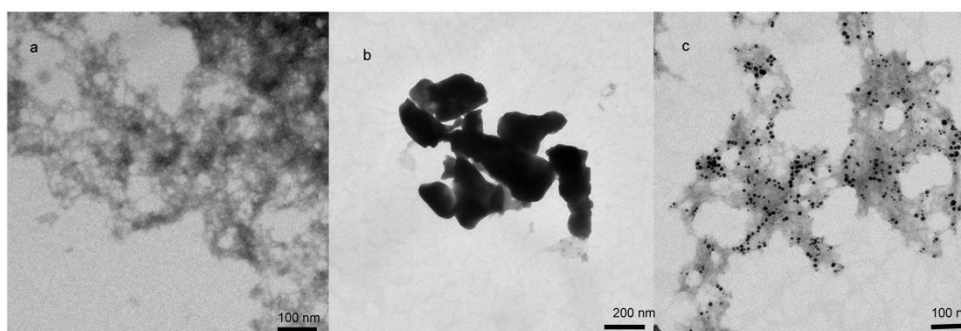


**Figure 4.3** TEM observation of **a)** 0.1 mM free CT DNA, **b)** 1 mM BA, and **c)** 0.1 mM CT DNA + 1 mM BA mixture. All samples were prepared in double distilled water and negatively stained with 2% uranyl acetate.

#### 4.2.1.4 Effects of BA Treatment on FT-IR Spectra of DNA

The binding mode of BA to CT DNA was evaluated via FT-IR spectroscopy. We compared the FT-IR spectra of DNA in the presence and absence of BA with varying concentrations. The spectra in the 700–1800  $\text{cm}^{-1}$  region are presented in Figure 4.4. The marker bands of DNA and their shifts are tabulated in Table 4.2. The peaks at 1715, 1663, 1604, and 1496  $\text{cm}^{-1}$  correspond to the vibrations of guanine (G), thymine (T), adenine (A), and cytosine (C), respectively<sup>191</sup>. After the addition of 1 mM BA to the DNA solution, the cytosine band at 1496  $\text{cm}^{-1}$  shifts to 1499  $\text{cm}^{-1}$ . A number of peaks around 1400–1500  $\text{cm}^{-1}$  disappeared by binding of BA (Figure 4.4). We observed that the overall spectral features for nitrogenous bases are similar to free DNA, which rule out the intercalation of BA to DNA strands. Peaks at 1231 and 1082  $\text{cm}^{-1}$  are denoted to phosphate asymmetric and symmetric stretching, respectively, and are commonly used to distinguish the binding modes and conformational changes. With the addition of increasing concentrations of BA, the band at 1231  $\text{cm}^{-1}$  gradually shifted to 1239  $\text{cm}^{-1}$ . The changes in this position may be attributed to partial perturbation in native B conformation of DNA. FT-IR outcomes are consistent with our CD spectroscopy results. In addition, sugar band at 1055  $\text{cm}^{-1}$  shifts to 1049 or 1053  $\text{cm}^{-1}$  in the presence of high concentration of BA. There is another B conformation peak at 825  $\text{cm}^{-1}$  which slightly shifts to 822, 824, and 821  $\text{cm}^{-1}$  in 0.25, 0.5, and 1 mM BA–DNA mixtures, respectively. It is known that the band in 821  $\text{cm}^{-1}$  is symmetric stretching of B(4)-O<sup>256</sup>. Therefore, the observed shifts in B conformation marker of DNA may result from the higher vibration of B(4)-O bond at high concentrations of BA. Our data indicated that the main binding site of BA could be deoxyribose compared to other regions, because a major shift was observed from 891

to  $881\text{ cm}^{-1}$  which attribute to deoxyribose band upon the addition of BA. In aqueous conditions, BA can form ester bonds with the hydroxyl groups of the sugars. For example; the sugar diacid disodium saccharate (glucarate) and BA form complex in 2:1 ratio in aqueous solution<sup>257</sup>. The interaction between sugar and BA may not limited to function on DNA. It may also affect its cellular uptake through the co-transport mechanism via a sugar transporter like calcium fructoborate<sup>239</sup>.

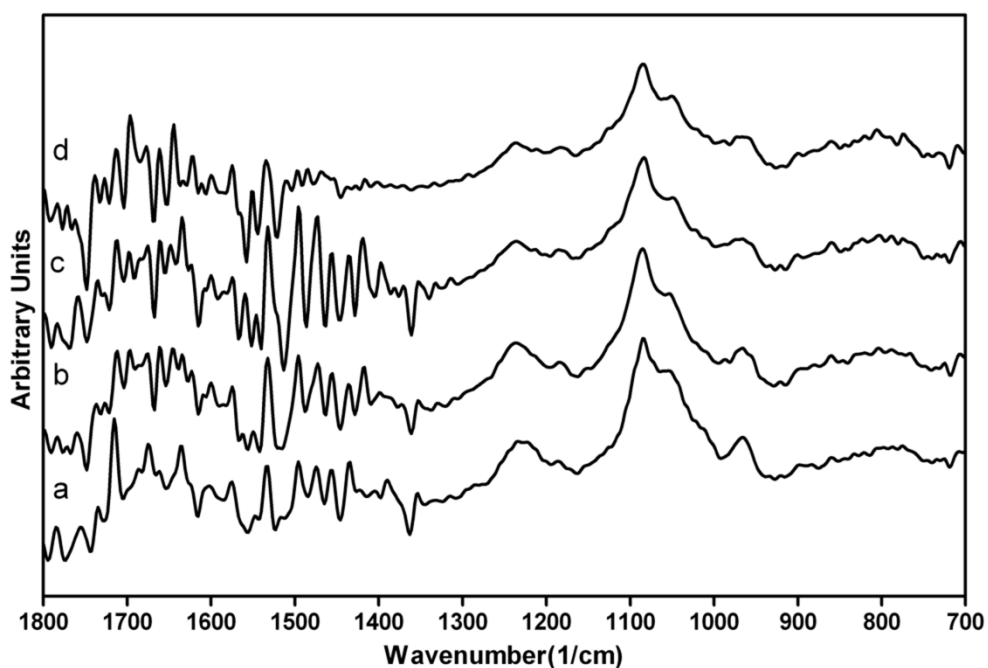


**Figure 4.4** FT-IR spectra of DNA-BA mixtures in the region of  $700\text{-}1800\text{ cm}^{-1}$ . **a)** free CT DNA (1 mg/mL), **b)** DNA + 0.25 mM BA, **c)** DNA + 0.5 mM BA, **d)** DNA + 1 mM BA.

**Table 4.2** Peak positions and spectral shifts of the free CT DNA and CT DNA–BA complex at different molar ratios. Concentration of DNA was kept constant (1 mM) for all samples.

DNA band assignments	Free DNA (cm <sup>-1</sup> )	DNA–0.25 mM BA (cm <sup>-1</sup> )	DNA–0.5 mM BA (cm <sup>-1</sup> )	DNA–1 mM BA (cm <sup>-1</sup> )
Guanine	1715	0	0	0
Thymine	1663	0	-1	0
Adenine	1604	+2	+1	-2
Cytosine	1496	+1	0	+3
Phosphate asymmetric	1231	+7	+8	+6
Phosphate symmetric	1084	+1	0	0
Sugar phosphate	1055	0	-6	-2
Backbone marker	967	0	0	+2
Deoxyribose	891	-10	-10	-9
B-conformation marker	825	-3	-1	-3

#### 4.2.1.5 Analysis of Thermodynamics of BA-DNA Binding

ITC is a powerful tool for direct determination of thermodynamic parameters ( $\Delta H$ ,  $\Delta G$ , and  $\Delta S$ ) associated with binding reactions, stoichiometry of interaction between two molecules ( $n$ ), and binding affinity ( $K_a$ )<sup>258</sup>. Multiple reports are available in literature about the ITC-based quantitative measurements of interactions between biological macromolecules, such as proteins<sup>259-264</sup> or DNA<sup>265-268</sup> and metal ions. In our study, thermodynamics of BA binding to CT DNA was analyzed via ITC. 5 mM BA in double-distilled water was titrated into 0.5 mM CT DNA; the thermogram of the reaction is shown in Figure 4.5. According to binding isotherm, the number of binding sites for the BA–DNA complex formation is 0.2. Because the BA–DNA interactions do not involve the formation of a 1:1 bound complex, a sigmoidal plot could not be fully fitted with the one-site binding model, but a partial fit has been obtained. ITC data showed that the rapid saturation of the BA–DNA complex resulted from the high initial molarity of BA. Negative enthalpy change in calories per mole was found to be  $-920.6 (\pm 1.44)$ , which revealed the binding reaction is exothermic, and the affinity constant  $K_a$  was found to be  $9.54 \times 10^4$ . The obtained thermodynamic parameters revealed that the interaction between BA and CT DNA is enthalpy driven rather than entropy.

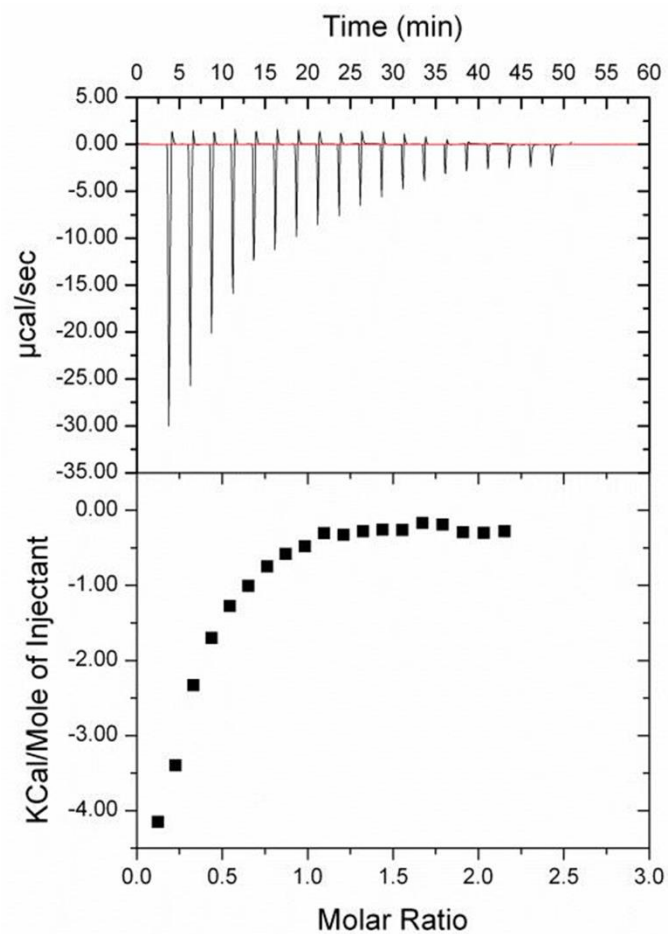


**Figure 4.5** ITC data for the titration of BA (5 mM) into CT DNA (0.5 mM) at 25 °C. Top panel demonstrates the differential power of the experiment. Bottom panel represents integrated heat change after each injection of BA.

## 4.2.2 DNA Binding Characteristics of Boron Compounds

### 4.2.2.1 Spectroscopic Confirmation of the Interaction of Borates with DNA

The UV absorption of a biomacromolecule can be used to understand the interactions between this molecule and possible targeting ligand. It is known that hyperchromism of the absorption band of helical DNA at 260 nm after the binding of a ligand may indicate the presence of a strong intercalative binding (i.e. insertion between the base pairs) between that ligand and DNA<sup>182</sup>. On the other hand, hypochromisms are generally associated with charge-transfer interactions<sup>269</sup>. The reverse trend is true if you are interested in the changes of maximum absorption peak of the ligand: Hypochromisms and red-shifts result from intercalative binding, whereas hyperchromism is associated with an electrostatic mode of interaction<sup>270</sup>.

The chemical structures of ule and col were demonstrated in Figure 4.6. Initially, the mode of binding between borates and DNA was investigated by UV-Vis spectroscopy. Figure 4.7a and 4.7b show the titration of varying amounts of ule or col into constant concentration of CT DNA, respectively. The absorbance peak around 258 nm showed slight hyperchromic shifts following the addition of borate compounds. This hyperchromicity is observed to be more pronounced (~20%) for col as compared with ule (10%). Also, same experiment was performed at a constant concentration of borates and varying concentrations of CT DNA as shown in Figure 4.8a and 4.8b. The maximum UV absorbance of both boron compounds were observed at 503 nm. Although ule samples demonstrated concentration-dependent hyperchromism with a slight blue-shift following DNA binding, col samples showed a gradual hypochromism at the same region. The binding of ule to CT DNA may depend on electrostatic

association between the negatively-charged phosphate backbone and positively-charged metal cations present in the borate structure<sup>112, 270</sup>. However, hypochromic effect of col on CT DNA may indicate that col has a stronger affinity to CT DNA and potentially interacts with the double helix through intercalative binding.

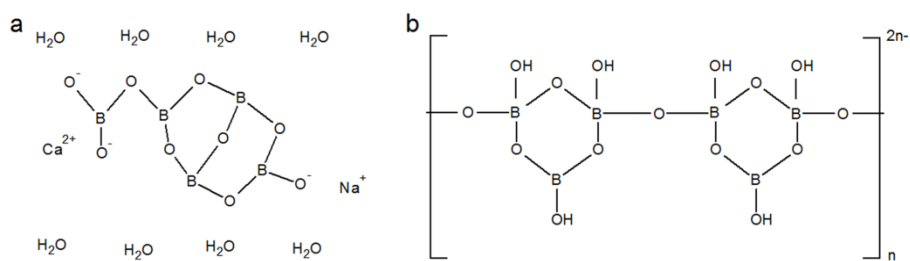


**Figure 4.6** Chemical structures of (a) ule and (b) col used in study.

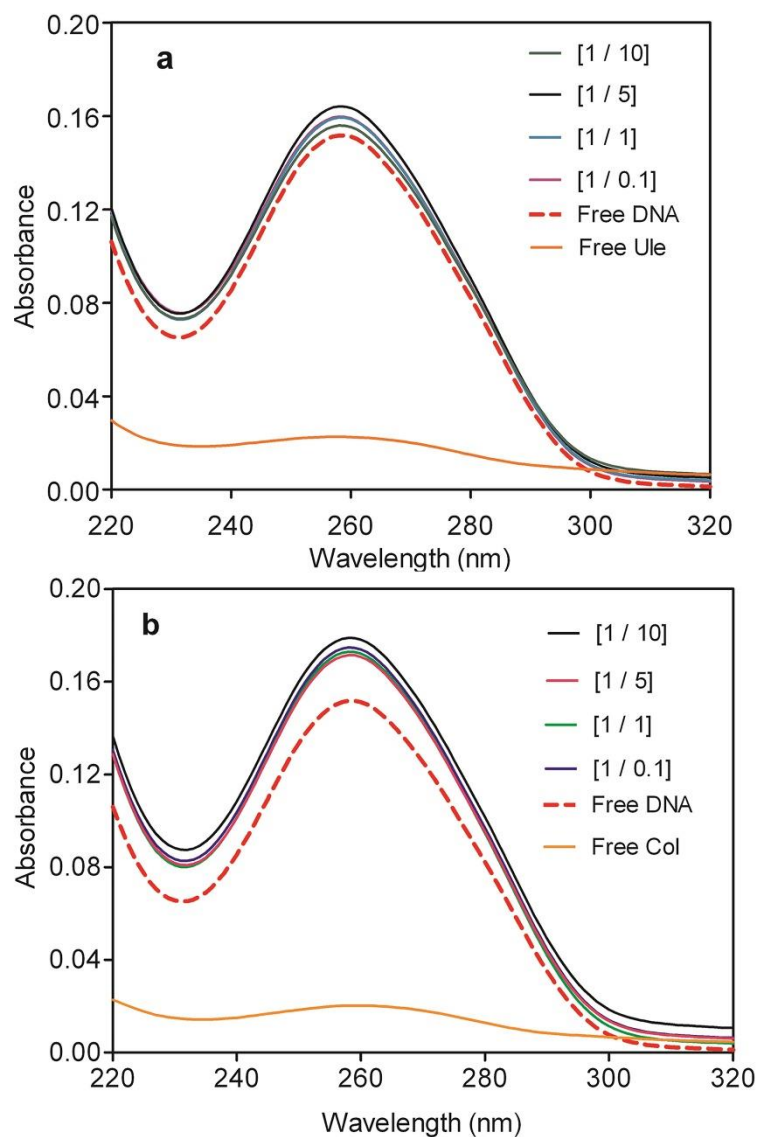


**Figure 4.7** UV-Vis spectra of CT DNA (0.01 mM) in the presence (solid line) and absence (dashed line) of varying concentrations of (a) ule and (b) col at the following ratios: [DNA/borate] = 0:1, 1:0.1, 1:1, 1:5, 1:10.

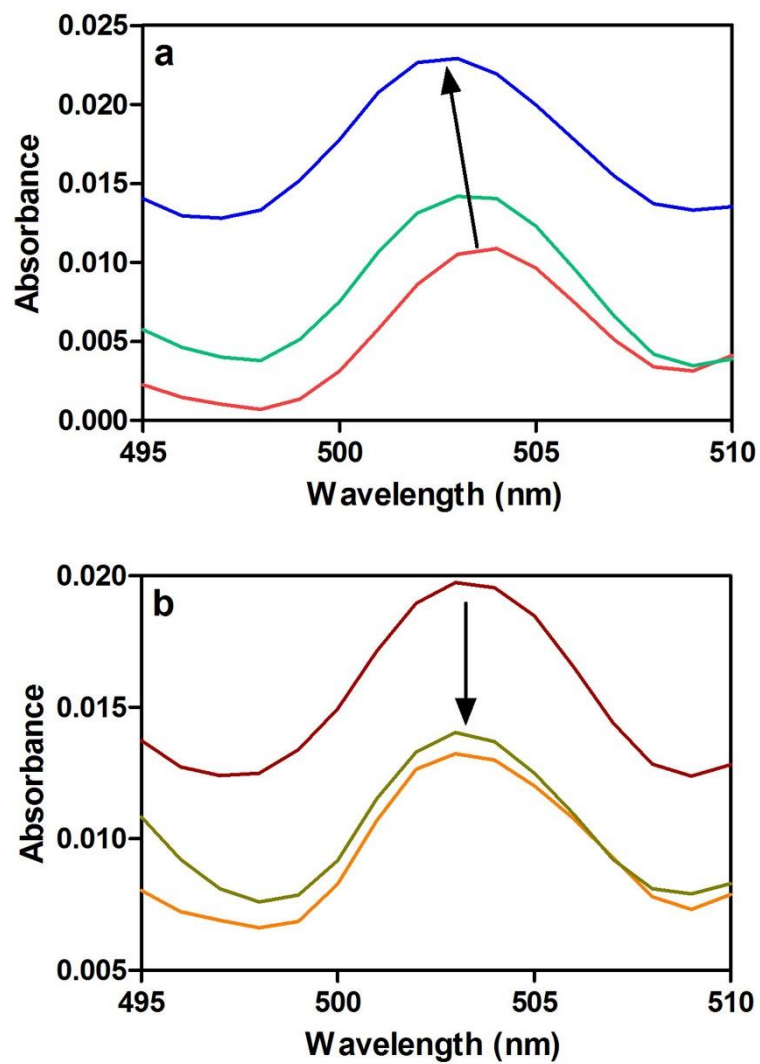


**Figure 4.8** UV-Vis spectra of (a) ule (0.1 mM) and (b) col (0.1 mM) in the presence and absence of different concentrations of CT DNA at the following ratios: [DNA/borate] = 0:1, 1:1, 2:1. The arrow indicates the spectral sequence with increasing DNA content.

#### **4.2.2.2 Competitive DNA Binding Between EtBr and Borates**

EtBr is a well-known intercalator and widespread use of it in anticancer drug research for the investigation of the intercalative capabilities of therapeutic agents is continuing<sup>271</sup>. An intercalator molecule can displace this cationic dye already present between the DNA strands which results in decrease in fluorescence quenching of EtBr-bound DNA and yields information about the binding mode of the molecule in question<sup>187</sup>. Displacement of EtBr from DNA after treatment with borates was not considerable in our experiment (Table 4.3). It has been reported that a competing DNA intercalator reduces the fluorescence of EtBr-bound DNA by about 50%, because of the lower fluorescence intensity associated with free EtBr molecules that are displaced from their original positions by the intercalator<sup>272</sup>. In our case, the addition of borates causes slight decreases in fluorescence intensity (by 10% and 11% for ule and col, respectively). Borates have comparable value to some groove binders<sup>272</sup>. Furthermore, the relationship between col and CT DNA is probably stronger than ule due to the observed more prominent fluorescence quenching at higher concentrations. The absence of a significant displacement of EtBr suggested non-intercalative binding between CT DNA and borates.

**Table 4.3** EtBr displacement assay results showing the fluorescence intensity changes with respect to different concentrations of borates.

[ DNA ] / [ Borate ]	Relative Fluorence Intensity ( % )	
molar ratio	[ DNA ] / [ Ule ]	[ DNA ] / [ Col ]
1:0	100 ± 4.1	100 ± 4.1
1:1	96 ± 2.7	96 ± 3.3
1:5	95 ± 3.9	90 ± 1.8
1:10	90 ± 1.6	89 ± 2.5

#### **4.2.2.3 Investigation of Effects of Borate on DNA Damage**

DNA cleavage induced by a molecule can be monitored via agarose electrophoresis analysis. The accumulation of metal ions around the DNA helix creates oxygen or hydroxide radicals which results in endonucleolytic cleavage of DNA<sup>273</sup>. It is known that intercalative or electrostatic binding interactions are capable of decreasing the mobility of DNA<sup>274</sup>. We performed agarose gel electrophoresis with borate-bound CT-DNA and borate-bound plasmid DNA to understand whether borates change the integrity of DNA (Figure 4.9). The migration of CT-DNA and plasmid DNA bands were examined in the presence of and absence of borates in aqueous buffer solution. It has been reported that relaxation of the supercoiled circular form of pUC19 plasmid DNA results in nicked circular and/or linear forms which is observed as retardation of strands. With the increasing concentrations of borates, the fragmentation of both col and ule added groups were comparable with control (non-borate treated) DNA, suggesting that both CT DNA and plasmid DNA do not cleaved despite interacting with borates. The lack of DNA cleavage activity even at higher concentrations of ule and col also indicated that the borates prefer a non-intercalative mode of binding and do not disrupt the structure of DNA. Agarose gel electrophoresis data are consistent with our EtBr displacement assay results, as the borates were also unable to replace a known intercalator from the structure of DNA.

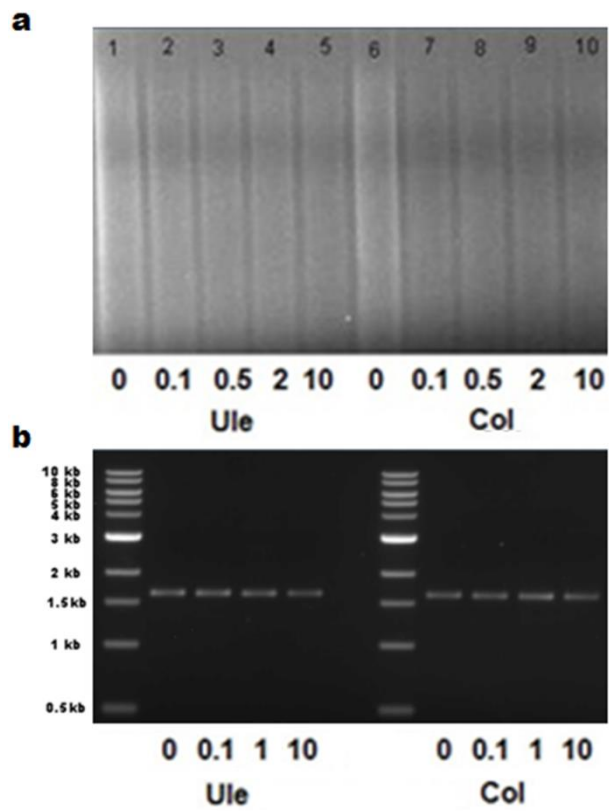


**Figure 4.9** Gel electrophoresis diagram showing bands of **a)** CT DNA (50 ng/ $\mu$ L) and **b)** pUC19 plasmid DNA (11 ng/ $\mu$ L) in the presence and absence of varying concentrations of borates (0, 0.1, 0.5, 2, 10 mM; and 0, 0.1, 1, 10 mM, respectively).

#### 4.2.2.4 Analysis of Effects of Borates on DNA Conformation

B-DNA displays two positive peaks at 220 and 275 nm, and a negative peak at 245 nm<sup>189</sup>. It is known that the peak around 275 nm and 245 nm are attributed to base stacking and the polynucleotide helicity of DNA, respectively<sup>275</sup>. Additionally, a red shift at 220 nm and an intensity increase at 275 nm peaks are some of the characteristics for B to A conformational change<sup>191</sup>. CD spectra of CT-DNA in the presence of increasing concentrations of boron compounds were recorded in order to explore the effects of borates on the secondary structure of CT DNA. Figure 4.10a and Figure 4.10b indicated that the association between borates and CT DNA causes a reduction in the intensities of CD values at 245 nm and 275 nm, and no consistent change at 220 nm was observed. CD studies showed that the right-handed helicity of B-DNA may be modified<sup>275</sup> with slight changes in the base stacking interactions. There was not B to A conformational transition because the expected peak shift in the spectra and increase in the intensity at 275 nm for both samples were not observed in our CD results. Although an intercalator is known to increase the intensities of both positive and negative bands, groove binders show less or no perturbation on the helicity and base stacking bands of DNA<sup>192</sup>. Importantly, the lack of any considerable alteration in the intensities of positive and negative peaks following borate treatment suggested that ule and col could bind to CT DNA through non-intercalative interactions (e.g. groove binding, electrostatic interactions). Moreover, helicity of B-DNA could be modified without a major change in the confirmation of CT DNA upon binding of ule and col.

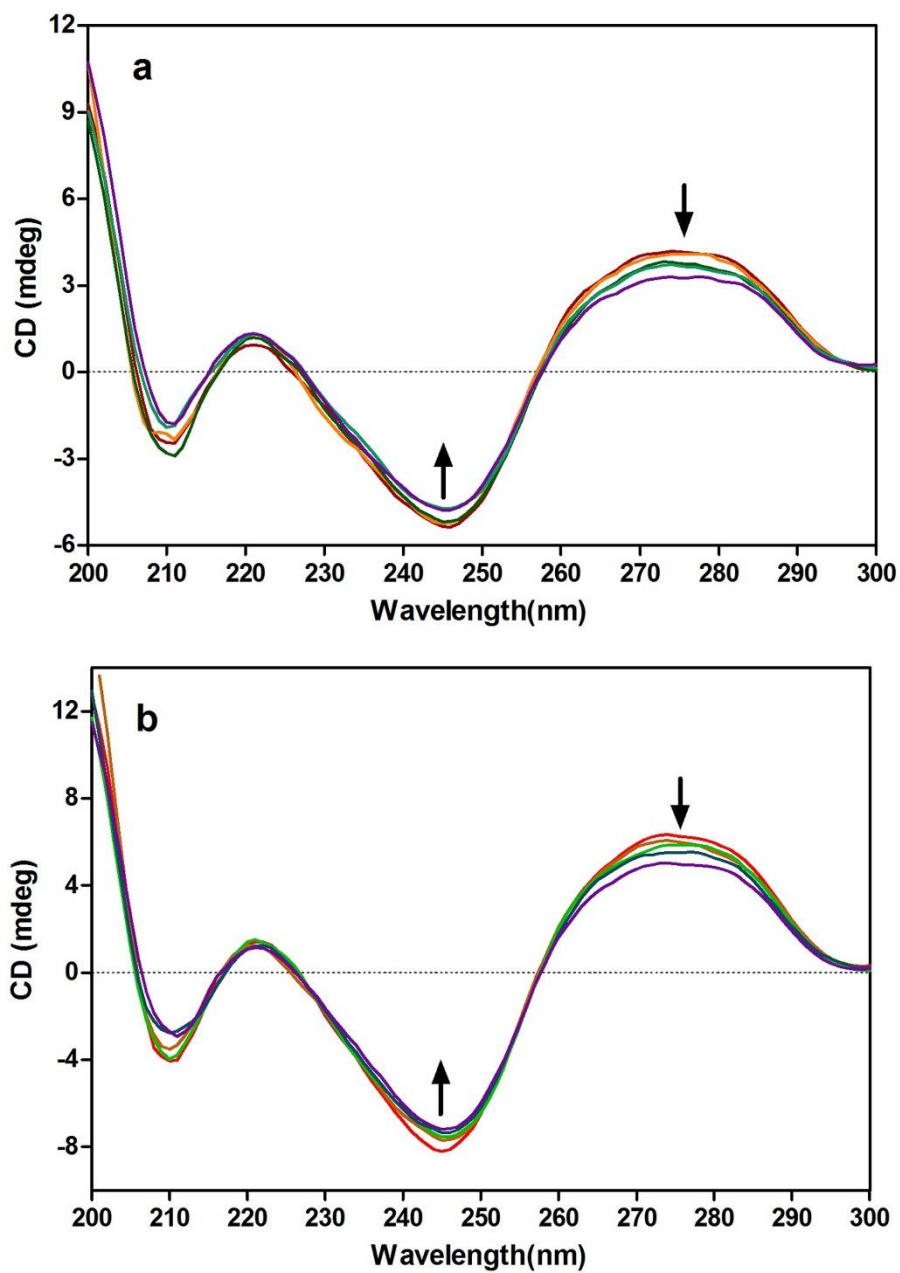


**Figure 4.10** CD spectra of CT-DNA (0.2 mM) in the presence of (a) ule and (b) col at the following ratios: [borate/DNA] = 0:1, 1:8, 1:4, 1:2, 1:1. Arrows show the spectral changes with respect to increasing concentrations of borates.

#### 4.2.2.5 Structural Analysis of DNA-Borate Binding

FT-IR spectroscopy is a nondestructive and well established tool for the determination of chemical bonds and their changes in terms of angle and structure following the binding of another molecule. Each molecule has characteristic absorption bands when exposed to IR radiation. The most sensitive spectral region to the secondary structural components of DNA is observed in the region of 1800-700  $\text{cm}^{-1}$  which derives from in plane double bond vibrations of the bases, vibrations of the glycosidic linkage between a DNA base and its sugar, antisymmetric and symmetric phosphate vibrations and phosphate-sugar backbone vibrations<sup>276</sup>. There are also specific marker bands sensitive to conformational changes between A, B and Z geometries depending on environmental conditions or binding of a molecule<sup>276</sup>.

The IR spectrum of the free CT DNA and its complexes with ule and col was demonstrated in Figure 4.11 and 4.12. All peak assignments of DNA were made in accordance with the literature<sup>277</sup>. Bands near 1715  $\text{cm}^{-1}$  are assigned to the in-plane vibrations of guanine stretching, while the band at 1663  $\text{cm}^{-1}$  is attributed to thymine stretching vibrations. The components centered at 1604  $\text{cm}^{-1}$  and 1489  $\text{cm}^{-1}$  have been assigned to the ring stretching vibrations of adenine and cytosine, respectively<sup>278</sup>. No major shifts were observed in peaks associated with DNA bases for borate concentrations of up to 2 mM, but the cytosine-associated band at 1487  $\text{cm}^{-1}$  was enhanced in a concentration-dependent manner in the difference spectra of borate/DNA complexes (Figure 4.13). Higher concentrations of ule and col were observed to slightly disrupt base vibrations, resulting in 1-2  $\text{cm}^{-1}$  shifts. The presence of these shifts is due to increased availability to alkaline earth cation ( $\text{Ca}^{+2}$ ) or to alkali metal ion ( $\text{Na}^{+1}$ ) that are found in the chemical structures of the borates, and these ions

are capable of binding DNA bases via electrostatic interactions or indirectly affect purine and pyrimidine bases. In addition, the effects of these ions on thermal stability and secondary structure of CT DNA were already discussed elsewhere<sup>279, 280</sup>. Phosphate asymmetric stretching of DNA is usually associated with the IR band at 1225 cm<sup>-1</sup> and showed an upward shift to 1240 cm<sup>-1</sup> following the binding of ule and col. The phosphate symmetric stretching band at 1087 cm<sup>-1</sup> shifted to 1095 cm<sup>-1</sup> following ule binding and association between col and CT DNA resulted in major shifts at these bands (11-13 cm<sup>-1</sup>). We also observed large shifts in the locations and intensities of 1225 cm<sup>-1</sup> and 1087 cm<sup>-1</sup> peaks, which are associated with asymmetric and symmetric phosphate stretching in the difference spectra of borate-bound DNA. The band that belongs to DNA backbone at 967 cm<sup>-1</sup> shifted to 965-977 cm<sup>-1</sup> in the presence of ule, and displayed 1-2 cm<sup>-1</sup> upward shifts following the addition of col. Also, the binding of borate compounds to CT DNA changed the bands attributed to the phosphate backbone, which can be seen in the difference spectra of borate/DNA complexes. Second-derivative analysis of the FT-IR spectra showed various considerable shifts and intensity changes of the symmetric phosphate peaks of borate/CT-DNA complexes, especially at higher concentrations of both ule and col (Figure 4.14) which may derive from electrostatic interactions of positively-charged ions in the structures of the borates and the negatively charged phosphate groups of DNA. Deoxyribose sugar vibrations band that is found at 1055 cm<sup>-1</sup> is associated with C=O and C-C stretching within the sugar structure. Sugar phosphate vibrations band was observed at 967 cm<sup>-1</sup> in the spectrum of free CT-DNA. The intensity of these bands reduced significantly, especially at higher concentration of borates as shown in Figure 5.8. Minor shifts in the deoxyribose sugar vibrations (~3 cm<sup>-1</sup>) of borate-bound

CT DNA were also presented. The peak at  $825\text{ cm}^{-1}$  is a B-DNA conformation marker, and although binding of ule did not alter the position of this band, binding of col resulted in  $1\text{-}2\text{ cm}^{-1}$  shift in the band. It is known that interaction of an agent with DNA backbone phosphates changes the locations and intensities of  $\text{-PO}_2$  bands. Our FT-IR study revealed that borates could bind externally to the sugar-phosphate backbone of the CT-DNA double helix. Furthermore, the general lack of base-related peak shifts is in line with our CD results, and supports a non-intercalative binding of borates to CT DNA.

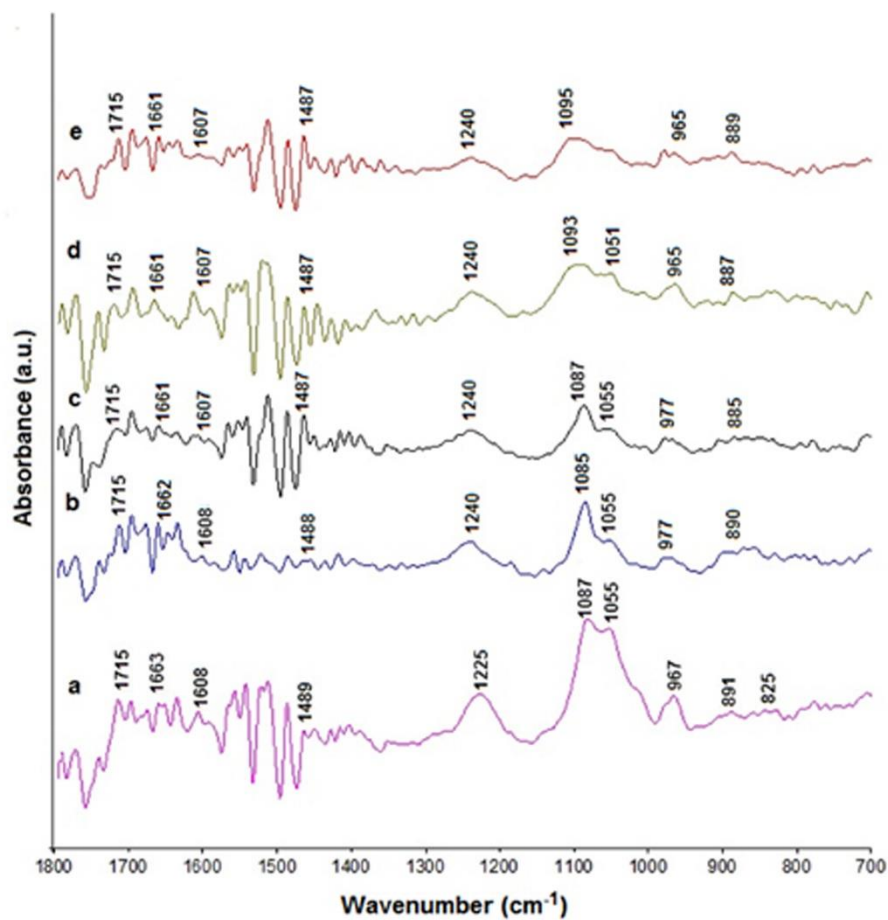


**Figure 4.11** FT-IR spectra of CT DNA-ule mixtures at different concentrations of borates. (a-e): **a)** free CT DNA (1 mg/mL) **b)** CT DNA (1 mg/mL) + borate (0.1 mM) **c)** CT DNA (1 mg/mL) + borate (0.5 mM) **d)** CT DNA (1 mg/mL) + borate (1 mM) **e)** CT DNA (1 mg/mL) + borate (2 mM) in the spectral region of 1800-700  $\text{cm}^{-1}$ .

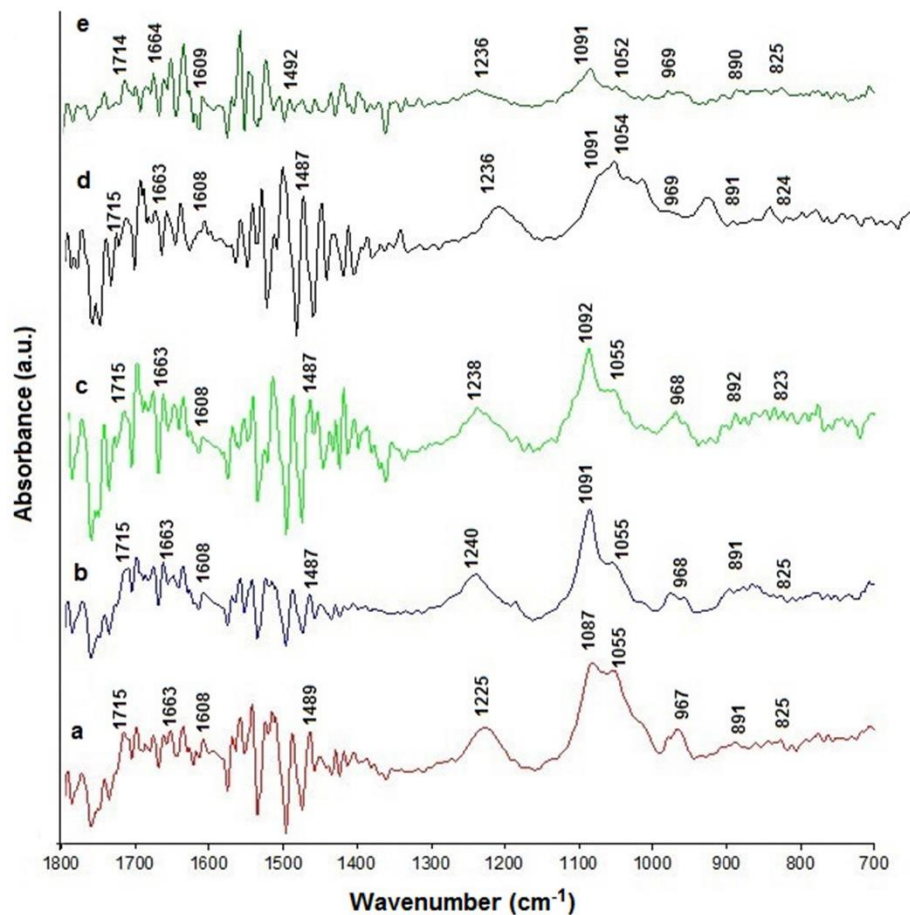


**Figure 4.12** FT-IR spectra of CT DNA-col mixtures at different concentrations of borates. (a-e): **a)** free CT DNA (1 mg/mL) **b)** CT DNA (1 mg/mL) + borate (0.1 mM) **c)** CT DNA (1 mg/mL) + borate (0.5 mM) **d)** CT DNA (1 mg/mL) + borate (1 mM) **e)** CT DNA (1 mg/mL) + borate (2 mM) in the spectral region of 1800-700 cm<sup>-1</sup>.

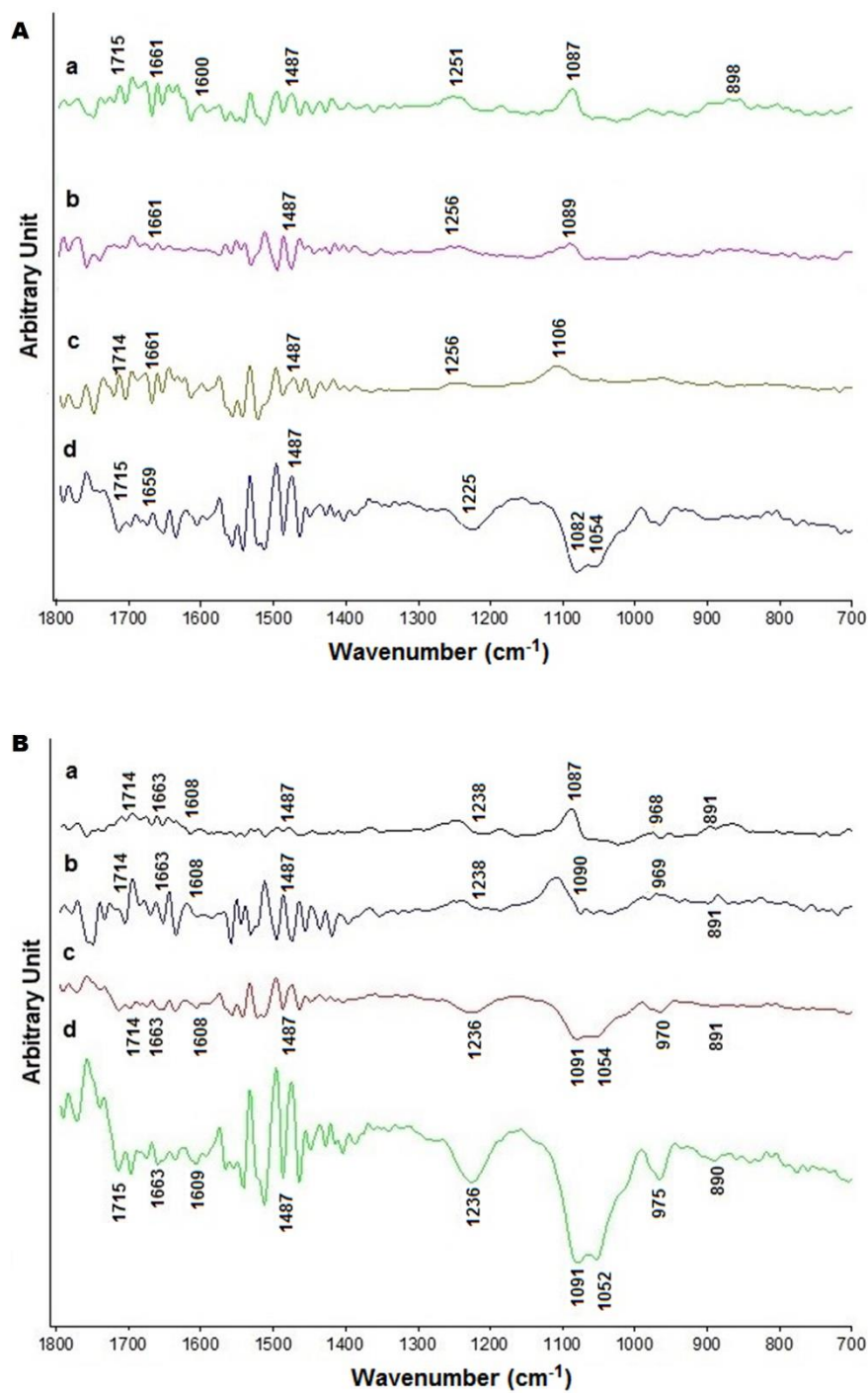


**Figure 4.13** FT-IR difference spectra of (A) CT DNA-ule mixtures and (B) CT DNA-col mixtures within the spectral region of 1800-700  $\text{cm}^{-1}$ . (a-d): **a**) CT DNA (1 mg/mL) + borate (0.1 mM) **b**) CT DNA (1 mg/mL) + borate (0.5 mM) **c**) CT DNA (1 mg/mL) + borate (1 mM) **d**) CT DNA (1 mg/mL) + borate (2 mM).

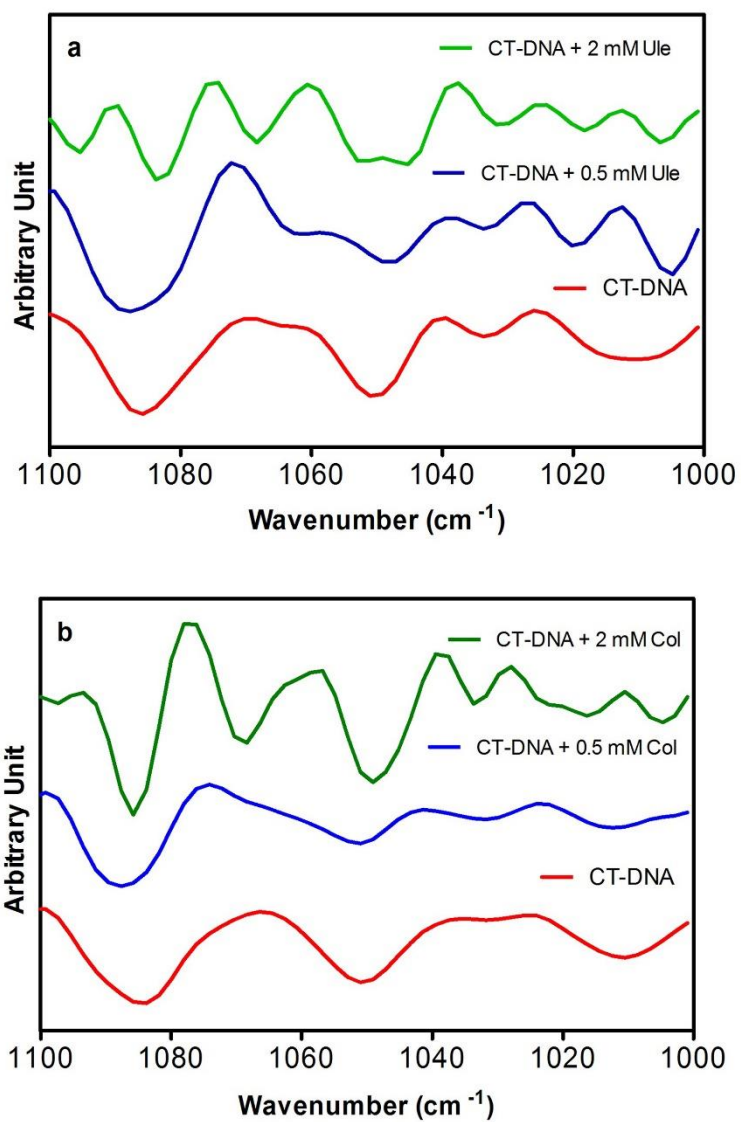


**Figure 4.14** FT-IR second-derivative spectra of **a)** CT DNA-ule mixtures and **b)** CT DNA-col mixtures within the spectral region of 1100-1000 cm<sup>-1</sup>.

## 4.2.3 HSA Binding Characteristics of Boron Compounds

### 4.2.3.1 Binding Studies Using UV-Vis Spectra

UV-Vis spectra of HSA with and without boron compounds are shown in Figure 4.15. HSA displays a characteristic absorbance peak at 278 nm, due to the  $\pi \rightarrow \pi^*$  transitions of aromatic amino acids. After the addition of increasing concentrations of ule, 39% increase was observed in the intensity of 278 nm absorbance peak, without any significant shifts. HSA-col mixture behaves similarly, however the increase in the intensity of 278 nm absorption peak for the maximum col concentration was 65%. Our data indicate that boron compounds and HSA are capable of interacting, and that Trp residues, which are primarily responsible for the 278 nm peak, are potential sites of interaction.

It is known that HSA is a transporter for  $\text{Ca}^{2+}$  ions in blood<sup>281</sup>. Ule and col include calcium in their structure which may affect binding and affinity of these borates, but there is no specific binding site or motif for Ca on the HSA. Studies revealed that Ca weakly and unspecifically binds to the serum protein and probably through the multiple carboxylates present on the surface of serum protein. Therefore; the contribution of Ca to the binding of borates are not significant<sup>281</sup>.

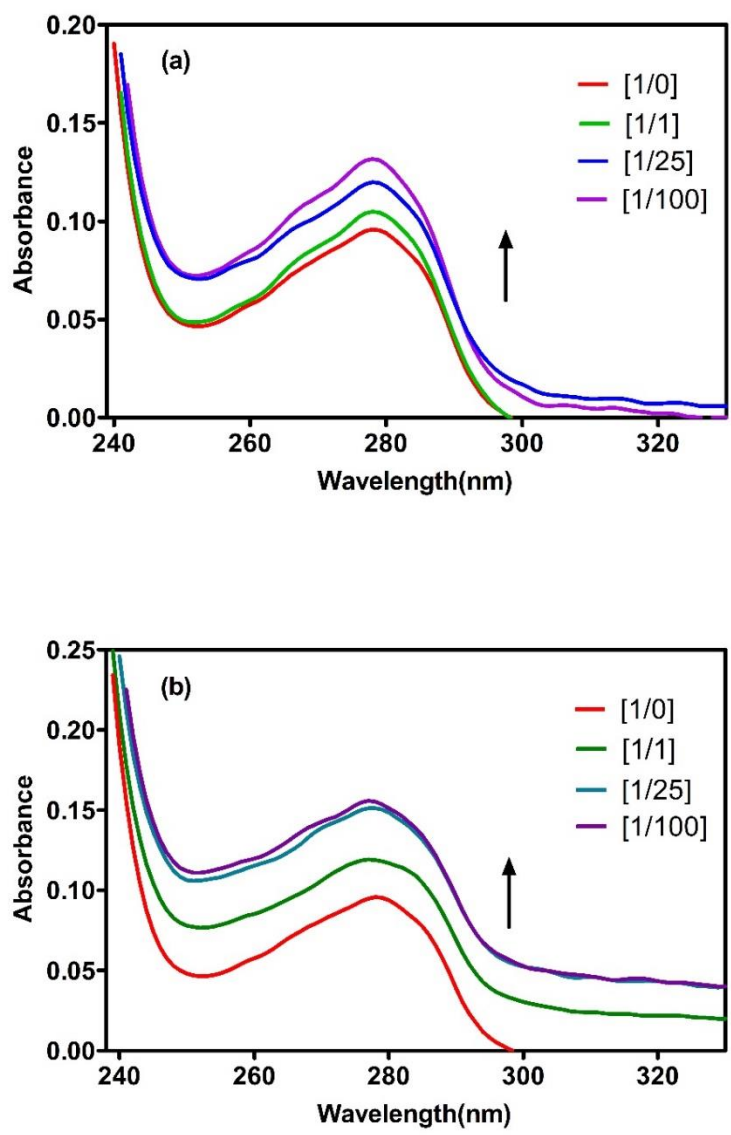


**Figure 4.15** UV-Vis spectra of free HSA and different molar ratios of HSA-boron compound complexes in 10 mM Tris-HCl buffer (pH 7.4); **a**) [HSA:ule], **b**) [HSA:col]. Protein concentration was kept constant at 0.01 mM in all samples. *Arrows* show the absorbance change following the addition of increasing concentrations of boron compounds.

#### 4.2.3.2 Fluorescence Quenching of HSA by Boron Compounds

Fluorescence spectroscopy is a useful method for exploring the interactions between a ligand molecule and a serum protein. In the 300-500 nm range, only the Trp-214 residue dominates the fluorescence of HSA. To further understand the effect of boron compounds on HSA, fluorescence spectra were collected from free HSA and HSA-ule or HSA-col complexes, with excitation and emission wavelengths of 290 nm and 345 nm, respectively (Figure 4.16). After the addition of boron compounds, a reduction in fluorescence intensity was observed without major shifts in the HSA fluorescence spectrum, which indicates the presence of complex formation. In particular, such a quenching in fluorescence spectra may result from excited-state reactions, molecular rearrangements, energy transfer, ground state complex formation, conformational changes or collision quenching<sup>282</sup>. Depending on the fluorescence intensity of Trp at 345 nm, the quenching data can be analyzed according to Stern-Volmer equation:  $F_0/F = K [Q] + 1$  where  $F_0$  and  $F$  are the fluorescence intensity in the absence and presence of quencher,  $K$  is the Stern-Volmer quenching constant taken as the binding constant of the small molecule and  $[Q]$  is the concentration of the quencher. The slope of the  $F_0/F$  versus  $[Q]$  plot can therefore be used to calculate the  $K$  value<sup>207</sup>. The plot of  $F_0/F$  as a function of quencher concentration is shown in Figure 4.16A' and 4.16B'. The binding constants obtained were  $K_{ule} = 1.37 \times 10^{-3} \text{ M}^{-1}$  and  $K_{col} = 1.78 \times 10^{-3} \text{ M}^{-1}$ , which suggests a low affinity between boron compounds and serum albumin. The calculated association constants from fluorescence spectroscopy exhibited great similarity. The absence of any shift in the fluorescence spectra indicates that the polar environment of

Trp 214 did not change after the binding of boron compounds<sup>283</sup>. In addition, borates may bind to IIA binding site in HSA near Trp 214.

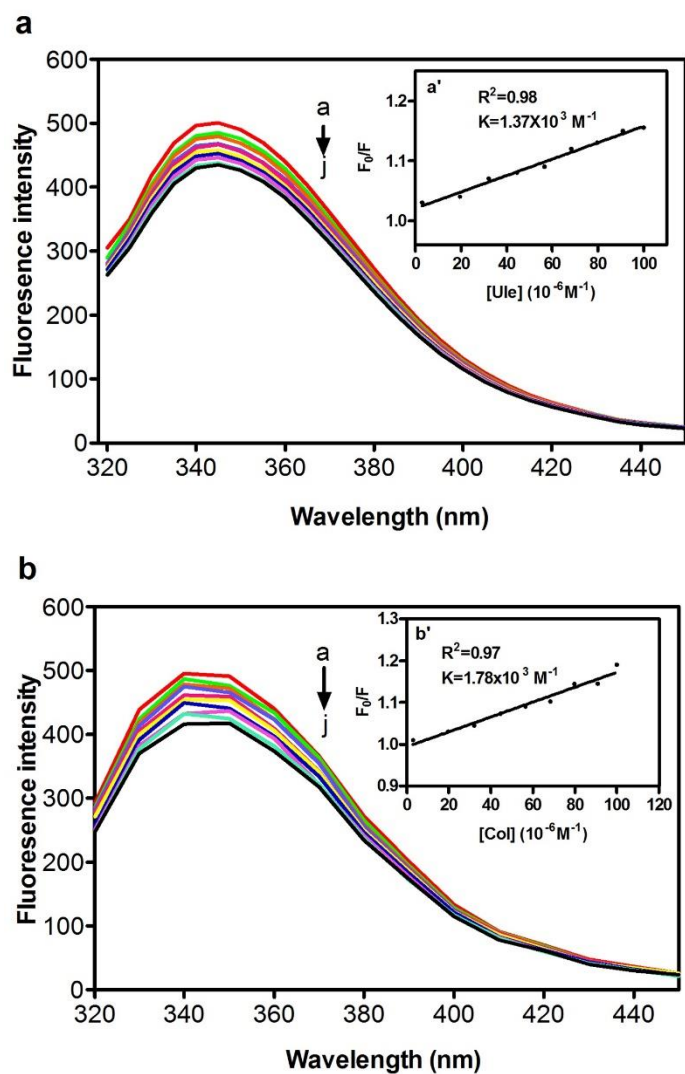


**Figure 4.16** Fluorescence emission spectra of HSA-borate complexes in aqueous solution (pH 7.4) for the interactions of HSA-ule **a**) and HSA-col **b**); a: 3  $\mu$ M of free HSA, b-j: HSA-borate complexes for the borate concentrations of 3-100  $\mu$ M. Inset plots show Stern-Volmer plots of HSA-ule (a') and HSA-col (b') at 298 K.

#### 4.2.3.3 Analysis of Protein Conformation

CD studies are useful to determine protein interactions, folding and secondary structure<sup>284</sup>. The two negative bands at 209 and 221 nm are characteristic in the CD spectrum of the HSA, and occur due to the  $n \rightarrow \pi^*$  and  $\pi \rightarrow \pi^*$  transitions of amide groups in the far UV region<sup>285, 286</sup>. Shifts in the CD spectrum of serum albumin after treatment with boron compounds were used to estimate changes in the secondary structure of the protein upon interaction with ule or col. Our data suggest that ule and col exhibit similar behaviors in CD spectra (Figure 4.17). Furthermore, no change in the shape of CD spectra was observed.

According to equation based on mean residue ellipticity value at 208 nm, free HSA had  $\alpha$ -helix content of 58%. Upon the addition of boron compounds, a minor reduction in the  $\alpha$ -helix content of the protein could be observed as a reduction in the CD signal without any shift. The quantitative results revealed that  $\alpha$ -helix content of HSA decreased to 53% following ule binding, and to 52% following col binding which was indicator of loss of  $\alpha$ -helical content of serum protein and binding of boron compounds to the protein<sup>287</sup>.

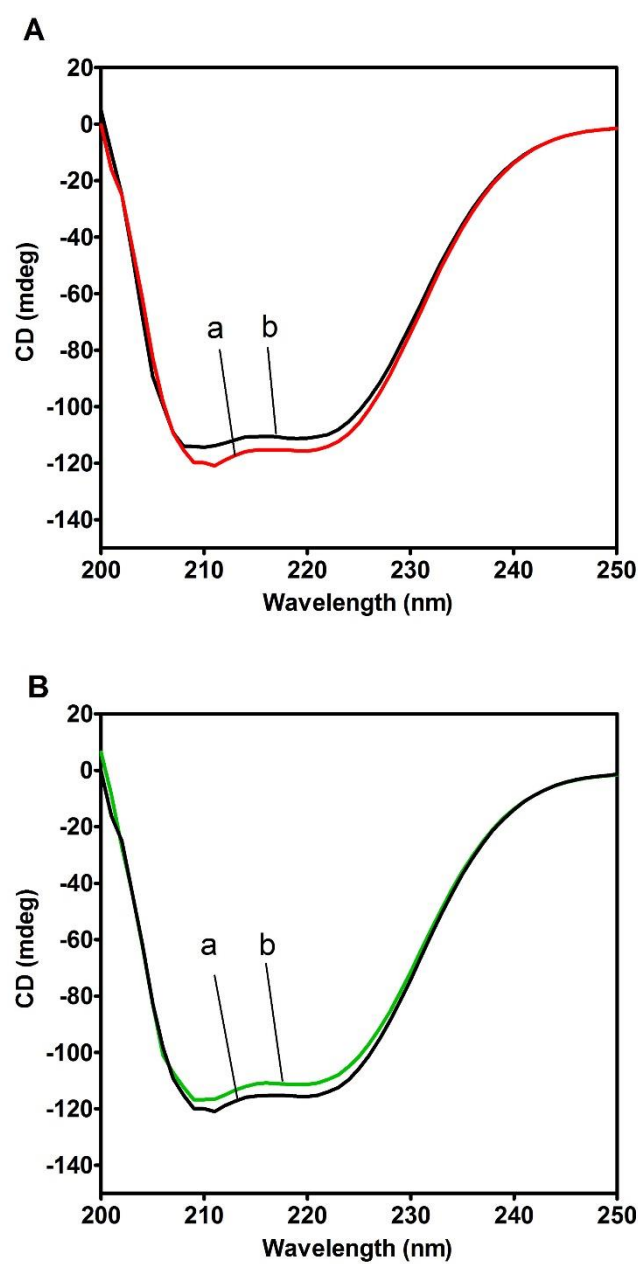


**Figure 4.17** CD spectra of HSA-ule **A**) and HSA-col **B**) interactions (a: 1  $\mu$ M of free HSA, b: HSA-borate complexes (50  $\mu$ M of ule or col) in 5 mM Tris-HCl buffer (pH 7.4) at 298 K.

#### 4.2.3.4 Structural Analysis of HSA Binding of Borates

FT-IR spectroscopy can be used to reveal the secondary structure of globular proteins based on the vibrational frequencies and vibrational modes of their functional groups. The amide I band in particular is highly sensitive to conformational changes. However, it must be kept in mind that the results of FT-IR-based secondary structure analysis may not be consistent with those derived from other techniques, due to the fact that regions associated with certain structures may overlap<sup>276</sup>. For example; while X-ray crystallography analysis suggests that HSA does not contain  $\beta$ -structures ( $\beta$ -turns or  $\beta$ -sheets), peaks associated with these motifs are observed in the IR spectrum of HSA, and are in fact attributable to a low frequency  $\alpha$ -helix band.

The IR spectrum of HSA exhibits characteristic bands at around 1652  $\text{cm}^{-1}$  and 1546  $\text{cm}^{-1}$ , attributed to the amide I and amide II bands, respectively. Figure 4.18 is the FT-IR spectra of the free HSA, and difference spectra of HSA obtained by subtraction of the spectrum of free borates from the HSA-borate complexes. As can be seen in Figure 4.18, peak positions were slightly changed upon the binding of both ule and col. In particular, at a 1:1 molar ratio of HSA:ule, the amide II band shifted from 1652 to 1642  $\text{cm}^{-1}$ , while a shift from 1652 to 1645  $\text{cm}^{-1}$  was observed in a mixture of HSA:col at 1:4 molar ratio. We observed minimal changes in the shape, position and the intensity of amide I bands after exposure of boron compounds at different concentrations, which is also evaluated quantitatively in Table 4.4.

Curve fitting analysis of the amide I region in the 1600-1700  $\text{cm}^{-1}$  range demonstrated that col binding resulted in minor protein secondary structural changes, such that the percentage ratio of  $\alpha$ -helices shifted from 55% (free HSA) to 53% at 1:1 molar ratio,

and to 51% at 1:4 molar ratio.  $\beta$ -sheet associated peaks increased from 18% (free HSA) to 23-24%, while initial  $\beta$ -turn (14%) and random coil (13%) ratios of free HSA changed by 1-3% with the addition of different concentrations of col. In ule-HSA complexes, the composition changed to 51%  $\alpha$ -helix, 22%  $\beta$ -sheet, 18%  $\beta$ -turn and 9% random coil at the highest concentration.

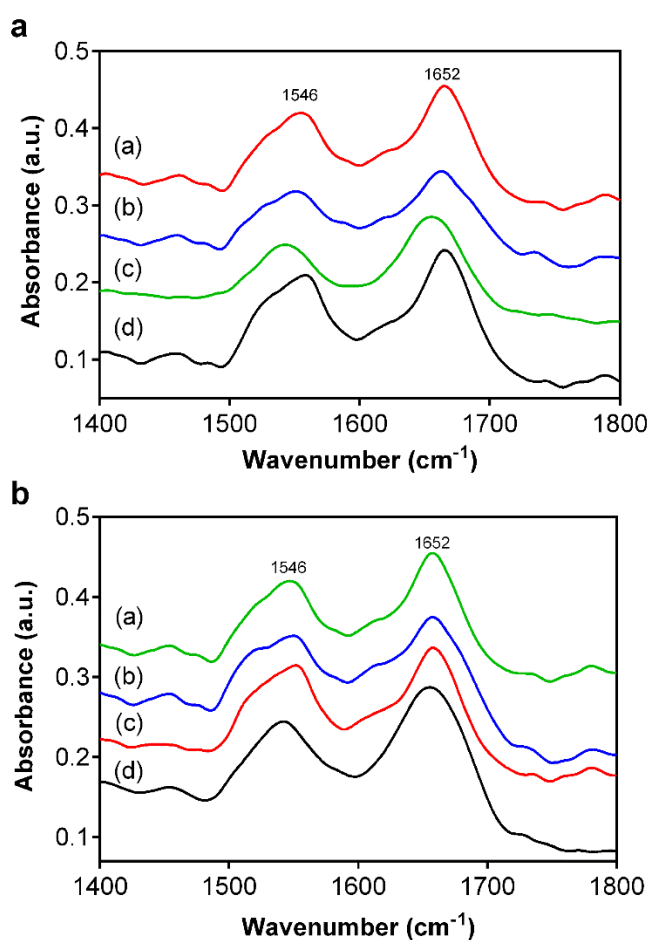


**Figure 4.18** FT-IR spectra and difference spectra of HSA-ule **a)** and HSA-col **b)** interactions in aqueous solutions under different molar ratios (a, b, c, d; [1:0], [1:0.5],

[1:1], [1:4] respectively). The final concentration of HSA was kept constant at 0.25 mM in each sample.

Difference spectra of HSA (b-d) obtained by subtracting the spectrum of free borates from that of the HSA-Borate complex is in the range of 1800-1400  $\text{cm}^{-1}$ .

**Table 4.4** Curve fitting analysis results of 0.25 mM free HSA and protein incubated with ule and col at different concentrations at pH 7.4. The wavelength values at each row represent where the maximal peak values for the defined group occur. The percentage values at each row represent the percentage of the area for the defined group with respect to the total surface area at 1600-1700  $\text{cm}^{-1}$  region. The area percentage values are the averages of triplicate samples.

Sample	$\alpha$ - helix (1660 – 1649 $\text{cm}^{-1}$ ) (%)( $\pm 3$ )	$\beta$ - sheet (1640 – 1615 $\text{cm}^{-1}$ ) (%)( $\pm 3$ )	$\beta$ - turn (1680 – 1661 $\text{cm}^{-1}$ ) (%)( $\pm 4$ )	Random (1648 – 1641 $\text{cm}^{-1}$ ) (%)( $\pm 2$ )
Free HSA	55	18	14	13
[HSA : col] [1:0.5]	55	21	11	13
[1:1]	53	23	12	12
[1:4]	51	24	14	11
[HSA : ule] [1:0.5]	55	17	16	12
[1:1]	52	20	16	12
[1:4]	51	22	18	9

#### 4.2.3.5 Cytotoxicity of Boron Compounds on HUVECs

Here, we evaluated the toxicity of boron compounds against human umbilical vein endothelial cells (HUVEC) using the Alamar blue cell viability assay. This assay measures the reducing environment (i.e. the aerobic activity) of cells through the reduction of resazurin to resorufin. The effect of ule and col on the above-mentioned cell line was investigated after 48 h incubation period (Figure 4.19). Our results revealed that viabilities of HUVECs were not affected by the addition of ule or col at all tested concentrations, indicating that both compounds are non-toxic to HUVECs. Although Turkez *et al.* demonstrated that these boron compounds have antioxidant capacity and no genotoxic effect in blood cells, they may result in oxidative stress in excessive concentrations<sup>242</sup>.

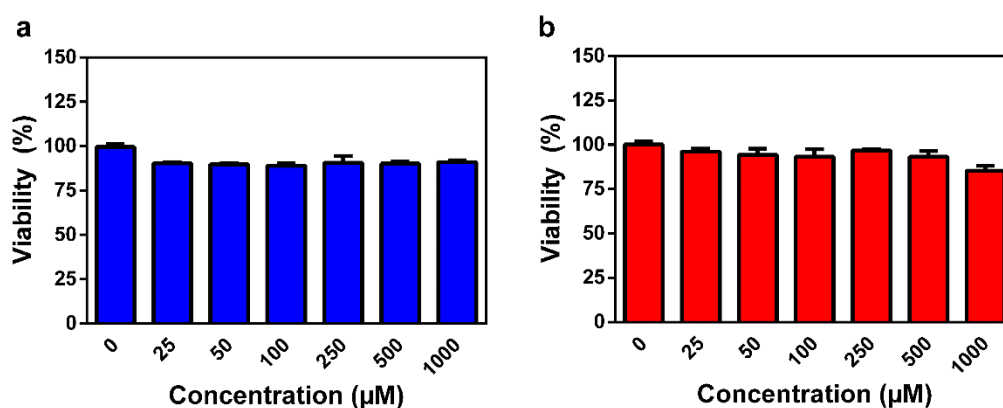


**Figure 4.19** Variations in HUVEC viability after 48 h incubation with different concentrations of borates; HUVECs treated with ule **a)** and HUVECs treated with col **b)** at varying concentrations. The results are expressed as means  $\pm$  SEM (n = 4) and presented as percentages of control.

### 4.3 CONCLUSION

In this chapter, DNA and HSA binding properties of BA and two common natural borates were investigated by different tools. Hyperchromic shifts in the absorption spectra of DNA-BA mixtures suggested the non-intercalative binding of half metal to DNA. The capability of BA binding to DNA was also monitored with electron microscopy technique. Shifts in characteristic peaks of CT DNA was evaluated upon binding of BA and the possible target for BA was found to be the deoxyribose sugar of DNA. The studies about the effects of BA on the secondary structure of CT DNA revealed that the secondary structure of DNA was not so much influenced after incubation with low concentrations of BA, but DNA degradation may occur at high concentrations. Calorimetric data indicated that an exothermic reaction takes place during the binding of BA to CT DNA and this half metal has a moderate affinity to CT DNA.

According to our results, we concluded that both boron compounds can bind to CT DNA with similar DNA binding characteristics. The ability to cleave DNA is the main characteristic of DNA intercalators used as anticancer agents. We therefore tested the effects of ule and col on CT DNA and observed that borates do not cause the unwinding of the DNA helix or any other significant change in its secondary structure. In addition, CD and FT-IR spectroscopy results indicated that both compounds interact with DNA under a non-intercalative mode of binding, and borates might interact with DNA through sugar-phosphate backbone binding. In terms of serum albumin binding characteristics, ule and col have similar properties, and electrostatic interactions may play an important role during the binding process. After interacting with the boron compounds, slight changes were observed in the secondary structure of HSA, which

may be explained by the external binding of the borate to the serum protein through electrostatic interactions. Fluorescence quenching experiments showed moderate binding for the borate compounds ule and col. It is remarkable that borates cause no endothelial cytotoxicity at all tested concentrations. This chapter highlights the importance of small structural differences for the binding characteristics of a potential biomolecular targeting ligand which could influence its activity as a drug.

The well-known applications of boron containing compounds based on the interaction between enzymes or nuclear receptors and boron as a ligand<sup>288</sup>. These studies focused on the biological outcomes of these interactions and toxicity of these compounds. In spite of these findings, the direct interaction of these compounds with DNA or serum albumin is not understood. The potential targets of boron compounds have been described in this study.

Several studies revealed that there are two important sites (I and II) for ligand binding to HSA. The well-known site specific marker molecules should be used to further explore binding region of a molecule in serum albumin. Warfarin is a bulky heterocyclic anion and used as anticoagulant drug. Ibuprofen is an aromatic carboxylate and used as non-steroidal anti-inflammatory agent. They have very high affinity for Sudlow's site I and II, respectively<sup>289</sup>. Site marker competitive experiments should be performed by using these drugs to further investigate effect of boric acid and borates on HSA.

## 4.4 EXPERIMENTAL SECTION

### 4.4.1 Materials and solutions

All reagents are used as purchased. Ultrapure CT DNA (CAT No. 15633–019) was obtained from Invitrogen, CA. pUC19 plasmid DNA and Quick-Load® 1 kb DNA ladder were purchased from New England Biolabs, UK. HSA, Tris(hydroxymethyl)aminomethane (Tris), BA and EtBr were obtained from Sigma-Aldrich Chemicals, USA.  $\text{Ca}_2\text{B}_6\text{O}_{11}\cdot 5\text{H}_2\text{O}$  (CAS No. 1318-33-8, ~92% pure) and  $\text{NaCaB}_5\text{O}_9\cdot 8\text{H}_2\text{O}$  (CAS No. 1319-33-1, ~93% pure) were supplied from Eti Mine Works General Management, Turkey. All reagents were used as supplied without further purification. The chemical structures of two borates were drawn with ACD/ChemSketch (Advanced Chemistry Development Inc., Canada) software. 0.01 M Tris-HCl buffer (pH 7.4) was used as buffer medium in experiments. Buffer pH was adjusted using NaOH or HCl. Stock solutions of borates were prepared by dissolving boron compounds to a concentration of 1.0 M in nanopure water. Stock solutions were diluted as necessary to obtain the desired concentrations prior to each experiment. DNA concentration per nucleotide was determined spectrophotometrically using a molar absorptivity of  $6600 \text{ M}^{-1} \text{ cm}^{-1}$  at 260 nm<sup>290</sup>. The ratio of absorbance at 260 and 280 nm was found to be 1.8, indicating the purity of DNA<sup>291</sup>. Concentrations of diluted HSA solutions were determined spectrophotometrically, using a molar extinction coefficient of  $3.66 \times 10^4 \text{ L mol}^{-1} \text{ cm}^{-1}$  at 280 nm<sup>292</sup>.

### 4.4.2 UV-Vis absorbance spectroscopy

Electronic absorption spectra were measured with a Thermo Scientific NanoDrop 2000 benchtop spectrophotometer (Thermo-Fisher Scientific, USA) at 297 K. The

spectra were obtained by keeping the concentration of DNA at 0.01 mM while varying concentrations of BA (0.01, 0.05, 0.1, and 0.50 mM) in 0.01 M Tris-EDTA (pH 8.0). Mixtures were allowed to incubate for 1 h before measurement. The absorption titration experiments were performed by titrating either varying concentrations of borates (0.001–0.1 mM) against a constant concentration of CT DNA (0.01 mM) or titrating varying concentrations of CT DNA (0.1, 0.2 mM) against a constant concentration of borates (0.1 mM). The titration readings were recorded in the wavelength range of 200–800 nm. The absorbance measurements were performed by keeping the HSA concentration constant (0.01 mM) while varying the borate concentrations from 0.01 mM to 1 mM.

#### **4.4.3 EtBr displacement assay**

Displacement assay was performed in the presence of increasing concentration of boron compounds (0.1–1 M) and constant concentrations of CT DNA (0.1 M) and EtBr (0.01 M) in 0.01 M Tris–HCl buffer (pH 7.4) at room temperature. The same procedure was applied as mentioned in Section 3.4.3.

#### **4.4.4 TEM**

Free CT DNA (0.1 mM), free BA (1 mM), and CT DNA (0.1 mM) - BA (1 mM) mixtures were placed on a copper TEM grid coated with carbon film and negative stained with 2% uranyl acetate for 5 min. Following staining, the excess solution on grid was removed by pipetting, and the grid was allowed to air dry prior to imaging. TEM images were taken by using a Tecnai G2 Spirit Biotwin microscope (FEI, USA) at an accelerated voltage of 80 kV.

#### **4.4.5 ITC**

ITC experiments were performed on an ITC200 microcalorimeter (Microcal®, USA) at 25 °C. One site binding model was employed for the analysis of interaction between BA and CT DNA by the Windows-based Origin software pack (Microcal®, USA) following baseline adjustment. DNA (0.5 mM) was maintained in the sample cell and the reference cell contained doubly distilled water. 5 mM BA solution was introduced into the sample cell by means of syringes. All the solutions were thoroughly degassed prior to use. Thermodynamic parameters were calculated with the formula mentioned in previous chapter.

#### **4.4.6 DNA cleavage and mobility experiments**

For the gel electrophoresis experiments, CT DNA (50 ng/μL) or pUC19 plasmid DNA (11 ng/μL) was treated with varying concentrations of borates and then samples were incubated for 1–2 h at 37 °C. Samples were analyzed by electrophoresis for 90 min at 70 V on 1% agarose gel containing Tris-acetate–EDTA (TAE) buffer. The gel was stained with 1 μg/mL of EtBr and the DNA bands were visualized under UV light, and photographed by using Gel Documentation System (Bio-Rad, USA).

#### **4.4.7 Fluorescence measurements**

HSA stock solution was prepared in 10 mM Tris-HCl buffer (pH 7.4) at room temperature, with a concentration of 6 μM. Various concentrations of borate hydrate solutions (6-200 μM) were mixed with equal concentration of HSA (3 μM) to obtain final concentrations of borates in the range of 3-100 μM in the HSA-Borate mixture. Fluorescence readings were taken after 10 min. Excitation wavelength was set at 290 nm, while emissions were recorded from 300 - 500 nm. Readings were conducted with

SpectraMax M5 Microplate Reader (Molecular Devices, US) in a quartz cuvette with a 0.01 cm path length.

#### **4.4.8 CD spectroscopy**

Spectra of CT DNA and borate mixtures were recorded with Jasco J-815 spectrophotometer (Jasco, UK) using quartz cuvettes with 0.1 cm path-lengths and three scans averaged for each CD spectrum. CD spectra were obtained using a scan speed of 100 nm/min at 25 °C in a nitrogen atmosphere. For each measurement a spectrum of buffer solution was taken and subtracted from the spectra of DNA or HSA and borate-biomacromolecule mixtures through base line correction. All spectra were acquired in the wavelength range 200–320 nm for DNA or 190-250 nm for HSA experiments. The CD spectra of BA (0.1 mM) – DNA (0.1 mM) mixtures in 10 mM Tris-HCl (pH 7.5) were recorded after successive additions of BA. Titrations were performed by keeping the concentration of CT DNA constant (0.01 mM) while the concentration of ule (0.025-0.2 mM) or col (0.01-0.1 mM) was varied in a solution containing 0.005 M Tris-HCl buffer (pH 7.4). The CD spectra of HSA (1 μM) were taken in the presence and absence of ule (50 μM) and col (50 μM). All plottings were conducted using GraphPad Prism5 software (La Jolla, CA). The results were taken as millidegrees. The α-helix content of HSA was calculated from the molar ellipticity ( $\theta$ ) at 208 nm according to the following equation <sup>293</sup>.

$$\% \text{ helix} = (-[\theta]_{208} - 4000) / (33000 - 4000) \times 100$$

#### 4.4.9 FT-IR spectroscopy

FTIR spectra of free biomacromolecule and biomacromolecule-borate mixtures were recorded on a Nicolet 6700 FT-IR Spectrometer (Thermo-Scientific, US) equipped with a deuterated triglycine sulfate (DTGS) detector and a KBr beamsplitter over the spectral range 1800–600  $\text{cm}^{-1}$  with a resolution of 4  $\text{cm}^{-1}$  and 128 scans. Spectra were recorded with BA concentrations 0.25, 0.5, 1 mM and a final CT DNA concentration of 1 mM (n=3). The FT-IR spectra were recorded after 3 h incubation of borates (0.1–2 mM) with a final DNA concentration of 1 mg/mL in Tris–HCl buffer (pH 7.4). A sharp band of CT DNA at 968  $\text{cm}^{-1}$  was used as an internal reference band<sup>294</sup>. We used the same procedure during FT-IR experiments as explained in Section 3.4.6. IR spectrum of free borates is recorded and subtracted from the spectra of borate/DNA complexes. This is done to ensure that the observed changes in peak positions and intensities in DNA are due to interaction with borates. Difference spectra [(borate/CT-DNA complexes)–(borate)] were generated after normalization.

Solutions of borates were added dropwise to obtain homogenous mixtures with borate concentrations of 1 mM, 0.25 mM and 0.1 mM, and a final HSA concentration of 0.25 mM. After 3 h of incubation, 20  $\mu\text{L}$  of borate-HSA mixtures were dropped and subsequently dried on a 96-well plate at 37 °C for 1 h prior to FT-IR transmittance analysis. Curve fitting analysis of the amide I region between 1700–1600  $\text{cm}^{-1}$  was performed to fit the Lorentzian line shapes in order to estimate approximate ratios of four main subgroups of protein secondary structures, with respect to the total protein content. The regions of interest were 1615 – 1640  $\text{cm}^{-1}$  for  $\beta$ -sheets, 1641 – 1648  $\text{cm}^{-1}$

for random coils, 1649 - 1660  $\text{cm}^{-1}$  for  $\alpha$ -helices, and 1661 - 1680  $\text{cm}^{-1}$  for  $\beta$ -turns<sup>295</sup>.

All tests were done in triplicate.

Analysis of all spectroscopy data and statistical analysis were performed using GrapPad Prism software version 5.00 for Windows (GraphPad Software, San Diego, California).

#### **4.4.10 Cytotoxicity assay**

HUVECs (American Type Culture Collection) were cultured in 75  $\text{cm}^2$  culture flasks using DMEM (Gibco) supplemented with 10% FBS and 1% penicillin/streptomycin (Gibco) at 37 °C and 5%  $\text{CO}_2$ . Viabilities of these cells were determined via Alamar blue assay with and without the inclusion of borate compounds. In a 96-well plate, cells were seeded at density of  $1 \times 10^4$  cells per well and cultured at standard conditions prior to borate treatment. Varying concentrations of sterilized borate compounds (0-1000  $\mu\text{M}$ ) prepared in DMEM were added to each well, and the cells were then incubated for 48 h. The same procedure was applied for Alamar blue assay as explained in Section 2.4.9.1. Results were analyzed for statistical significance using ANOVA and Tukey tests. Changes were considered significant at  $p < 0.05$ . Each experiment was performed in quadruplicate ( $n = 4$ ).

## **Chapter 5**

### **CONCLUSION and PROSPECTS**

Cancer is one of the most common causes of death in the world. Each year millions of people are diagnosed with cancer and get therapy to overcome this disease. Although there are standard screening procedures in clinics, they are not sensitive and accurate enough for early detection of most tumors. In recent years, new improvements in material design and treatments have facilitated the understanding of cancer biology. However, there are still several challenges to fully overcome cancer due to its heterogeneous nature and contributions of several metabolic factors. Nowadays, researchers have focused on developing new agents for early diagnosis of cancer and more efficient cancer treatment.

Research on SPIONs has been growing exponentially in the last decade. SPIONs are used as negative contrast agents for MRI, but their application is generally limited to the detection of liver pathologies in clinics. Effective synthetic methods have been developed for direct fabrication of surface-functionalized, water-soluble iron oxide nanoparticles, but these techniques are generally incapable of producing nanoparticles with diameters below 100 nm. Thermal decomposition can be used to synthesize smaller sized hydrophobic SPIONs (5-10 nm), and these nanoparticles can then be coated with a hydrophilic ligand to increase their solubility and allow their use in biomedical applications. SPIONs are capable of binding and carrying several small molecules such as drugs, DNA, protein, peptide and other imaging probes which are generally covalently attached to the surface. It is possible to achieve cancer cell specific targeting of nanoparticles by using receptor mediated interactions. For this purpose, biological ligands or synthetic materials mimicking the function of ligand of interest, which are highly expressed in tumor cells rather than healthy cells, could be used. Although angiogenesis is a well-known biological process during growth,

development and wound healing, it is also important for the development of the malignancy of cancer. NRP-1 is a receptor protein for VEGF165 and is overexpressed by most of the tumor cells, in addition to being associated with tumor angiogenesis. It has been reported that peptides with LPPR amino acid sequence selectively bind to NRP-1 and inhibit binding of VEGF165. Peptides are a commonly employed type of targeting ligand for cancer imaging, and have been demonstrated to stimulate increased accumulation of functionalized nanoparticles in cancer cells, in addition to imparting with desirable RES and blood clearance profiles.

In this thesis, the surface functionalization of SPIONs with LPPR-PA or K-PA to allow their selective uptake into the tumor vascular cells was demonstrated. The fabrication, structure, stability, morphology and targeting capacities of PA-coated SPIONs were characterized, and their effects on viability of HUVECs and breast cancer cells were demonstrated. In particular, the effects of PA-coated SPIONs on the tube formation characteristics of vascular cells were investigated through Matrigel assay and the localization of the SPIONs were confirmed within the cells. This PA/SPION co-assembled system aims to enhance MRI negative contrast in tumor tissue rather than healthy organs, therefore, we tested whether PA-coated SPIONs demonstrate the capacity to serve as contrast agents for *in vivo* tumor detection in chemically induced breast cancer model by MRI following 4 h and 15 days after intravenous injection of SPIONs to Sprague-Dawley rats. Biodistribution analysis was performed for various organs to determine the possible toxicity and accumulation of PA-coated SPIONs. Viability assays indicated presence of a high degree of biocompatibility of nanoparticles and free PAs, but we observed cell specific toxicity at high concentrations of samples. The comparison of effect of SPION-K and SPION-LPPR

on tube formation of human vascular endothelial cells indicated that SPION-LPPR selectively prevents angiogenesis process, probably by binding to NRP-1 receptor.

MR imaging revealed that SPION/K-PA accumulated in tumor tissues enhancing their imaging potential. Although nanoparticles immediately accumulated in RES organs and especially in the liver and kidney within minutes, the MR signal intensity in these organs diminished after 1 h and nanoparticles were subsequently cleared from these organs within two weeks. Histological observations also validated the accumulation of nanoparticles in tumor tissue at 4 h and their bioelimination from the organs of both healthy and experimental rats after two weeks. The absence of pathological inflammatory responses revealed the biocompatibility of SPION/K-PA *in vivo*. Overall, K-PA functionalized SPIONs appear to be a suitable negative contrast agent for *in vivo* tumor imaging by MR.

The binding of a molecule to biomacromolecules provides insight into the evolution of chemico-biological interactions for biochemistry, drug design and pharmacology. In the rest of the thesis, I investigated the binding mechanism and affinities of Au, Ga, BA, ule and col to DNA and HSA. Furthermore, their effects on the structures of these biomacromolecules were examined in detail by using various spectroscopic and calorimetric methods to predict their potential targets and to explore their anticancer potential as well as possible mechanism of action. The subtle differences between the metal or half-metal/biomacromolecule interactions were described. In addition, chemoprevention of metal ions against breast cancer cells was demonstrated. On the other hand, the absence of toxicity against health tissue was revealed on HUVECs.

Our investigation of the metal or half-metal/biomacromolecule binding mechanism is of considerable importance for the development of new therapeutic materials for cancer therapy. The effectiveness of a therapy is mostly based on high accumulation rate of therapeutic molecule in tumor tissue. Understanding of binding kinetics, structural effects of potential therapeutic agents on biological molecules and possible functions of these molecules could help the design of drugs and drug delivery systems to increase success of therapy. The metal based drugs with anti-tumor activity will have a great significance for development in chemotherapy.

## Bibliography

1. Baird A-M, Gray SG, Richard DJ, O'Byrne KJ. Promotion of a cancer-like phenotype, through chronic exposure to inflammatory cytokines and hypoxia in a bronchial epithelial cell line model. *Scientific Reports* 2016;6:18907.
2. Hanahan D, Weinberg RA. The Hallmarks of Cancer. *Cell* 2000;100:57-70.
3. Kim YJ, Dev R, Reddy A et al. Association Between Tobacco Use, Symptom Expression, and Alcohol and Illicit Drug Use in Advanced Cancer Patients. *Journal of Pain and Symptom Management*.
4. Espinosa P, Pfeiffer RM, García-Casado Z et al. Risk factors for keratinocyte skin cancer in patients diagnosed with melanoma, a large retrospective study. *European Journal of Cancer* 2016;53:115-124.
5. Linares MA, Zakaria A, Nizran P. Skin Cancer. *Primary Care: Clinics in Office Practice* 2015;42:645-659.
6. Alemany L, Cubilla A, Halc G et al. Role of Human Papillomavirus in Penile Carcinomas Worldwide. *European Urology*.
7. Gilbert L. In regard to: "Why is it appropriate to recommend human papillomavirus vaccination as cervical cancer prevention?". *American Journal of Obstetrics and Gynecology*.
8. Shi Y, Wang J, Wang Y et al. A novel mutant 10Ala/Arg together with mutant 144Ser/Arg of hepatitis B virus X protein involved in hepatitis B virus-related hepatocarcinogenesis in HepG2 cell lines. *Cancer Letters* 2016;371:285-291.
9. Islami F, Dikshit R, Mallath MK, Jemal A. Primary liver cancer deaths and related years of life lost attributable to hepatitis B and C viruses in India. *Cancer Epidemiology* 2016;40:79-86.
10. Zhou J, Wang W, Xie Y et al. Proteomics-Based Identification and Analysis of Proteins Associated with Helicobacter pylori in Gastric Cancer. *PLoS ONE* 2016;11:e0146521.
11. Kong SY, Takeuchi M, Hyogo H et al. The Association between Glyceraldehyde-Derived Advanced Glycation End-Products and Colorectal Cancer Risk. *Cancer Epidemiology Biomarkers & Prevention* 2015;24:1855-1863.
12. Lin JE, Colon-Gonzalez F, Blomain E et al. Obesity-Induced Colorectal Cancer Is Driven by Caloric Silencing of the Guanylin-GUCY2C Paracrine Signaling Axis. *Cancer Research* 2016;76:339-346.
13. Boyle T, Lynch BM, Ransom EK, Vallance JK. Volume and correlates of objectively measured physical activity and sedentary time in non-Hodgkin lymphoma survivors. *Psycho-Oncology* 2015:n/a-n/a.
14. da Silva PL, Do Amaral VC, Gabrielli V et al. Prolactin promotes breast cancer cell migration through actin cytoskeleton remodeling. *Frontiers in Endocrinology* 2015;6.
15. Spinelli FM, Vitale DL, Demarchi G, Cristina C, Alaniz L. The immunological effect of hyaluronan in tumor angiogenesis. *Clinical & Translational Immunology* 2015;4:e52.
16. Jemal A, Siegel R, Xu J, Ward E. Cancer Statistics, 2010. *CA: A Cancer Journal for Clinicians* 2010;60:277-300.
17. Siegel R, Ma J, Zou Z, Jemal A. Cancer statistics, 2014. *CA: A Cancer Journal for Clinicians* 2014;64:9-29.
18. Yilmaz HH, Yazihan N, Tunca D et al. Cancer Trends and Incidence and Mortality Patterns in Turkey. *Japanese Journal of Clinical Oncology* 2011;41:10-16.
19. Nie S, Xing Y, Kim GJ, Simons JW. Nanotechnology applications in cancer. *Annu Rev Biomed Eng* 2007;9:257-288.

20. Zen K, Zhang C-Y. Circulating MicroRNAs: a novel class of biomarkers to diagnose and monitor human cancers. *Medicinal Research Reviews* 2012;32:326-348.
21. Pu F, Qiao J, Xue S et al. GRPR-targeted Protein Contrast Agents for Molecular Imaging of Receptor Expression in Cancers by MRI. *Sci Rep* 2015;5:16214.
22. Geninatti Crich S, Cadenazzi M, Lanzardo S et al. Targeting ferritin receptors for the selective delivery of imaging and therapeutic agents to breast cancer cells. *Nanoscale* 2015;7:6527-6533.
23. Duffy MJ, Lamerz R, Haglund C et al. Tumor markers in colorectal cancer, gastric cancer and gastrointestinal stromal cancers: European group on tumor markers 2014 guidelines update. *International Journal of Cancer* 2014;134:2513-2522.
24. de la Chapelle A, Hampel H. Clinical Relevance of Microsatellite Instability in Colorectal Cancer. *Journal of Clinical Oncology* 2010;28:3380-3387.
25. Cai W, Chen X. Multimodality Molecular Imaging of Tumor Angiogenesis. *Journal of Nuclear Medicine* 2008;49:113S-128S.
26. Patnaik A, LoRusso PM, Messersmith WA et al. A Phase Ib study evaluating MNRP1685A, a fully human anti-NRP1 monoclonal antibody, in combination with bevacizumab and paclitaxel in patients with advanced solid tumors. *Cancer Chemother Pharmacol* 2014;73:951-960.
27. Weekes CD, Beeram M, Tolcher AW et al. A phase I study of the human monoclonal anti-NRP1 antibody MNRP1685A in patients with advanced solid tumors. *Invest New Drugs* 2014;32:653-660.
28. He X, Wang K, Cheng Z. In vivo near-infrared fluorescence imaging of cancer with nanoparticle-based probes. *Wiley Interdisciplinary Reviews: Nanomedicine and Nanobiotechnology* 2010;2:349-366.
29. Huang Y, He S, Cao W, Cai K, Liang XJ. Biomedical nanomaterials for imaging-guided cancer therapy. *Nanoscale* 2012;4:6135-6149.
30. Tubiana M. Computed tomography and radiation exposure. *N Engl J Med* 2008;358:850; author reply 852-853.
31. Kim D, Park S, Lee JH, Jeong YY, Jon S. Antibiofouling Polymer-Coated Gold Nanoparticles as a Contrast Agent for in Vivo X-ray Computed Tomography Imaging. *Journal of the American Chemical Society* 2007;129:7661-7665.
32. Aaron Fenster and Dónal BDaHNC. Three-dimensional ultrasound imaging. *Physics in Medicine and Biology* 2001;46:R67.
33. Lindner JR, Song J, Xu F et al. Noninvasive Ultrasound Imaging of Inflammation Using Microbubbles Targeted to Activated Leukocytes. *Circulation* 2000;102:2745-2750.
34. Klibanov AL. Microbubble Contrast Agents: Targeted Ultrasound Imaging and Ultrasound-Assisted Drug-Delivery Applications. *Investigative Radiology* 2006;41.
35. Ellegala DB, Leong-Poi H, Carpenter JE et al. Imaging Tumor Angiogenesis With Contrast Ultrasound and Microbubbles Targeted to  $\alpha\beta 3$ . *Circulation* 2003;108:336-341.
36. Kobayashi H, Choyke PL. Target-Cancer-Cell-Specific Activatable Fluorescence Imaging Probes: Rational Design and in Vivo Applications. *Accounts of Chemical Research* 2011;44:83-90.
37. Sima PD, Kanofsky JR. Cyanine dyes as protectors of K562 cells from photosensitized cell damage. *Photochem Photobiol* 2000;71:413-421.
38. Luo S, Zhang E, Su Y, Cheng T, Shi C. A review of NIR dyes in cancer targeting and imaging. *Biomaterials* 2011;32:7127-7138.

39. van Dam GM, Themelis G, Crane LMA et al. Intraoperative tumor-specific fluorescence imaging in ovarian cancer by folate receptor-[alpha] targeting: first in-human results. *Nat Med* 2011;17:1315-1319.
40. Pham W, Medarova Z, Moore A. Synthesis and application of a water-soluble near-infrared dye for cancer detection using optical imaging. *Bioconjug Chem* 2005;16:735-740.
41. Frullano L, Meade TJ. Multimodal MRI contrast agents. *J Biol Inorg Chem* 2007;12:939-949.
42. Hingorani DV, Bernstein AS, Pagel MD. A review of responsive MRI contrast agents: 2005–2014. *Contrast Media & Molecular Imaging* 2015;10:245-265.
43. Shin TH, Choi Y, Kim S, Cheon J. Recent advances in magnetic nanoparticle-based multi-modal imaging. *Chem Soc Rev* 2015;44:4501-4516.
44. Hricak H. MR imaging and MR spectroscopic imaging in the pre-treatment evaluation of prostate cancer. *Br J Radiol* 2005;78 Spec No 2:S103-111.
45. Major JL, Meade TJ. Bioresponsive, cell-penetrating, and multimeric MR contrast agents. *Acc Chem Res* 2009;42:893-903.
46. Blasiak B, Veggel FCJMv, Tomanek B. Applications of Nanoparticles for MRI Cancer Diagnosis and Therapy. *Journal of Nanomaterials*, 2013.
47. Xue S, Yang H, Qiao J et al. Protein MRI contrast agent with unprecedented metal selectivity and sensitivity for liver cancer imaging. *Proc Natl Acad Sci U S A* 2015;112:6607-6612.
48. Chen R, Ling D, Zhao L et al. Parallel Comparative Studies on Mouse Toxicity of Oxide Nanoparticle- and Gadolinium-Based T1 MRI Contrast Agents. *ACS Nano* 2015;9:12425-12435.
49. Aime S, Caravan P. Biodistribution of gadolinium-based contrast agents, including gadolinium deposition. *Journal of magnetic resonance imaging : JMRI* 2009;30:1259-1267.
50. Greenberg SA. Zinc Transmetallation and Gadolinium Retention after MR Imaging: Case Report. *Radiology* 2010;257:670-673.
51. Kanazawa Y, Miyati T, Sato O. Hemodynamic analysis of bladder tumors using T1-dynamic contrast-enhanced fast spin-echo MRI. *European Journal of Radiology* 2012;81:1682-1687.
52. Li Y, Li CH, Talham DR. One-step synthesis of gradient gadolinium ironhexacyanoferrate nanoparticles: a new particle design easily combining MRI contrast and photothermal therapy. *Nanoscale* 2015;7:5209-5216.
53. Yu C, Zhou Z, Wang J et al. In depth analysis of apoptosis induced by silica coated manganese oxide nanoparticles in vitro. *Journal of Hazardous Materials* 2015;283:519-528.
54. Jinqun Li and Zhenghuan Zhao and Jianghua Feng and Jinhao Gao and Zhong C. Understanding the metabolic fate and assessing the biosafety of MnO nanoparticles by metabonomic analysis. *Nanotechnology* 2013;24:455102.
55. Omid H, Oghabian MA, Ahmadi R et al. Synthesizing and staining manganese oxide nanoparticles for cytotoxicity and cellular uptake investigation. *Biochimica et Biophysica Acta (BBA) - General Subjects* 2014;1840:428-433.
56. Chen N, Shao C, Qu Y et al. Folic Acid-Conjugated MnO Nanoparticles as a T1 Contrast Agent for Magnetic Resonance Imaging of Tiny Brain Gliomas. *ACS Applied Materials & Interfaces* 2014;6:19850-19857.
57. Bennewitz MF, Lobo TL, Nkansah MK et al. Biocompatible and pH-Sensitive PLGA Encapsulated MnO Nanocrystals for Molecular and Cellular MRI. *ACS Nano* 2011;5:3438-3446.

58. Huang J, Xie J, Chen K et al. HSA coated MnO nanoparticles with prominent MRI contrast for tumor imaging. *Chemical Communications* 2010;46:6684-6686.
59. Blasiak B, Veggel FCJMv, Tomanek B. Applications of Nanoparticles for MRI Cancer Diagnosis and Therapy. *Journal of Nanomaterials*, 2013:1-12.
60. Tan M, Lu Z-R. Integrin Targeted MR Imaging. *Theranostics* 2011;1:83-101.
61. Rosen JE, Chan L, Shieh DB, Gu FX. Iron oxide nanoparticles for targeted cancer imaging and diagnostics. *Nanomedicine* 2012;8:275-290.
62. Tsang LLC, Chen CL, Huang TL et al. Superparamagnetic Iron Oxide-Enhanced Magnetic Resonance for Tumor Surveillance in Cirrhotic Liver Before Liver Transplantation with Explanted Liver Correlation. *Transplantation Proceedings* 2011;43:1674-1677.
63. Yang H-M, Park CW, Bae PK et al. Folate-conjugated cross-linked magnetic nanoparticles as potential magnetic resonance probes for in vivo cancer imaging. *Journal of Materials Chemistry B* 2013;1:3035-3043.
64. Khemtong C, Kessinger CW, Ren J et al. In vivo Off-Resonance Saturation Magnetic Resonance Imaging of  $\alpha\beta 3$ -Targeted Superparamagnetic Nanoparticles. *Cancer Research* 2009;69:1651-1658.
65. Carvalho A, Martins MBF, Corvo ML, Feio G. Enhanced contrast efficiency in MRI by PEGylated magnetoliposomes loaded with PEGylated SPION: Effect of SPION coating and micro-environment. *Materials Science and Engineering: C* 2014;43:521-526.
66. Lim S-W, Kim H-W, Jun H-Y et al. TCL-SPION-enhanced MRI for the Detection of Lymph Node Metastasis in Murine Experimental Model. *Academic Radiology* 2011;18:504-511.
67. Shevtsov MA, Nikolaev BP, Yakovleva LY et al. Superparamagnetic iron oxide nanoparticles conjugated with epidermal growth factor (SPION-EGF) for targeting brain tumors. *International Journal of Nanomedicine* 2014;9:273-287.
68. Sidoryk-Wegrzynowicz M, Aschner M. Role of astrocytes in manganese mediated neurotoxicity. *BMC pharmacology & toxicology*, 2013:23.
69. Borges M, Yu S, Laromaine A et al. Dual T1/T2 MRI contrast agent based on hybrid SPION@coordination polymer nanoparticles. *RSC Advances* 2015;5:86779-86783.
70. Cheng K, Yang M, Zhang R et al. Hybrid Nanotrimers for Dual T1 and T2-Weighted Magnetic Resonance Imaging. *ACS Nano* 2014;8:9884-9896.
71. Chen Y, Ai K, Liu J et al. Polydopamine-based coordination nanocomplex for T1/T2 dual mode magnetic resonance imaging-guided chemo-photothermal synergistic therapy. *Biomaterials* 2016;77:198-206.
72. Mahmoudi M, Serpooshan V, Laurent S. Engineered nanoparticles for biomolecular imaging. *Nanoscale* 2011;3:3007-3026.
73. Wahajuddin, Arora S. Superparamagnetic iron oxide nanoparticles: magnetic nanoplatforms as drug carriers. *International Journal of Nanomedicine* 2012;7:3445-3471.
74. Gupta AK, Gupta M. Synthesis and surface engineering of iron oxide nanoparticles for biomedical applications. *Biomaterials* 2005;26:3995-4021.
75. Lu A-H, Salabas EL, Schüth F. Magnetic Nanoparticles: Synthesis, Protection, Functionalization, and Application. *Angewandte Chemie International Edition* 2007;46:1222-1244.
76. Sun S, Zeng H. Size-controlled synthesis of magnetite nanoparticles. *Journal of the American Chemical Society* 2002;124:8204-8205.
77. Vayssières L, Chanéac C, Tronc E, Jolivet JP. Size Tailoring of Magnetite Particles Formed by Aqueous Precipitation: An Example of Thermodynamic Stability of Nanometric Oxide Particles. *Journal of Colloid and Interface Science* 1998;205:205-212.

78. Jana NR, Chen Y, Peng X. Size- and Shape-Controlled Magnetic (Cr, Mn, Fe, Co, Ni) Oxide Nanocrystals via a Simple and General Approach. *Chemistry of Materials* 2004;16:3931-3935.
79. Li Z, Wei L, Gao MY, Lei H. One-Pot Reaction to Synthesize Biocompatible Magnetite Nanoparticles. *Advanced Materials* 2005;17:1001-1005.
80. Laurent S, Forge D, Port M et al. Magnetic iron oxide nanoparticles: synthesis, stabilization, vectorization, physicochemical characterizations, and biological applications. *Chemical reviews* 2008;108:2064-2110.
81. Langevin D. Micelles and Microemulsions. *Annual Review of Physical Chemistry* 1992;43:341-369.
82. Tassa C, Shaw SY, Weissleder R. Dextran-Coated Iron Oxide Nanoparticles: A Versatile Platform for Targeted Molecular Imaging, Molecular Diagnostics, and Therapy. *Accounts of Chemical Research* 2011;44:842-852.
83. Berry CC, Wells S, Charles S, Curtis ASG. Dextran and albumin derivatised iron oxide nanoparticles: influence on fibroblasts in vitro. *Biomaterials* 2003;24:4551-4557.
84. Sardan M, Yildirim A, Mumcuoglu D, Tekinay AB, Guler MO. Noncovalent functionalization of mesoporous silica nanoparticles with amphiphilic peptides. *Journal of Materials Chemistry B* 2014;2:2168-2174.
85. Sulek S, Mammadov B, Mahcicek DI et al. Peptide functionalized superparamagnetic iron oxide nanoparticles as MRI contrast agents. *Journal of Materials Chemistry* 2011;21:15157-15162.
86. Trent A, Marullo R, Lin B, Black M, Tirrell M. Structural properties of soluble peptide amphiphile micelles. *Soft Matter* 2011;7:9572-9582.
87. Mlinar LB, Chung EJ, Wonder EA, Tirrell M. Active targeting of early and mid-stage atherosclerotic plaques using self-assembled peptide amphiphile micelles. *Biomaterials* 2014;35:8678-8686.
88. Chung EJ, Cheng Y, Morshed R et al. Fibrin-binding, peptide amphiphile micelles for targeting glioblastoma. *Biomaterials* 2014;35:1249-1256.
89. Peer D, Karp JM, Hong S et al. Nanocarriers as an emerging platform for cancer therapy. *Nat Nano* 2007;2:751-760.
90. Xie J, Chen K, Lee H-Y et al. Ultrasmall c (RGDyK)-coated Fe<sub>3</sub>O<sub>4</sub> nanoparticles and their specific targeting to integrin  $\alpha\beta$ 3-rich tumor cells. *Journal of the American Chemical Society* 2008;130:7542-7543.
91. Radermacher KA, Boutry S, Laurent S et al. Iron oxide particles covered with hexapeptides targeted at phosphatidylserine as MR biomarkers of tumor cell death. *Contrast Media & Molecular Imaging* 2010;5:258-267.
92. Sykes EA, Chen J, Zheng G, Chan WCW. Investigating the Impact of Nanoparticle Size on Active and Passive Tumor Targeting Efficiency. *ACS Nano* 2014;8:5696-5706.
93. Bazak R, Hourri M, Achy SE, Hussein W, Refaat T. Passive targeting of nanoparticles to cancer: A comprehensive review of the literature. *Molecular and Clinical Oncology* 2014;2:904-908.
94. Ndong C, Tate JA, Kett WC et al. Tumor Cell Targeting by Iron Oxide Nanoparticles Is Dominated by Different Factors In Vitro versus In Vivo. *PLoS ONE* 2015;10:e0115636.
95. Rosca EV, Koskimaki JE, Rivera CG et al. Anti-angiogenic peptides for cancer therapeutics. *Curr Pharm Biotechnol* 2011;12:1101-1116.
96. Ferner RE. Martindale's Extra Pharmacopoeia. *BMJ* 1996;313:1214.

97. Mohammad A, Farheen Shamsi and Amir A. Ruthenium Complexes: An Emerging Ground to the Development of Metallopharmaceuticals for Cancer Therapy. *Mini-Reviews in Medicinal Chemistry* 2015;15:1-15.
98. Greish K. Enhanced Permeability and Retention (EPR) Effect for Anticancer Nanomedicine Drug Targeting. In: Grobmyer SR, Moudgil BM, editors. *Cancer Nanotechnology*. Humana Press, 2010:25-37.
99. Calandrini V, Rossetti G, Arnesano F, Natile G, Carloni P. Computational metallomics of the anticancer drug cisplatin. *Journal of Inorganic Biochemistry* 2015;153:231-238.
100. Gopal YNV, Jayaraju D, Kondapi AK. Inhibition of Topoisomerase II Catalytic Activity by Two Ruthenium Compounds: A Ligand-Dependent Mode of Action. *Biochemistry* 1999;38:4382-4388.
101. Valiahdi SM, Heffeter P, Jakupec MA et al. The gallium complex KP46 exerts strong activity against primary explanted melanoma cells and induces apoptosis in melanoma cell lines. *Melanoma research* 2009;19:283-293.
102. Heffeter P, Jakupec MA, Körner W et al. Multidrug-resistant cancer cells are preferential targets of the new antineoplastic lanthanum compound KP772 (FFC24). *Biochemical Pharmacology* 2007;73:1873-1886.
103. Chen J, Luo Z, Zhao Z et al. Cellular localization of iron(II) polypyridyl complexes determines their anticancer action mechanisms. *Biomaterials* 2015;71:168-177.
104. Annaraj B, Neelakantan MA. Synthesis, crystal structure, spectral characterization and biological exploration of water soluble Cu(II) complexes of vitamin B6 derivative. *European Journal of Medicinal Chemistry* 2015;102:1-8.
105. Munteanu CR, Suntharalingam K. Advances in cobalt complexes as anticancer agents. *Dalton Transactions* 2015;44:13796-13808.
106. Habala L, Bartel C, Giester G et al. Complexes of N-hydroxyethyl-N-benzimidazolymethylethylenediaminediacetic acid with group 12 metals and vanadium—Synthesis, structure and bioactivity of the vanadium complex. *Journal of Inorganic Biochemistry* 2015;147:147-152.
107. Eshkourfu R, Čobeljić B, Vujčić M et al. Synthesis, characterization, cytotoxic activity and DNA binding properties of the novel dinuclear cobalt(III) complex with the condensation product of 2-acetylpyridine and malonic acid dihydrazide. *Journal of Inorganic Biochemistry* 2011;105:1196-1203.
108. Mi P, Dewi N, Yanagie H et al. Hybrid Calcium Phosphate-Polymeric Micelles Incorporating Gadolinium Chelates for Imaging-Guided Gadolinium Neutron Capture Tumor Therapy. *ACS Nano* 2015;9:5913-5921.
109. He L, Chen T, You Y et al. A cancer-targeted nanosystem for delivery of gold(III) complexes: enhanced selectivity and apoptosis-inducing efficacy of a gold(III) porphyrin complex. *Angew Chem Int Ed Engl* 2014;53:12532-12536.
110. Palchoudhuri R, Hergenrother PJ. DNA as a target for anticancer compounds: methods to determine the mode of binding and the mechanism of action. *Current Opinion in Biotechnology* 2007;18:497-503.
111. Boer DR, Canals A, Coll M. DNA-binding drugs caught in action: the latest 3D pictures of drug-DNA complexes. *Dalton Transactions* 2009:399-414.
112. Eshkourfu R, Čobeljić B, Vujčić M et al. Synthesis, characterization, cytotoxic activity and DNA binding properties of the novel dinuclear cobalt(III) complex with the condensation product of 2-acetylpyridine and malonic acid dihydrazide. *J Inorg Biochem* 2011;105:1196-1203.

113. Buurma NJ, Haq I. Advances in the analysis of isothermal titration calorimetry data for ligand–DNA interactions. *Methods* 2007;42:162-172.
114. Sava G, Jaouen G, Hillard EA, Bergamo A. Targeted therapy vs. DNA-adduct formation-guided design: thoughts about the future of metal-based anticancer drugs. *Dalton Transactions* 2012;41:8226-8234.
115. Sułkowska A, Równicka J, Bojko B, Sułkowski W. Interaction of anticancer drugs with human and bovine serum albumin. *Journal of Molecular Structure* 2003;651–653:133-140.
116. Carlo Bertucci and Enrico D. Reversible and Covalent Binding of Drugs to Human Serum Albumin: Methodological Approaches and Physiological Relevance. *Current Medicinal Chemistry* 2002;9:1463-1481.
117. Yi G, Yao Z, Feng Yang and Hong L. Evaluation of Interactions Between Platinum-/Ruthenium-Based Anticancer Agents and Human Serum Albumin: Development of HSA Carrier for Metal-Based Drugs. *Current Pharmaceutical Design* 2015;21:1848-1861.
118. He XM, Carter DC. Atomic structure and chemistry of human serum albumin. *Nature* 1992;358:209-215.
119. Fanali G, di Masi A, Trezza V et al. Human serum albumin: from bench to bedside. *Mol Aspects Med* 2012;33:209-290.
120. Roche M, Rondeau P, Singh NR, Tarnus E, Bourdon E. The antioxidant properties of serum albumin. *FEBS Lett* 2008;582:1783-1787.
121. Gou Y, Zhang Y, Qi J et al. Enhancing the copper(II) complexes cytotoxicity to cancer cells through bound to human serum albumin. *Journal of Inorganic Biochemistry* 2015;144:47-55.
122. Gabai-Kapara E, Lahad A, Kaufman B et al. Population-based screening for breast and ovarian cancer risk due to BRCA1 and BRCA2. *Proceedings of the National Academy of Sciences* 2014;111:14205-14210.
123. Day FR, Ruth KS, Thompson DJ et al. Large-scale genomic analyses link reproductive aging to hypothalamic signaling, breast cancer susceptibility and BRCA1-mediated DNA repair. *Nat Genet* 2015;47:1294-1303.
124. Accardo A, Tesaro D, Morelli G. Peptide-based targeting strategies for simultaneous imaging and therapy with nanovectors. *Polym J* 2013;45:481-493.
125. Folkman J, Merler E, Abernathy C, Williams G. ISOLATION OF A TUMOR FACTOR RESPONSIBLE FOR ANGIOGENESIS. *The Journal of Experimental Medicine* 1971;133:275-288.
126. Nishida N, Yano H, Nishida T, Kamura T, Kojiro M. Angiogenesis in Cancer. *Vascular Health and Risk Management* 2006;2:213-219.
127. Miao H-Q, Lee P, Lin H, Soker S, Klagsbrun M. Neuropilin-1 expression by tumor cells promotes tumor angiogenesis and progression. *The FASEB Journal* 2000;14:2532-2539.
128. Xu Y, Li P, Zhang X et al. Prognostic implication of neuropilin-1 upregulation in human nasopharyngeal carcinoma. *Diagnostic Pathology* 2013;8:155-155.
129. Zhuang P-Y, Wang J-D, Tang Z-H et al. Peritumoral Neuropilin-1 and VEGF receptor-2 expression increases time to recurrence in hepatocellular carcinoma patients undergoing curative hepatectomy. *Oncotarget* 2014;5:11121-11132.
130. Starzec A, Ladam P, Vassy R et al. Structure-function analysis of the antiangiogenic ATWLPPR peptide inhibiting VEGF(165) binding to neuropilin-1 and molecular dynamics simulations of the ATWLPPR/neuropilin-1 complex. *Peptides* 2007;28:2397-2402.
131. Benachour H, Sève A, Bastogne T et al. Multifunctional Peptide-Conjugated Hybrid Silica Nanoparticles for Photodynamic Therapy and MRI. *Theranostics* 2012;2:889-904.

132. Mulder W, Strijkers GJ, Van Tilborg G, Griffioen AW, Nicolay K. Lipid-based nanoparticles for contrast-enhanced MRI and molecular imaging. *NMR in Biomedicine* 2006;19:142-164.
133. Peng XH, Qian X, Mao H et al. Targeted magnetic iron oxide nanoparticles for tumor imaging and therapy. *Int J Nanomedicine* 2008;3:311-321.
134. Akerman ME, Chan WC, Laakkonen P, Bhatia SN, Ruoslahti E. Nanocrystal targeting in vivo. *Proc Natl Acad Sci U S A* 2002;99:12617-12621.
135. Ling D, Hyeon T. Chemical design of biocompatible iron oxide nanoparticles for medical applications. *Small* 2013;9:1450-1466.
136. Zhou Z, Qutaish M, Han Z et al. MRI detection of breast cancer micrometastases with a fibronectin-targeting contrast agent. *Nat Commun* 2015;6.
137. Lee N, Choi Y, Lee Y et al. Water-Dispersible Ferrimagnetic Iron Oxide Nanocubes with Extremely High  $r_2$  Relaxivity for Highly Sensitive in Vivo MRI of Tumors. *Nano Letters* 2012;12:3127-3131.
138. Lee SJ, Lee HJ, Moon MJ et al. Superparamagnetic iron oxide nanoparticles-loaded polymersome-mediated gene delivery guided by enhanced magnetic resonance signal. *J Nanosci Nanotechnol* 2011;11:7057-7060.
139. Sun S, Zeng H, Robinson DB et al. Monodisperse MFe<sub>2</sub>O<sub>4</sub> (M= Fe, Co, Mn) nanoparticles. *Journal of the American Chemical Society* 2004;126:273-279.
140. Muthiah M, Park I-K, Cho C-S. Surface modification of iron oxide nanoparticles by biocompatible polymers for tissue imaging and targeting. *Biotechnology advances* 2013;31:1224-1236.
141. Boyer C, Whittaker MR, Bulmus V, Liu J, Davis TP. The design and utility of polymer-stabilized iron-oxide nanoparticles for nanomedicine applications. *NPG Asia Materials* 2010;2:23-30.
142. Wu X, Tan Y, Mao H, Zhang M. Toxic effects of iron oxide nanoparticles on human umbilical vein endothelial cells. *Int J Nanomedicine* 2010;5:385-399.
143. Gaspar D, Veiga AS, Sinthuvanich C, Schneider JP, Castanho MARB. Anticancer Peptide SVS-1: Efficacy Precedes Membrane Neutralization. *Biochemistry* 2012;51:6263-6265.
144. Bachelder RE, Crago A, Chung J et al. Vascular Endothelial Growth Factor Is an Autocrine Survival Factor for Neuropilin-expressing Breast Carcinoma Cells. *Cancer Research* 2001;61:5736-5740.
145. Diehl KH, Hull R, Morton D et al. A good practice guide to the administration of substances and removal of blood, including routes and volumes. *J Appl Toxicol* 2001;21:15-23.
146. Yang C, Uertz J, Yohan D, Chithrani BD. Peptide modified gold nanoparticles for improved cellular uptake, nuclear transport, and intracellular retention. *Nanoscale* 2014;6:12026-12033.
147. Periyasamy K, Baskaran K, Ilakkia A et al. Antitumor efficacy of tangeretin by targeting the oxidative stress mediated on 7,12-dimethylbenz(a) anthracene-induced proliferative breast cancer in Sprague-Dawley rats. *Cancer Chemother Pharmacol* 2015;75:263-272.
148. Just N. Improving tumour heterogeneity MRI assessment with histograms. *Br J Cancer* 2014;111:2205-2213.
149. Zhang X-D, Wu H-Y, Wu D et al. Toxicologic effects of gold nanoparticles in vivo by different administration routes. *International Journal of Nanomedicine* 2010;5:771-781.

150. Myer K. *Standard Handbook of Biomedical Engineering & Design*. McGRAW-HILL, New York, Chicago, San Francisco, Lisbon, London, Madrid, Mexico City, Milan, New Delhi, San Juan, Seoul, Singapore, Sydney, Toronto, 2003.
151. Yu MK, Jeong YY, Park J et al. Drug-loaded superparamagnetic iron oxide nanoparticles for combined cancer imaging and therapy in vivo. *Angew Chem Int Ed Engl* 2008;47:5362-5365.
152. Pombo García K, Zarschler K, Barbaro L et al. Zwitterionic-coated "stealth" nanoparticles for biomedical applications: recent advances in countering biomolecular corona formation and uptake by the mononuclear phagocyte system. *Small* 2014;10:2516-2529.
153. Nardone G, Compare D, Liguori E et al. Protective effects of *Lactobacillus paracasei* F19 in a rat model of oxidative and metabolic hepatic injury. *Am J Physiol Gastrointest Liver Physiol* 2010;299:G669-676.
154. Meerasa A, G. Huang J, X. Gu F. CH50: A Revisited Hemolytic Complement Consumption Assay for Evaluation of Nanoparticles and Blood Plasma Protein Interaction. *Current Drug Delivery* 2011;8:290-298.
155. Mirabello V, Calatayud DG, Arrowsmith RL, Ge H, Pascu SI. Metallic nanoparticles as synthetic building blocks for cancer diagnostics: from materials design to molecular imaging applications. *Journal of Materials Chemistry B* 2015;3:5657-5672.
156. Scopes R. Measurement of protein by spectrophotometry at 205 nm. *Analytical biochemistry* 1974;59:277-282.
157. Obenauf AC, Zou Y, Ji AL et al. Therapy-induced tumour secretomes promote resistance and tumour progression. *Nature* 2015;520:368-372.
158. Stewart MK, Bechberger JF, Welch I, Naus CC, Laird DW. Cx26 knockout predisposes the mammary gland to primary mammary tumors in a DMBA-induced mouse model of breast cancer. *Oncotarget* 2015.
159. Sarioglu OF, Tekiner-Gursacli R, Ozdemir A, Tekinay T. Comparison of Au(III) and Ga(III) ions' binding to calf thymus DNA: spectroscopic characterization and thermal analysis. *Biol Trace Elem Res* 2014;160:445-452.
160. Sarioglu OF, Ozdemir A, Karaboduk K, Tekinay T. Comparative serum albumin interactions and antitumor effects of Au(III) and Ga(III) ions. *J Trace Elem Med Biol* 2015;29:111-115.
161. Gómez-Ruiz S, Gallego B, Kaluđerović MR et al. Novel gallium(III) complexes containing phthaloyl derivatives of neutral aminoacids with apoptotic activity in cancer cells. *Journal of Organometallic Chemistry* 2009;694:2191-2197.
162. Samari F, Hemmateenejad B, Shamsipur M, Rashidi M, Samouei H. Affinity of two novel five-coordinated anticancer Pt(II) complexes to human and bovine serum albumins: a spectroscopic approach. *Inorg Chem* 2012;51:3454-3464.
163. Kaluđerović MR, Gómez-Ruiz S, Gallego B et al. Anticancer activity of dinuclear gallium(III) carboxylate complexes. *European Journal of Medicinal Chemistry* 2010;45:519-525.
164. Tabassum S, Asim A, Arjmand F, Afzal M, Bagchi V. Synthesis and characterization of copper(II) and zinc(II)-based potential chemotherapeutic compounds: Their biological evaluation viz. DNA binding profile, cleavage and antimicrobial activity. *European Journal of Medicinal Chemistry* 2012;58:308-316.
165. Wilfinger N, Austin S, Scheiber-Mojdekhar B et al. Novel p53-dependent anticancer strategy by targeting iron signaling and BNIP3L-induced mitophagy. *Oncotarget* 2015.

166. Ortega R, Suda A, Devès G. Nuclear microprobe imaging of gallium nitrate in cancer cells. *Nuclear Instruments and Methods in Physics Research Section B: Beam Interactions with Materials and Atoms* 2003;210:364-367.
167. Enyedy ÉA, Dömötör O, Varga E et al. Comparative solution equilibrium studies of anticancer gallium(III) complexes of 8-hydroxyquinoline and hydroxy(thio)pyrone ligands. *Journal of Inorganic Biochemistry* 2012;117:189-197.
168. Lessa JA, Parrilha GL, Beraldo H. Gallium complexes as new promising metallodrug candidates. *Inorganica Chimica Acta* 2012;393:53-63.
169. Chitambar CR. Gallium-containing anticancer compounds. *Future Medicinal Chemistry* 2012;4:1257-1272.
170. Despaigne AA, Parrilha GL, Izidoro JB et al. 2-Acetylpyridine- and 2-benzoylpyridine-derived hydrazones and their gallium(III) complexes are highly cytotoxic to glioma cells. *Eur J Med Chem* 2012;50:163-172.
171. Silva F, Marques F, Santos IC et al. Synthesis, characterization and cytotoxic activity of gallium(III) complexes anchored by tridentate pyrazole-based ligands. *J Inorg Biochem* 2010;104:523-532.
172. Chen D, Frezza M, Shakya R et al. Inhibition of the proteasome activity by gallium(III) complexes contributes to their anti prostate tumor effects. *Cancer Res* 2007;67:9258-9265.
173. Li W, Xie Y, Sun RWY et al. Inhibition of Akt sensitises neuroblastoma cells to gold(III) porphyrin 1a, a novel antitumour drug induced apoptosis and growth inhibition. *Br J Cancer* 2009;101:342-349.
174. Lum CT, Yang ZF, Li HY et al. Gold(III) compound is a novel chemocytotoxic agent for hepatocellular carcinoma. *International Journal of Cancer* 2006;118:1527-1538.
175. Tu S, Wai-Yin Sun R, Lin MCM et al. Gold (III) porphyrin complexes induce apoptosis and cell cycle arrest and inhibit tumor growth in colon cancer. *Cancer* 2009;115:4459-4469.
176. To YF, Sun RW-Y, Chen Y et al. Gold(III) porphyrin complex is more potent than cisplatin in inhibiting growth of nasopharyngeal carcinoma in vitro and in vivo. *International Journal of Cancer* 2009;124:1971-1979.
177. Lessa JA, Ferraz KS, Guerra JC et al. Spectroscopic and electrochemical characterization of gold(I) and gold(III) complexes with glyoxaldehyde bis(thiosemicarbazones): cytotoxicity against human tumor cell lines and inhibition of thioredoxin reductase activity. *Biometals* 2012;25:587-598.
178. Zou T, Lum CT, Lok C-N, Zhang J-J, Che C-M. Chemical biology of anticancer gold(III) and gold(I) complexes. *Chemical Society Reviews* 2015;44:8786-8801.
179. Kim NH, Park HJ, Oh MK, Kim IS. Antiproliferative effect of gold(I) compound auranofin through inhibition of STAT3 and telomerase activity in MDA-MB 231 human breast cancer cells. *BMB Rep* 2013;46:59-64.
180. Gimeno MC, Goitia H, Laguna A et al. Conjugates of ferrocene with biological compounds. Coordination to gold complexes and antitumoral properties. *J Inorg Biochem* 2011;105:1373-1382.
181. Arjmand F, Parveen S, Afzal M, Shahid M. Synthesis, characterization, biological studies (DNA binding, cleavage, antibacterial and topoisomerase I) and molecular docking of copper(II) benzimidazole complexes. *Journal of Photochemistry and Photobiology B: Biology* 2012;114:15-26.
182. Wu SS, Yuan WB, Wang HY et al. Synthesis, crystal structure and interaction with DNA and HSA of (N,N'-dibenzylethane-1,2-diamine) transition metal complexes. *J Inorg Biochem* 2008;102:2026-2034.

183. Liu H-K, Sadler PJ. Interactions of Metallo drugs with DNA. *NMR of Biomolecules*. Wiley-VCH Verlag GmbH & Co. KGaA, 2012:282-296.
184. Zhou X, Lü W, Su L et al. The binding affinity of amino acid-protein: hydroxyproline binding site I on human serum albumin. *Org Biomol Chem* 2012;10:8314-8321.
185. Kratz F. Albumin as a drug carrier: Design of prodrugs, drug conjugates and nanoparticles. *Journal of Controlled Release* 2008;132:171-183.
186. Bourassa P, Dubeau S, Maharvi GM et al. Binding of antitumor tamoxifen and its metabolites 4-hydroxytamoxifen and endoxifen to human serum albumin. *Biochimie* 2011;93:1089-1101.
187. Ju CC, Zhang AG, Yuan CL, Zhao XL, Wang KZ. The interesting DNA-binding properties of three novel dinuclear Ru(II) complexes with varied lengths of flexible bridges. *J Inorg Biochem* 2011;105:435-443.
188. Kypr J, Kejnovská I, Renčíuk D, Vorlíčková M. Circular dichroism and conformational polymorphism of DNA. *Nucleic Acids Research* 2009;37:1713-1725.
189. Ivanov VI, Minchenkova LE, Schyolkina AK, Poletayev AI. Different conformations of double-stranded nucleic acid in solution as revealed by circular dichroism

Biopolymers Volume 12, Issue 1. *Biopolymers*, 1973:89-110.

190. Sun J, Lu Y, Wang L et al. Fluorescence turn-on detection of DNA based on the aggregation-induced emission of conjugated poly(pyridinium salt)s. *Polymer Chemistry* 2013;4:4045-4051.
191. Jangir DK, Charak S, Mehrotra R, Kundu S. FTIR and circular dichroism spectroscopic study of interaction of 5-fluorouracil with DNA. *J Photochem Photobiol B* 2011;105:143-148.
192. Uma V, Elango M, Nair BU. Copper(II) Terpyridine Complexes

Effect of Substituent on DNA Binding and Nuclease Activity, *European Journal of Inorganic Chemistry* Volume 2007, Issue 22. *European Journal of Inorganic Chemistry*, 2007:3484-3490.

193. Freyer MW, Lewis EA. Isothermal Titration Calorimetry: Experimental Design, Data Analysis, and Probing Macromolecule/Ligand Binding and Kinetic Interactions. *Methods in Cell Biology*. Academic Press, 2008:79-113.
194. Sikora CW, Turner RJ. Investigation of ligand binding to the multidrug resistance protein EmrE by isothermal titration calorimetry. *Biophys J* 2005;88:475-482.
195. Brain S. *Fundamentals of Fourier Transform Infrared Spectroscopy*. CRC Press, Washington, D.C., 1996.
196. Kong J, Yu S. Fourier Transform Infrared Spectroscopic Analysis of Protein Secondary Structures. *Acta Biochimica et Biophysica Sinica* 2007;39:549-559.
197. Tyagi G, Charak S, Mehrotra R. Binding of an indole alkaloid, vinblastine to double stranded DNA: A spectroscopic insight in to nature and strength of interaction. *Journal of Photochemistry and Photobiology B: Biology* 2012;108:48-52.
198. Nafisi S, Sobhanmanesh A, Esm-Hosseini M, Alimoghaddam K, Tajmir-Riahi HA. Interaction of antitumor drug Sn(CH<sub>3</sub>)<sub>2</sub>Cl<sub>2</sub> with DNA and RNA. *Journal of Molecular Structure* 2005;750:22-27.
199. Ozdemir A, Gursaclı RT, Tekinay T. Non-intercalative, Deoxyribose Binding of Boric Acid to Calf Thymus DNA. *Biol Trace Elem Res* 2014;158:268-274.
200. Anastassopoulou J. Metal DNA interactions. *J. Mol. Struct.* , 2003:651-653.
201. Yue Y, Dong Q, Zhang Y et al. Synthesis of imidazole derivatives and the spectral characterization of the binding properties towards human serum albumin. *Spectrochimica Acta Part A: Molecular and Biomolecular Spectroscopy* 2016;153:688-703.

202. He W, Li Y, Xue C et al. Effect of Chinese medicine alpinetin on the structure of human serum albumin. *Bioorganic & Medicinal Chemistry* 2005;13:1837-1845.
203. Liu J, Yue Y, Liu M, Zhang N, Zhuo K. Synthesis and interaction studies of benzimidazole derivative with human serum albumin. *Spectrochimica Acta Part A: Molecular and Biomolecular Spectroscopy* 2011;82:299-305.
204. Jovanović VB, Penezić-Romanjuk AZ, Pavićević ID, Aćimović JM, Mandić LM. Improving the reliability of human serum albumin-thiol group determination. *Analytical Biochemistry* 2013;439:17-22.
205. Montero MT, Hernández J, Estelrich J. Fluorescence quenching of albumin. A spectrofluorimetric experiment. *Biochemical Education* 1990;18:99-101.
206. Sułkowska A. Interaction of drugs with bovine and human serum albumin. *Journal of Molecular Structure* 2002;614:227-232.
207. N'soukpoé-Kossi CN, Sedaghat-Herati R, Ragi C, Hotchandani S, Tajmir-Riahi HA. Retinol and retinoic acid bind human serum albumin: stability and structural features. *Int J Biol Macromol* 2007;40:484-490.
208. Vivian JT, Callis PR. Mechanisms of Tryptophan Fluorescence Shifts in Proteins. *Biophysical Journal* 2001;80:2093-2109.
209. Leavitt S, Freire E. Direct measurement of protein binding energetics by isothermal titration calorimetry. *Current Opinion in Structural Biology* 2001;11:560-566.
210. Li Y, Jia B, Wang H et al. The interaction of 2-mercaptobenzimidazole with human serum albumin as determined by spectroscopy, atomic force microscopy and molecular modeling. *Colloids Surf B Biointerfaces* 2013;104:311-317.
211. He L, Chen T, You Y et al. A Cancer-Targeted Nanosystem for Delivery of Gold(III) Complexes: Enhanced Selectivity and Apoptosis-Inducing Efficacy of a Gold(III) Porphyrin Complex. *Angewandte Chemie International Edition* 2014;53:12532-12536.
212. Sadler PJ, Sue RE. The Chemistry of Gold Drugs. *Metal-Based Drugs* 1994;1:107-144.
213. Straus DJ. Gallium nitrate in the treatment of lymphoma. *Semin Oncol* 2003;30:25-33.
214. Chitambar CR. Gallium nitrate for the treatment of non-Hodgkin's lymphoma. *Expert Opin Investig Drugs* 2004;13:531-541.
215. Sheng R, Luo T, Zhu Y et al. The intracellular plasmid DNA localization of cationic reducible cholesterol-disulfide lipids. *Biomaterials* 2011;32:3507-3519.
216. Chatterjee T, Pal A, Dey S, Chatterjee BK, Chakrabarti P. Interaction of virstatin with human serum albumin: spectroscopic analysis and molecular modeling. *PLoS One* 2012;7:e37468.
217. Ozdemir A, Sarioglu O, Tekinay T. Spectroscopic Evaluation of DNA-Borate Interactions. *Biological Trace Element Research* 2015;168:508-515.
218. Loomis WD, Durst RW. Chemistry and biology of boron. *Biofactors* 1992;3:229-239.
219. Pandey N, Gupta B. The impact of foliar boron sprays on reproductive biology and seed quality of black gram. *J Trace Elem Med Biol* 2013;27:58-64.
220. Boron. *J Diet Suppl* 2008;5:62-94.
221. Ban HS, Nakamura H. Boron-Based Drug Design. *The Chemical Record* 2015;15:616-635.
222. Del-Campo Marín CM, Oron G. Boron removal by the duckweed *Lemna gibba*: a potential method for the remediation of boron-polluted waters. *Water Res* 2007;41:4579-4584.
223. Davis SM, Drake KD, Maier KJ. Toxicity of boron to the duckweed, *Spirodella polyrrhiza*. *Chemosphere* 2002;48:615-620.

224. Wang J, Wu W, Jiang X. Nanoscaled boron-containing delivery systems and therapeutic agents for cancer treatment. *Nanomedicine* 2015;10:1149-1163.
225. Sukhorukova IV, Zhitnyak IY, Kovalskii AM et al. Boron Nitride Nanoparticles with a Petal-Like Surface as Anticancer Drug-Delivery Systems. *ACS Applied Materials & Interfaces* 2015;7:17217-17225.
226. Romulus ISaRP. Boron-Containing Compounds as Preventive and Chemotherapeutic Agents for Cancer. *Anti-Cancer Agents in Medicinal Chemistry* 2010;10:346-351.
227. Grimes RN. Boron Clusters Come of Age. *J. of Chem. Education*, 2004:657-672.
228. Tabassum S, Chandra Sharma G, Arjmand F, Azam A. DNA interaction studies of new nano metal based anticancer agent: validation by spectroscopic methods. *Nanotechnology* 2010;21:195102.
229. Yang CH, Lin YT, Hung YH et al. Autoradiographic and histopathological studies of boric acid-mediated BNCT in hepatic VX2 tumor-bearing rabbits: Specific boron retention and damage in tumor and tumor vessels. *Applied Radiation and Isotopes* 2015;106:176-180.
230. Kabalka GW. Recent developments in boron neutron capture therapy. *Expert Opin. Ther. Pat*, 1998:445-551.
231. Barth RF, Coderre JA, Vicente MG, Blue TE. Boron neutron capture therapy of cancer: current status and future prospects. *Clin Cancer Res* 2005;11:3987-4002.
232. Lu DR, Mehta SC, Chen W. Selective boron drug delivery to brain tumors for boron neutron capture therapy. *Adv Drug Deliv Rev* 1997;26:231-247.
233. Low LY, Hernandez H, Robinson CV et al. Metal-dependent folding and stability of nuclear hormone receptor DNA-binding domains. *J. Mol. Biol.*, 2002.
234. Shelly K, Feaks DA, Hawthorne MF et al. Model studies directed toward the boron neutron capture therapy of cancer: Boron delivery to murine tumors with liposomes. *Proc Natl Acad Sci U S A* 1992;89:9039-9043.
235. Rodríguez-Pulido A, Aicart E, Llorca O, Junquera E. Compaction process of calf thymus DNA by mixed cationic-zwitterionic liposomes: a physicochemical study. *J Phys Chem B* 2008;112:2187-2197.
236. Barranco WT, Eckhert CD. Boric acid inhibits human prostate cancer cell proliferation. 2004;216:21-29.
237. Meacham SL, Elwell KE, Ziegler S, Carper SW. Boric Acid Inhibits Cell Growth in Breast and Prostate Cancer Cell Lines. *Advances in Plant and Animal Boron Nutrition*. *Advances in Plant and Animal Boron Nutrition*, 2007:299-306.
238. Scorei R, Ciubar R, Ciofrangeanu CM et al. Comparative effects of boric acid and calcium fructoborate on breast cancer cells. *Biol Trace Elem Res* 2008;122:197-205.
239. Scorei IR. Boron Compounds in the Breast Cancer Cells Chemoprevention and Chemotherapy. In: Gunduz PE, editor. *Breast Cancer - Current and Alternative Therapeutic Modalities*. InTech, 2011.
240. Ince S, Kucukkurt I, Cigerci IH, Fatih Fidan A, Eryavuz A. The effects of dietary boric acid and borax supplementation on lipid peroxidation, antioxidant activity, and DNA damage in rats. *J Trace Elem Med Biol* 2010;24:161-164.
241. Robbins WA, Xun L, Jia J et al. Chronic boron exposure and human semen parameters. *Reprod Toxicol* 2010;29:184-190.
242. Türkez H, Geyikoğlu F, Tatar A, Keleş S, Ozkan A. Effects of some boron compounds on peripheral human blood. *Z Naturforsch C* 2007;62:889-896.
243. Turkez H. Effects of boric acid and borax on titanium dioxide genotoxicity. *J Appl Toxicol* 2008;28:658-664.

244. Turkez H, Tatar A, Hacimuftuoglu A, Ozdemir E. Boric acid as a protector against paclitaxel genotoxicity. *Acta Biochim Pol* 2010;57:95-97.
245. Weser U. Chemistry and structure of some borate polyol compounds of biochemical interest. *Structure and Bonding* 1967;2:160-180.
246. Gabel D, Foster S, Fairchild RG. The Monte Carlo simulation of the biological effect of the  $^{10}\text{B}(\text{n}, \alpha)^7\text{Li}$  reaction in cells and tissue and its implication for boron neutron capture therapy. *Radiat Res* 1987;111:14-25.
247. Geng S, Liu G, Li W, Cui F. Molecular interaction of ctDNA and HSA with sulfadiazine sodium by multispectroscopic methods and molecular modeling. *Luminescence* 2013;28:785-792.
248. Saito ST, Silva G, Pungartnik C, Brendel M. Study of DNA–emodin interaction by FTIR and UV–vis spectroscopy. *Journal of Photochemistry and Photobiology B: Biology* 2012;111:59-63.
249. Theophanides T. Fourier Transform Infrared Spectra of Calf Thymus DNA and its Reactions with the Anticancer Drug Cisplatin. 1981:461-465.
250. Yang D, Wang AH-J. Structural Studies of Interactions between anticancer platinum compounds and DNA. *Prog. Biophys. Mol. Biol.*, 1996:81-111.
251. Arjmand F, Parveen S, Afzal M, Toupet L, Ben Hadda T. Molecular drug design, synthesis and crystal structure determination of CuII–SnIV heterobimetallic core: DNA binding and cleavage studies. *Eur J Med Chem* 2012;49:141-150.
252. Chitrapriya N, Jang YJ, Kim SK, Lee H. Non-intercalative binding mode of bridged binuclear chiral Ru(II) complexes to native duplex DNA. *J Inorg Biochem* 2011;105:1569-1575.
253. Panja S, Jana B, Aich P, Basu T. In vitro interaction between calf thymus DNA and Escherichia coli LPS in the presence of divalent cation  $\text{Ca}^{2+}$ . *Biopolymers* 2008;89:606-613.
254. Kypr J, Vorlícková M. Circular dichroism spectroscopy reveals invariant conformation of guanine runs in DNA. *Biopolymers* 2002;67:275-277.
255. Zaludová R, ZÁKOVSKÁ A, Kasparková J et al. DNA interactions of bifunctional dinuclear platinum(II) antitumor agents. *Eur J Biochem* 1997;246:508-517.
256. Zhihong L, Bo G, Mancheng H, Shuni L, Shuping X. FT-IR and Raman spectroscopic analysis of hydrated cesium borates and their saturated aqueous solution. *Spectrochim Acta A Mol Biomol Spectrosc* 2003;59:2741-2745.
257. Woods WG. An introduction to boron: history, sources, uses, and chemistry. *Environmental Health Perspectives* 1994;102:5-11.
258. Jelesarov I, Bosshard HR. Isothermal titration calorimetry and differential scanning calorimetry as complementary tools to investigate the energetics of biomolecular recognition. *J Mol Recognit* 1999;12:3-18.
259. Morales KA, Lasagna M, Gribenko AV et al.  $\text{Pb}^{2+}$  as modulator of protein-membrane interactions. *J Am Chem Soc* 2011;133:10599-10611.
260. Divsalar A, Damavandi SE, Saboury AA, Seyedarabi A, Moosavi-Movahedi AA. Calorimetric and spectroscopic investigations of  $\beta$ -lactoglobulin upon interaction with copper ion. *J Dairy Res* 2012;79:209-215.
261. Liu G, Xu H, Zhang L, Zheng Y. Fe binding properties of two soybean (*Glycine max* L.) LEA4 proteins associated with antioxidant activity. *Plant Cell Physiol* 2011;52:994-1002.
262. Murai MJ, Sassonia RC, Zamboni AH et al. Characterization of the C-terminal half of human juvenile myoclonic epilepsy protein EFHC1: dimer formation blocks  $\text{Ca}^{2+}$  and  $\text{Mg}^{2+}$  binding to its functional EF-hand. *Arch Biochem Biophys* 2008;477:131-138.
263. José TJ, Conlan LH, Dupureur CM. Quantitative evaluation of metal ion binding to Pvull restriction endonuclease. *J Biol Inorg Chem* 1999;4:814-823.

264. Sacco C, Skowronsky RA, Gade S, Kenney JM, Spuches AM. Calorimetric investigation of copper(II) binding to A $\beta$  peptides: thermodynamics of coordination plasticity. *J Biol Inorg Chem* 2012;17:531-541.
265. Prislán I, Khutsishvili I, Marky LA. Interaction of minor groove ligands with G-quadruplexes: thermodynamic contributions of the number of quartets, T-U substitutions, and conformation. *Biochimie* 2011;93:1341-1350.
266. Bhattacharjee AJ, Ahluwalia K, Taylor S et al. Induction of G-quadruplex DNA structure by Zn(II) 5,10,15,20-tetrakis(N-methyl-4-pyridyl)porphyrin. *Biochimie* 2011;93:1297-1309.
267. Shukla S, Sastry M. Probing differential Ag<sup>+</sup>-nucleobase interactions with isothermal titration calorimetry (ITC): Towards patterned DNA metallization. *Nanoscale* 2009;1:122-127.
268. Wu J, Du F, Zhang P et al. Thermodynamics of the interaction of aluminum ions with DNA: implications for the biological function of aluminum. *J Inorg Biochem* 2005;99:1145-1154.
269. Markovitsi D, Gustavsson T, Banyasz A. Absorption of UV radiation by DNA: spatial and temporal features. *Mutat Res* 2010;704:21-28.
270. Sirajuddin M, Ali S, Badshah A. Drug-DNA interactions and their study by UV-Visible, fluorescence spectroscopies and cyclic voltametry. *J Photochem Photobiol B* 2013;124:1-19.
271. Ting CY, Hsu CT, Hsu HT et al. Isodiospyrin as a novel human DNA topoisomerase I inhibitor. *Biochem Pharmacol* 2003;66:1981-1991.
272. Kelly JM, Tossi AB, McConnell DJ, OhUigin C. A study of the interactions of some polypyridylruthenium (II) complexes with DNA using fluorescence spectroscopy, topoisomerisation and thermal denaturation. *Nucleic Acids Res* 1985;13:6017-6034.
273. Stohs SJ, Bagchi D. Oxidative mechanisms in the toxicity of metal ions. *Free Radic Biol Med* 1995;18:321-336.
274. Kumar RS, Arunachalam S. DNA binding and antimicrobial studies of polymer-copper(II) complexes containing 1,10-phenanthroline and L-phenylalanine ligands. *Eur J Med Chem* 2009;44:1878-1883.
275. Kunwar A, Simon E, Singh U et al. Interaction of a curcumin analogue dimethoxycurcumin with DNA. *Chem Biol Drug Des* 2011;77:281-287.
276. Mantsch HH, Chapman D. *Infrared Spectroscopy of Biomolecules*. A John Willey & Sons, Inc., 1996.
277. Adali T, Bentaleb A, Elmarzugi N, Hamza AM. PEG-calf thymus DNA interactions: conformational, morphological and spectroscopic thermal studies. *Int J Biol Macromol* 2013;61:373-378.
278. Agarwal S, Jangir DK, Singh P, Mehrotra R. Spectroscopic analysis of the interaction of lomustine with calf thymus DNA. *J Photochem Photobiol B* 2014;130:281-286.
279. Duguid JG, Bloomfield VA, Benevides JM, Thomas GJ. Raman spectroscopy of DNA-metal complexes. II. The thermal denaturation of DNA in the presence of Sr<sup>2+</sup>, Ba<sup>2+</sup>, Mg<sup>2+</sup>, Ca<sup>2+</sup>, Mn<sup>2+</sup>, Co<sup>2+</sup>, Ni<sup>2+</sup>, and Cd<sup>2+</sup>. *Biophys J* 1995;69:2623-2641.
280. LAWLEY PD. Interaction studies with DNA. III. The effect of changes in sodium ion concentration, pH and temperature on the ultra-violet absorption spectrum of sodium thymonucleate. *Biochim Biophys Acta* 1956;21:481-488.
281. Kragh-Hansen U, Vorum H. Quantitative analyses of the interaction between calcium ions and human serum albumin. *Clin Chem* 1993;39:202-208.
282. Khan AB, Khan JM, Ali MS, Khan RH, Kabir-Ud-Din. Interaction of amphiphilic drugs with human and bovine serum albumins. *Spectrochim Acta A Mol Biomol Spectrosc* 2012;97:119-124.

283. Mandeville JS, Froehlich E, Tajmir-Riahi HA. Study of curcumin and genistein interactions with human serum albumin. *J Pharm Biomed Anal* 2009;49:468-474.
284. Greenfield NJ. Using circular dichroism spectra to estimate protein secondary structure. *Nat Protoc* 2006;1:2876-2890.
285. Whitmore L, Wallace BA. Protein secondary structure analyses from circular dichroism spectroscopy: methods and reference databases. *Biopolymers* 2008;89:392-400.
286. Dong SY, Li ZQ, Shi L et al. The Interaction of Plant-growth Regulators with Serum Albumin: Molecular Modeling and Spectroscopic methods. *Food Chem Toxicol* 2014.
287. Gao H, Lei L, Liu J et al. The study on the interaction between human serum albumin and a new reagent with antitumour activity by spectrophotometric methods. *Journal of Photochemistry and Photobiology A: Chemistry* 2004;167:213-221.
288. Soriano-Ursua MA, Mancilla-Percino T, Correa-Basurto J, Querejeta E, Trujillo-Ferrara JG. Give boron a chance: boron containing compounds reach ionotropic and metabotropic transmembrane receptors. *Mini Rev Med Chem* 2011;11:1031-1038.
289. Hu Y-J, Ou-Yang Y, Dai C-M, Liu Y, Xiao X-H. Site-Selective Binding of Human Serum Albumin by Palmatine: Spectroscopic Approach. *Biomacromolecules* 2010;11:106-112.
290. Ramakrishnan S, Suresh E, Riyasdeen A, Akbarsha MA, Palaniandavar M. DNA binding, prominent DNA cleavage and efficient anticancer activities of tris(diimine)iron(II) complexes. *Dalton Trans* 2011;40:3524-3536.
291. Chen LM, Liu J, Chen JC et al. Synthesis, characterization, DNA-binding and spectral properties of complexes [Ru(L)<sub>4</sub>(dppz)]<sup>2+</sup> (L=Im and Melm). *J Inorg Biochem* 2008;102:330-341.
292. Peters T. Serum albumin. *Adv Protein Chem* 1985;37:161-245.
293. Khan MA, Muzammil S, Musarrat J. Differential binding of tetracyclines with serum albumin and induced structural alterations in drug-bound protein. *Int J Biol Macromol* 2002;30:243-249.
294. Nafisi S, Bonsaii M, Manouchehri F, Abdi K. Interaction of glycyrrhizin and glycyrrhetic acid with DNA. *DNA Cell Biol* 2012;31:114-121.
295. Zhang Y, Yue Y, Li J, Chen X. Studies on the interaction of caffeic acid with human serum albumin in membrane mimetic environments. *J Photochem Photobiol B* 2008;90:141-151.

## Appendix

### Copyright Clearance Agreements†

Reference Number	License Supplier	License Number
42	Wiley	3787641234901
89	Nature	3793020241945
109	Wiley	3793101339652
159	Springer	3747091018531
160	Elsevier	3747091213177
199	Springer	3747081364618
217	Springer	3747090854689

† All license agreements between Ayşe Özdemir and the License Suppliers are made by means of Copyright Clearance Center (CCC).